Spring 1-1-2011

Sea Level Hazards: Altimetric Monitoring of Tsunamis and Sea Level Rise

Benjamin D. Hamlington
University of Colorado at Boulder, hamlingt@colorado.edu

SEA LEVEL HAZARDS: ALTIMETRIC MONITORING OF TSUNAMIS AND SEA LEVEL RISE

by

BENJAMIN DILLON HAMLINGTON

B.S., Washington University in Saint Louis, 2007

M.S., Washington University in Saint Louis, 2007

A thesis submitted to the

Faculty of the Graduate School of the

University of Colorado in partial fulfillment

of the requirement for the degree of

Doctor of Philosophy

Department of Aerospace Engineering Sciences

2011

This thesis entitled:
Sea Level Hazards: Altimetric Monitoring of Tsunamis and Sea Level Rise
written by Benjamin D. Hamlington
has been approved for the Department of Engineering Sciences

Dr. Robert Leben

Dr. Steve Nerem

Dr. William Emery

Dr. Baylor Fox-Kemper

Dr. Oleg Godin

*Date*_____

The final copy of this thesis has been examined by the signatories, and we
Find that both the content and the form meet acceptable presentation standards
Of scholarly work in the above mentioned discipline.

Hamlington, Benjamin D., (Ph.D., Aerospace Engineering Sciences)

Sea Level Hazards: Altimetric Monitoring of Tsunamis and Sea Level Rise

Thesis directed by Dr. Robert Leben

Whether on the short timescale of an impending tsunami or the much longer timescale of climate change-driven sea level rise, the threat stemming from rising and inundating ocean waters is a great concern to coastal populations. Timely and accurate observations of potentially dangerous changes in sea level are vital in determining the precautionary steps that need to be taken in order to protect coastal communities. While instruments from the past have provided in situ measurements of sea level at specific locations across the globe, satellites can be used to provide improved spatial and temporal sampling of the ocean in addition to producing more accurate measurements. Since 1993, satellite altimetry has provided accurate measurements of sea surface height (SSH) with near-global coverage. Not only have these measurements led to the first definitive estimates of global mean sea level rise, satellite altimetry observations have also been used to detect tsunami waves in the open ocean where wave amplitudes are relatively small, a vital step in providing early warning to those potentially affected by the impending tsunami.

The use of satellite altimetry to monitor two specific sea level hazards is examined in this thesis. The first section will focus on the detection of tsunamis in the open ocean for the purpose of providing early warning to coastal inhabitants. The second section will focus on estimating secular trends using satellite altimetry data with the hope of improving our understanding of future sea level change. Results presented here will show the utility of satellite altimetry for sea level monitoring and will lay the foundation for further advancement in the detection of the two sea level hazards considered.

ACKNOWLEDGEMENTS

It is with great pleasure that I acknowledge those that have supported me throughout my work at the University of Colorado. I would like to first thank my advisor, Dr. Robert Leben, for his guidance and support. His ideas and suggestions kept my work moving forward and discussions with him were vital in improving my research. Most importantly, his ability to ask the right questions and pursue the right avenues of research has taught me valuable lessons that will benefit me greatly in my future work.

Several others have provided me with significant assistance and guidance over my four years of studies. Dr. Oleg Godin has provided me not only financial support, but has also taught me a great deal about fully exploring a gven research problem and navigating the challenges of preparing scientific work for publication. I would like to thank Dr. Kwang-Yul Kim for not only developing a tool that has proven to be so fruitful in my work, but also for helping me learn how to use and apply this technique. Lastly, I would like to thank Dr. Steve Nerem for his financial support and more importantly, introducing me to the sea level community and helping me develop my work in that area.

I owe a great deal to my family who were encouraging throughout my studies. In particular, my wife Mylinh has been a great source of support and encouragement and I appreciate her understanding during my years of being a student. To my brother, thank you for providing an excellent example for me and for being a great friend. To my parents, thank you for your support and encouragement, I couldn't ask for better parents. Finally, to my dog Milo, thank you for making sure I was awake by 6AM (at the latest) every morning so I could get an early start on my work.

TABLE OF CONTENTS **Page Number**

TABLES

Table

FIGURES

Figure

CHAPTER 1: INTRODUCTION

Millions of people across the world live in the coastal regions of continents. Some inhabit these areas to utilize the fertile lands, while others are attracted by the economic and recreational activities provided by the ocean itself. Many of these people inhabit oceanic islands with elevations less than ten meters, and one of the most serious challenges facing these coastal communities involves sea level change that can serve to permanently alter their way of life. Whether on the short timescale of an impending tsunami or the much longer timescale of climate change-driven sea level rise, the threat stemming from rising and inundating ocean waters has become a great concern in the minds of politicians, scientists and the general public alike. Scientists have expended a significant amount of time and effort in finding ways to mitigate the effects of such natural ocean hazards. Perhaps the two most important steps in countering some of the adverse effects to coastal populations are positive identification of the impending threat and then subsequent understanding of how this threat evolves over time.

Timely and accurate observations of potentially dangerous changes in sea level are vital in determining the precautionary steps that need to be taken in order to protect coastal communities. While instruments from the past have provided in situ measurements of sea level at specific locations across the globe, satellites can be used to provide improved spatial and temporal sampling of the ocean in addition to producing more accurate measurements. Since 1993, satellite altimetry has provided accurate measurements of sea surface height (SSH) with near-global coverage. Not only have these measurements led to the first definitive estimates of global mean sea level (GMSL) rise, satellite altimetry observations have also been used to detect tsunami waves in the open ocean where wave amplitudes are relatively small, a vital step in

providing early warning to those potentially affected by the impending tsunami. The modern altimetry era began with the TOPEX/Poseidon satellite altimeter launched late in 1992. With the launch of Jason-1 in 2001 and Jason-2 in 2008, a continuous sea level record of over 17 years is now available. The satellite altimeters are capable of providing near-global measurements with centimeter level accuracy, and these measurements have been used for a wide-range of applications over the past two decades.

In this thesis, I will explore the use of satellite altimetry measurements to investigate the threat posed by two different sea level hazards. The thesis will be divided into two main sections. The first will focus on the detection of tsunamis in the open ocean for the purposes of providing early warning to coastal inhabitants. The second section will focus on estimating secular trends using satellite altimetry data with the hope of improving the understanding of future sea level change. The first section is divided as follows: chapter 2 provides background information and an extensive review of the literature describing past efforts on the problem of early tsunami detection; chapter 3 describes the techniques employed to identify the tsunami in satellite altimeter measurements of the open ocean; chapter 4 provides results obtained from studying and applying the techniques in chapter 3 to several past tsunamis; finally, chapter 5 considers the merits of these techniques as the foundation of an early tsunami detection and warning system.

The second section of this thesis on the topic of estimating regional sea level trends is organized as follows: chapter 6 provides background information and a review of relevant literature on the estimation of low-frequency climate signals and secular sea level trends; chapter 7 introduces the concept of cyclostationary empirical orthogonal functions (CSEOFs); chapter 8 demonstrates how CSEOFs can be used to improve estimates of secular sea level trends over the satellite altimeter time period; chapter 9 examines the sea level reconstruction problem and how

CSEOFs can be used to create an improved reconstruction of sea level from tide gauges using satellite altimetry. Finally, in chapter 10 a final summary is given of the work presented in the thesis, and what this work means for the future of satellite monitoring of sea level hazards.

PART I: EARLY TSUNAMI DETECTION AND WARNING

CHAPTER 2: BACKGROUND

The need for a reliable system for early tsunami detection and warning was made painfully clear by the over two hundred thousand lives lost to the tsunami generated by the 9.3 magnitude Sumatra-Andaman earthquake that swept across the Indian Ocean on 26 December 2004 (Stein & Okal, 2005; Lay et al., 2005; Titov et al., 2005). The tsunami claimed the lives of over 220,000 people and despite a lag of up to several hours between the earthquake and arrival of the tsunami in some locations, the majority of victims were given little or no warning of the impending threat. While tsunamis occur frequently in the Pacific Ocean and a tsunami warning system has been in place in the region for many years, no such system was in place in the Indian Ocean and the communications infrastructure was not adequate for issuing widespread warnings at the time of the Sumatra-Andaman tsunami.

An early and dependable assessment of a tsunami threat requires detection of the tsunami wave in the open ocean away from the shore (Lautenbacher, 2005; Levin and Nosov, 2005; Bernard et al., 2006; Schindele et al., 2008). In the open ocean, however, the wave amplitude of the tsunami is small (generally much less than one meter) and it is only as it approaches the shore that the tsunami rapidly grows in amplitude. Given the expansiveness of the ocean, sensors capable of detecting the tsunami must have very broad coverage. In addition to detecting the tsunami early enough to provide adequate warning, the method of detection must be reliable with few false warnings. If coastal populations go to great lengths to move to safe areas only to find out later such an evacuation was unnecessary, they may be less likely to heed warnings in the future.

By complementing traditional seismic data and point measurements as provided by the Deep-Ocean Assessment and Reporting of Tsunamis (DART) buoys network (Gonzalez et al., 2005; Bernard et al., 2006), satellite observations of tsunami manifestations can potentially improve the accuracy and timeliness of tsunami forecasts (Levin & Nosov, 2005; Synolakis & Bernard, 2006; Geist et al., 2007; Wei et al., 2008; Behrens et al., 2008), increase the lead time of tsunami warnings, decrease the probability of false alarms (Walker, 1996; Dudley and Lee, 1998; Godin et al., 2004; Nagai et al. 2007), and help avoid unnecessary evacuations (Dudley and Lee, 1998; Bernard et al., 2006).

Satellites have detected gravity waves induced by tsunamis in the ionosphere and the potential to use global positioning system satellites (GPS) for early tsunami detection is being explored (Artru et al., 2005; Occhipinti et al., 2006). Satellite altimeters have also sampled several tsunamis over the past two decades. The satellite altimetry SSH measurements of the Sumatra-Andaman tsunami were used by a number of authors to study the properties of the tsunami, its propagation and scattering from the coastline as well as to improve the characterization of the seismic source of the tsunami, and to verify numerical models (Fine et al., 2005; Kulikov et al., 2005; Smith et al., 2005; Song et al., 2005; Titov et al., 2005; Ablain et al., 2006; Hirata et al., 2006; Kumar et al., 2006; Fujii & Satake, 2007; Gower, 2007; Hayashi, 2008; Hoechner et al., 2008; Sladen & Hebert, 2008). Detection of earlier weaker tsunamis in less extensive satellite altimetry SSH records is discussed by Okal et al. (1999) and Zaichenko et al. (2005).

Although measurements of SSH can provide definitive detection of sufficiently large tsunamis, the spatial coverage and temporal resolution of satellite altimeters are not suitable for forming the basis of a system for the early detection of tsunamis. Satellite altimeters provide

measurements only along their ground tracks and generally require ten days to obtain near global coverage. The chances are remote of actually observing a tsunami early enough to warn coastal inhabitants. Of the tsunami manifestations in the deep ocean, variations in ocean surface roughness are perhaps the most relevant and promising to detect tsunamis from space provided that these factors can be revealed by orbiting active (scatterometers) and passive (radiometers) scanning microwave sensors, which have broad coverage of hundreds of kilometers across the satellite ground track.

Tsunami-induced variations in surface roughness away from the shore were first observed in visible light originating from a tsunami approaching Oahu in 1994 (Walker, 1996; Dudley and Lee, 1998). These variations were given the name "tsunami shadows" and appear as extended darker strips on the ocean surface along a tsunami front. Formation of the tsunami shadows as areas with a different root mean square (RMS) surface slope has been explained theoretically as a result of air-sea interaction; specifically tsunami-induced perturbations in the wind velocity close to the ocean surface that are predicted to be much larger than currents in the tsunami wave (Godin, 2003, 2004; Rowan, 2004). Later theoretical studies (Godin, 2005; Troitskaya & Ermakov, 2008) corroborated these conclusions.

The Sumatra-Andaman tsunami is the first for which detailed concurrent measurements of the SSH and radar backscattering strength at nadir (σ_0) (a measure of ocean surface roughness) of the tsunami in deep water are unambiguously available. These measurements were made with microwave radar altimeters onboard the Jason-1, TOPEX/Poseidon, Envisat, and Geosat Follow-on (GFO) satellite altimeters (Smith et al., 2005; Ablain et al., 2006; Gower, 2007). In this study, the radar backscattering strength and SSH data obtained by satellite altimeters for the Sumatra-Andaman event as well as for three other tsunamis in the past two

decades are used to detect the tsunami signal in the open ocean. Using simple filtering techniques and comparison to model results, the SSH tsunami signature is detectable in satellite altimeter measurements. More importantly, through statistical analyses of multiple years of satellite altimeter observations, it can be demonstrated that tsunamis induce distinctive variations in ocean surface roughness, which can potentially be used to form the foundation of an early detection and warning system.

CHAPTER 3: DATA AND METHODS

3.1 Satellite Altimetry Data

Satellite altimetry provides concurrent measurements of SSH and σ_0. While not necessarily the focus of this study, SSH measurements allow us to identify the location of the leading edge of the tsunami. Detection of tsunamis in SSH measurements has been demonstrated in several previous studies (Okal et al., 1999; Ablain et al., 2006), although weak tsunamis generally remain obscured by background ocean variability. By utilizing satellite altimetry data, it is possible to identify the location of the tsunami's leading edge in SSH measurements and test the concurrently measured σ_0 values for tsunami-induced changes in ocean surface roughness.

While initial studies have focused on the 2004 Sumatra-Andaman tsunami, the statistical analysis described below can be applied to any tsunami event occurring within the modern altimetry era. The Radar Altimeter Database System (RADS) was used to search and collect historical altimeter records. RADS allows the user to quickly search and obtain records from several satellite altimeters (Naeije et al., 2000). With the poor spatial coverage and temporal resolution provided by satellite altimeters, the chances of an altimeter sampling a tsunami are remote. Through an extensive search of the past 17 years of satellite altimetry data, four tsunami events have been identified on which this study will focus: 1992 Nicaraguan tsunami, 1995 Chile tsunami, 2004 Sumatra-Andaman tsunami, and 2010 Chile tsunami. For the 2010 Chile tsunami, the Method of Tsunami Splitting (MOST) model SSH data produced by the NOAA Center for Tsunami Research (Titov et al., 2005; Titov and Synolakis, 1997) is used to verify the time and location of the tsunami leading edge. The two-dimensional SSH data produced by MOST were

interpolated along each altimeter ground-track of interest and compared to the satellite altimetry SSH data.

3.2 Extraction of Tsunami Signals from SSH Measurements

Two different techniques were used in an attempt to separate the tsunami signal from the background ocean variability in the SSH measurements. The first technique was used by Gower (2007) to identify the SSH signature of the 2004 Sumatra-Andaman tsunami. This method of filtering consists of subtracting a smoothed average (9-second boxcar filter) of SSH measured on the same pass of the cycles before and after the tsunami cycle. While it is possible that SSH differences between the three cycles will introduce some additional error, such filtering should remove the signals resulting from uncorrected geoid heights, mesoscale eddies, or ocean currents that persist for time periods longer than 10-day repeat cycle of Jason-1 and Jason-2. Furthermore, by using only the cycle before the tsunami cycle, we can explore the possibility of using this simple filtering technique for real-time detection of a tsunami signal in SSH measurements.

The second, more complex, filtering method is based on a specific mapping technique, first introduced by Ablain et al. (2006). The method involves collecting data provided by all available altimeters (Jason-1, Jason-2, and Envisat) in a 40-day window centered on the tsunami event. The data corresponding to the tsunami is excluded in order to not take into account measurements affected by the tsunami. An ocean anomaly mapping technique (Le Traon et al., 1998) is used to interpolate data in space and time along each altimeter ground-track on the day of the tsunami. The resulting interpolated sea level anomaly data correspond to the sea level signals that would have been observed had the tsunami not been present. This interpolated data is

subsequently removed from the actual SSH measurements to produce a time series featuring the tsunami signal more prominently and that is less affected by the background ocean variability, reflecting only periods lower than about 15 days. As with the first filtering technique, however, other errors could remain since no statistical correction can perfectly reproduce the complex dynamics of the ocean surface. This more elaborate technique has been used with great success to identify the 2004 Sumatra-Andaman tsunami signal in the satellite altimetry data. Both of the filtering methods are used in an attempt to extract and identify the tsunami signal resulting from the earthquake occurring on February 27th, 2010 off the coast of Chile. The filtered results are also compared to the MOST-derived SSH measurements and the feasibility of using such methods for real-time detection of tsunamis in the open ocean is considered. This analysis will not be discussed in-depth for the 2004 Sumatra-Andaman tsunami, as similar studies have already been performed (Ablain et al., 2006; Gower, 2007). However, the use of filtering in identifying the leading edges of the 1992 Nicaraguan and 1995 Chilean tsunamis is explored and compared to the analysis of Okal et al. (1999) on these two tsunamis.

3.3 Analysis of Sea Surface Roughness Variations

3.3.1 Theory of tsunami-induced wind velocity perturbations

Long surface gravity waves in the ocean modulate short gravity and gravity-capillary waves and change ocean surface roughness through the interaction of short waves with near-surface currents and variations of near-surface wind-induced by long waves (Hara & Plant, 1994; Troitskaya, 1994; Kudryatsev et al., 1997; Cohen and Belcher, 1999; Godin and Irisov, 2003). Modulation due to currents is negligible for a tsunami in the deep ocean (Godin, 2003, 2004).

Tsunami-induced variations in ocean surface roughness away from the shore result from variations in wind velocity that accompany tsunami waves, and have been predicted to be much larger than currents in the tsunami wave (Godin, 2003, 2004, 2005). Godin (2003, 2004, 2005) found that significant variations in the mean wind velocity arise from the generation of viscous waves in the atmosphere by coherent large-scale motion of the ocean surface in a tsunami wave. However, the magnitude of the surface roughness modulations and the position of areas with increased and decreased roughness are sensitive to the choice of a closure hypothesis for turbulence in the atmospheric boundary layer. Although any theoretical explanation of tsunami-induced surface roughness variations is still tentative, measuring these variations in the open ocean can provide insight into the physics of the interaction of fast surface waves with turbulent wind.

As outlined in Godin et al. (2009), there is no universally accepted model of airflow over fast sea waves. Using assumptions made in (Godin, 2005), in the presence of a monochromatic tsunami wave, the wind speed relative to the ocean surface retains a logarithmic profile up to a few tens of meters above the surface. The effective wind speed depends on characteristics of the tsunami and differs from the background wind speed by the factor:

$$M = 1 - \frac{\kappa a c}{H u_* \ln \beta} \tag{3.1}$$

where κ is the von Karman constant, u_* is the friction velocity, H is the height of the background logarithmic boundary layer, a is the SSH change due to the tsunami, c is the tsunami phase speed,

$$\beta = \frac{\kappa u_* T}{2\pi z_0} \tag{3.2}$$

z_0 is the roughness length, and T is the tsunami period.

For a monochromatic tsunami wave, the effective wind speed varies periodically in time with the SSH change. As long as the relaxation time of wind waves is much smaller than the tsunami period, the time dependence of the effective wind speed can be disregarded when determining characteristics of the ocean surface roughness that correspond to a given instantaneous value of the wind modulation M. Variations in the radar backscattering strength at nadir, σ_0, resulting from the tsunami-induced wind variations can be found in the Modified Chelton-Wentz algorithm (Witter & Chelton, 1991) or the Freilich-Challenor algorithm (Freilich & Challenor, 1994) by comparing the σ_0 values that correspond to the background and effective wind speeds.

3.3.2 Statistical Randomization Tests

Ocean surface roughness is influenced by diverse phenomena in the ocean and atmosphere, including wind gusts, currents, internal gravity waves, and oceanographic fronts. The resulting σ_0 variability can far exceed the expected tsunami-induced variations. To determine whether the σ_0 variations observed were indeed caused by a tsunami and whether tsunami signals can be reliably extracted from σ_0 data, data with and without the tsunami present must be compared.

Tsunamis have several distinctive spatio-temporal characteristics that aid in the retrieval of the tsunami signal from the "noise" arising from other geophysical processes. Perhaps the most distinctive attribute of tsunami-induced roughness variations is the propagation speed relative to the ocean bottom. However, satellite altimeters only provide a "snapshot" of the ocean surface, and thus the propagation speed of the tsunami cannot be used to identify tsunami-induced features in satellite altimeter data. Instead, we systematically utilize spatial filtering (Powell & Leben, 2004) to suppress σ_0 variations that are unrelated to tsunamis.

To determine if σ_0 variations were induced by the passage of a tsunami, statistical randomization tests (Edgington, 1995) were performed to compare data with and without the tsunami present. One thousand 3.2°-windows (each containing 64 points of data) were randomly selected from the area of the ocean through which the tsunami passed. For instance, for the 2004 Sumatra-Andaman tsunami, one thousand 3.2°-windows centered between 20°S and 10°N in the tropical Indian Ocean were selected. Mean σ_0 values were subtracted in each window to calculate the σ_0 anomaly. The RMS values and the number of zero crossings were calculated for the σ_0 anomaly in each window and compared to the respective values in the 3.2°-window containing the leading edge of the tsunami. The RMS σ_0 anomaly characterizes the strength of the surface roughness variations, while the number of zero crossings serves as a measure of the spatial scale of the variations. If the tsunami-induced variations were distinctive and unique, we would expect the window containing the leading edge of the tsunami to have both a higher RMS and a greater number of zero crossings than found in the 1,000 randomly selected windows.

CHAPTER 4: RESULTS

In this chapter, four different tsunamis are investigated: 2004 Sumatra-Andaman tsunami, 2010 Chile tsunami, 1992 Nicaragua tsunami and the 1995 Chile tsunami. The SSH and σ_0 data for each tsunami are both analyzed in an attempt to detect the tsunami signal in the measurements. The results for each tsunami are outlined below.

4.1 2004 Sumatra-Andaman Tsunami

Four satellite altimeters overflew the 2004 Sumatra-Andaman tsunami during its propagation across the Indian Ocean. Envisat, Geosat Follow-On (GFO), Jason-1, and TOPEX/Poseidon measured the tsunami at times ranging from two hours to seven hours after the tsunamigenic earthquake occurred. Of these four satellite altimeters, Jason-1 provides the earliest observations of the Sumatra-Andaman tsunami and has the most extensive records. Jason-1 encountered the leading edge of the tsunami on pass 129 of cycle 109 approximately 1 h 53 mins after the earthquake (Ablain et al., 2006; Gower, 2007) at about 5°S in the Indian Ocean heading northeast on ascending pass 129 of cycle 109 (Fig. 4.1). TOPEX overflew the tsunami approximately 7 minutes after the Jason-1 satellite altimeter on pass 129 of cycle 452 with the largest amplitude found between 5°S and 2°S. The Envisat satellite altimeter was the next to encounter the tsunami on descending pass 352 of cycle 33 over 3 hours after the generation of the tsunami. Finally, GFO observed the tsunami 7 h 22 mins after the earthquake on descending pass 208 of cycle 143.

4.1.1 Analysis of Sea Surface Height Measurements

The SSH measurements provided by satellite altimetry on the day of the 2004 Sumatra-Andaman tsunami have been analyzed in several different studies (Fine et al., 2005; Kulikov et al., 2005; Smith et al., 2005; Song et al., 2005; Titov et al., 2005; Ablain et al., 2006; Gower et al., 2007). Jason-1 provides the earliest observations of the

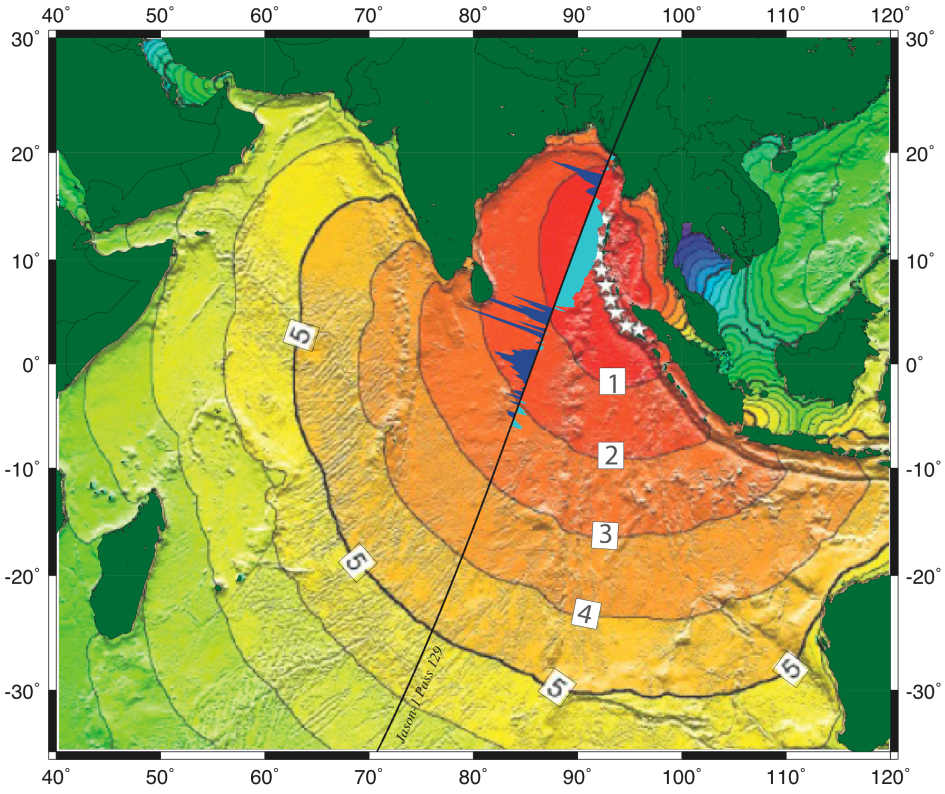

Figure 4.1. Jason-1 satellite altimeter overflight of the Sumatra-Andaman tsunami. The Jason-1 ground track and C-band σ_0 data for pass 129 of cycle 109 is superimposed on contours of the tsunami leading wave front at hourly intervals after the earthquake. White stars show the location of the tsunami wave sources. (Tsunami wave front graphic is provided courtesy of the National Geophysical Data Center/NOAA).

Sumatra-Andaman tsunami. Ablain et al. (2006) show that the leading edge of the tsunami is contained between approximately 6°S and 2°S latitudes. By using the simple filtering technique of Gower (2007), it is seen that the tsunami signal is unambiguously present and is well above the noise level in this window (Fig. 4.2, top). The amplitude of the wave is approximately 50 cm, and the width of this segment is on the order of the tsunami wavelength. The Envisat satellite altimeter overflew the leading edge of the tsunami in a window between 17°S and 13°S over an hour after Jason-1 (Fig. 4.2, middle). The amplitude at this later time was close to 30 cm. Four hours later, GFO encountered the leading edge of the tsunami near 40°S (Fig. 4.2, bottom). The amplitude at this time was greatly attenuated with values less than 20 cm. The TOPEX/Poseidon SSH measurements are omitted from the discussion due to data gaps present on the day of the tsunami. By studying the measurements of the tsunami from each of the three satellite altimeters discussed above, a better understanding of how the strength of the tsunami relates to the ability to detect the wave in the open ocean.

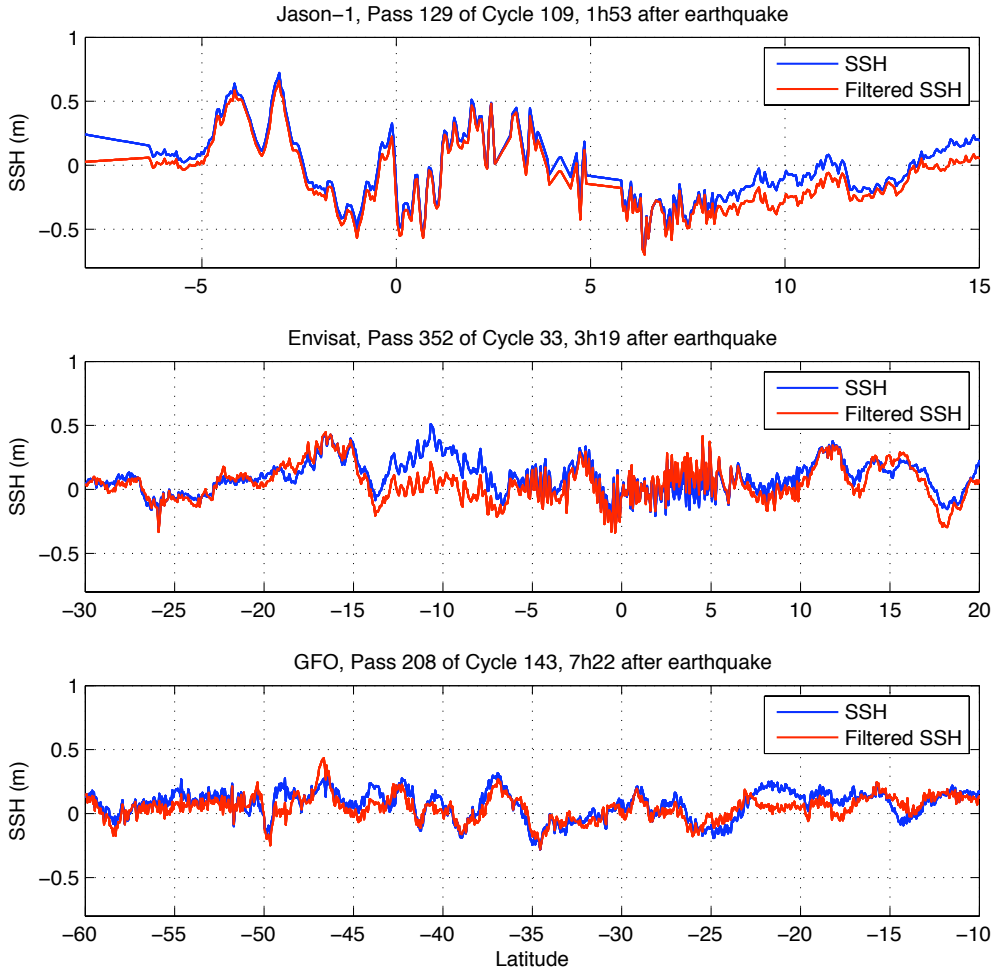

Figure 4.2. SSH measurements, both raw and high-pass filtered (Gower, 2007), taken by the Jason-1 (top), Envisat (middle) and GFO (bottom) satellite altimeters on the day of the 2004 Sumatra-Andaman tsunami.

4.1.2 Analysis of Sea Surface Roughness Measurements

4.1.2.1 Jason-1

The leading front of the tsunami is contained in the window between 6°S and 2°S on Jason-1 pass 129 of cycle 109, with the spatial extent of the segment on the order of the tsunami wavelength. The tsunami signal is clearly present in this window and is well above the noise

level in SSH records (Fig. 4.3A). Data quality in this window is high and there are few data points excluded by quality controls. Radar backscattering strengths measured in both the Ku- and C- microwave frequency bands in the vicinity of the leading front of the tsunami show up to 1 dB variations, which are not present in measurements along the same pass of the cycles before and after the tsunami (Fig. 4.3B, C). Using equations 3.1 and 3.2, and assuming the height of the background logarithmic boundary layer to be H = 50-70 m (Garratt, 1994), we calculate the tsunami period to be T = 35-45 min (Gower, 2007), and a maximum and minimum SSH anomaly of 0.6-0.7m. Values of approximately 1 dB are obtained for the maximum variation of the radar backscattering strength, which is consistent with the values in Figs. 4.3 B and C. A more detailed comparison of the observed to predicted σ_0 variations, however, is not possible because of uncertainty in knowledge of the local meteorological parameters and the tsunami spectrum, and the high sensitivity of the tsunami-induced changes in the surface roughness to poorly known environmental parameters, such as the background wind speed. Despite this difficulty, the σ_0 variations can be attributed to the tsunami by performing statistical randomization tests using historical Jason-1 σ_0 data and comparing to the σ_0 data collected during the passage of the tsunami. Troitskaya & Ermakov (2005; 2008) discussed the Jason-1 σ_0 data obtained during the Sumatra-Andaman tsunami passage, but they did not compare the data to analogous data in the absence of the tsunami.

To perform the randomization tests, one thousand 3.2°-windows centered between 20°S and 10°N were randomly selected in the tropical Indian Ocean from cycles 1-174 of Jason-1. The data were processed as outlined in section 3.2, and the RMS values and the number of zero crossings were calculated for the σ_0 data in each window and compared to the respective values in the window covering 5.6°S to 2.4°S along pass 129 of cycle 109. Only a few percent of the

randomly selected windows simultaneously have equal or larger values of both the RMS σ_0 anomaly and the number of zero crossings. The statistical significance of the hypothesis that surface roughness variations with and without the tsunami are not substantially different is 3.15% and 0.93% when estimated using the Ku- and C-band σ_0 data, respectively (Fig. 4.4).

In addition to detecting the leading wave front of the tsunami where the amplitude of the wave is often the largest, it is important to be able to detect the tsunami away from the leading edge where the magnitude of the tsunami has been diminished. The same data processing techniques was applied to 3.2° non-overlapping windows, which extend from 2.4°S (where the window test above ends) to the north along the Jason-1 pass 129 of cycle 109. Windows that contained data gaps too extensive to apply the processing and filtering techniques were excluded from the subsequent randomization tests. The other two windows that were used for testing ranged from 2.5°S to 0.7°N and from 0.8°N to 4.0°N. For the window beginning at 2.5°S, only 9.1% and 9.7% of the randomly selected windows simultaneously have equal or larger numbers of both RMS σ_0 anomalies and the number of zero crossings in the Ku- and C-bands, respectively. For the window beginning at 4.0°N, only 6.4% and 2.2% of the randomly selected windows had greater RMS σ_0 anomaly and more zero crossings for the Ku- and C-bands, respectively.

These additional randomization tests away from the leading wave front of the tsunami reinforce the evidence of exceptional features in radar backscattering strength in the presence of a tsunami. Furthermore, these results demonstrate that our data processing algorithms allow detection of the tsunami manifestations in the radar backscattering strength for various tsunami waveforms and can successfully discriminate between regions where the tsunami is and is not present.

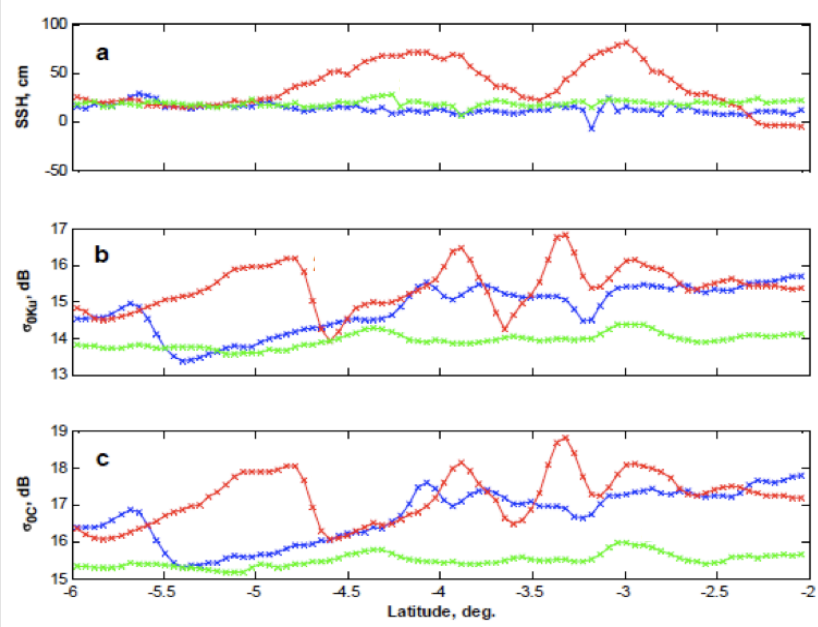

Figure 4.3. Jason-1 data for pass 129 from 6°S to 2°S shown for the cycles before the tsunami (blue), coincident with the tsunami (red) and after the tsunami (green). (a) Sea surface height. (b) Ku-band radar backscattering strength. (c) C-band radar backscattering strength.

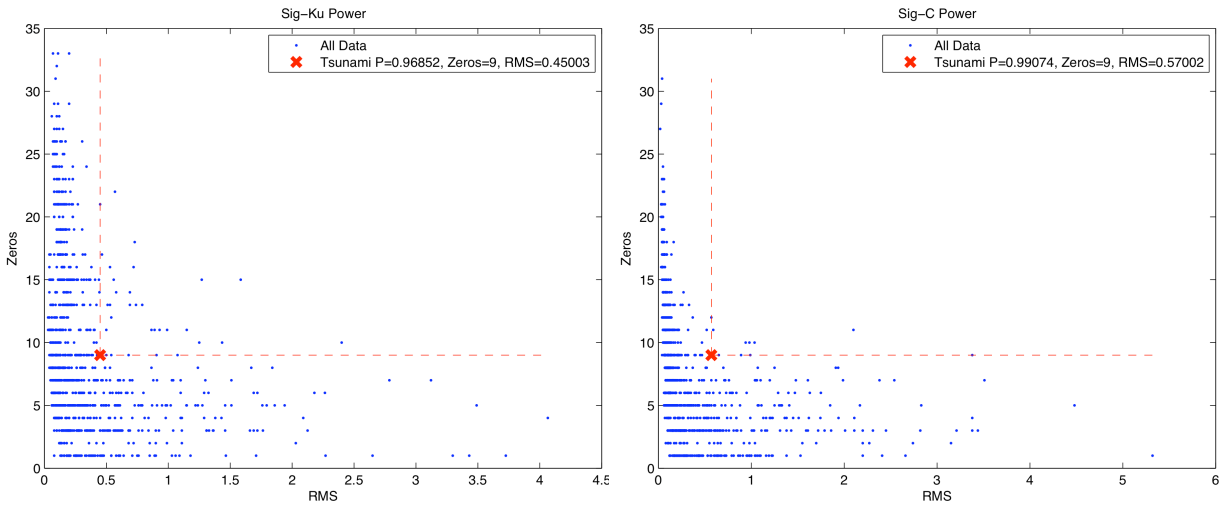

Figure 4.4. Randomization tests of the radar backscattering strength data. (a) Ku-band σ_0 data. (b) C-band σ_0 data. Statistical significance of the hypothesis that surface roughness variations with and without the tsunami are not substantially different is found to be 3.15% and 0.93% for the Ku-band and C-band measurements respectively.

4.1.2.2 Envisat

The Envisat satellite altimeter encountered the leading edge of the tsunami on pass 352 of cycle 33 in the window between 17°S and 13°S. As seen in Fig. 4.2B, the amplitude in this segment was still relatively large, about 30 cm for the first wave. A smaller secondary wave is observed between 12°S and 8°S with amplitude closer to 20 cm. The weaker signal provides a chance to test the efficacy of the randomization tests on the sea surface roughness variations in detecting smaller tsunamis. Instead of selecting a single window containing the leading edge of the tsunami, randomization tests using a "sliding window" across the tsunami altimeter pass are conducted. In other words, a randomization test is conducted for every 3.2° window and the statistical significance that the surface roughness with and without the tsunami is not significantly different is computed. The results of this test are shown in Fig. 4.5 for the Ku-band and Fig. 4.6 for the S-band of the Envisat satellite altimeter. The tsunami wave field spans the region from approximately 17°S to 10°N. For the Ku-band, the statistical significance is generally less than 20% in this region, with the exception being the segment from 15°S to 10°S just behind the leading edge of the tsunami. The results are more promising for the S-band with most of the region having significance levels of less than 10%.

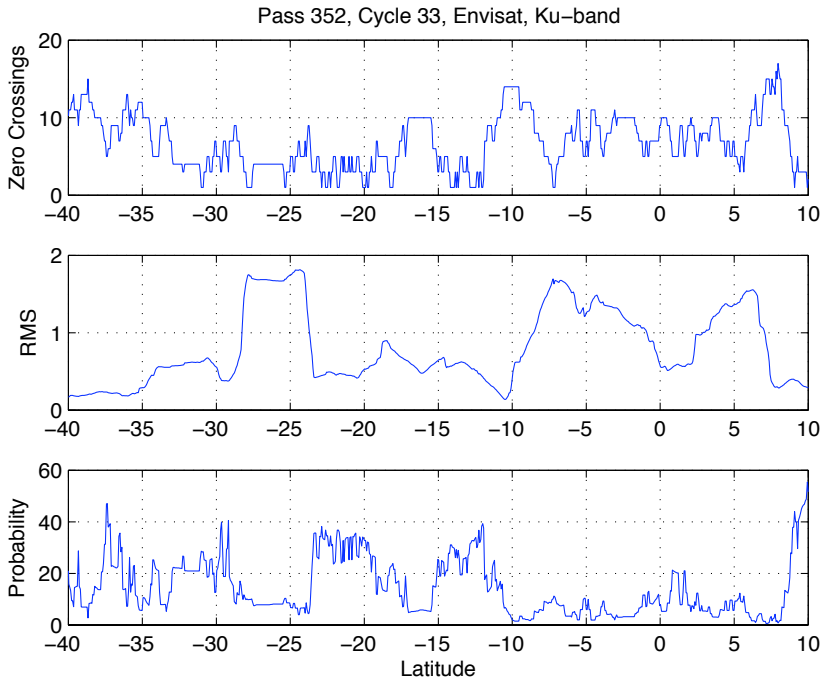

Figure 4.5. Statistical randomization tests on the Ku-band using a "sliding window" for pass 352 of Envisat cycle 33. A randomization test is conducted for every 3.2° window and the statistical significance is computed to test the hypothesis that the surface roughness variations with and without the tsunami present are not significantly different. The x-axis values represent the center point of each window.

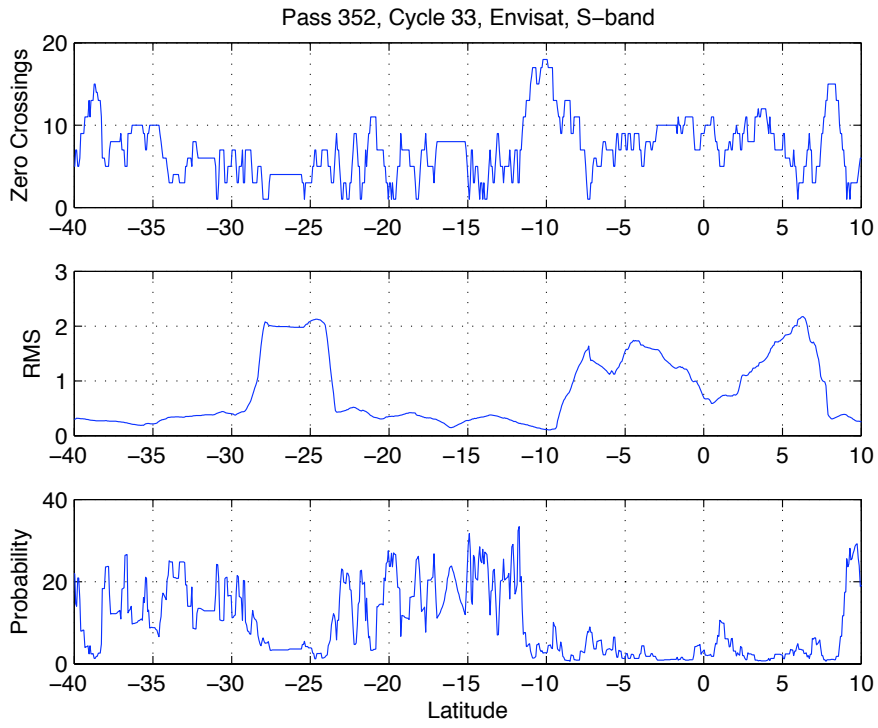

Figure 4.6. Statistical randomization tests on the S-band using a "sliding window" for pass 352 of Envisat cycle 33. A randomization test is conducted for every 3.2° window and the statistical significance is computed to test the hypothesis that the surface roughness variations with and without the tsunami present are not significantly different. The x-axis values represent the center point of each window.

4.1.2.3 Geosat Follow-On

The Geosat Follow-On (GFO) satellite altimeter encountered the leading edge of the tsunami on pass 208 of cycle 143 in the window between 45°S and 40°S. As seen in Fig. 4.2C, the amplitude in this segment was greatly attenuated, about 10 cm for the first wave. A larger secondary wave is observed between 40°S and 35°S with amplitude closer to 20 cm. Again, instead of selecting a single window containing the leading edge of the tsunami, randomization tests using a "sliding window" across the tsunami altimeter pass are conducted. In other words, a

randomization test is conducted for every 3.2° window and the statistical significance that the surface roughness with and without the tsunami is not significantly different is computed. The results of this test are shown in Fig. 4.7 for the Ku-band of the GFO satellite altimeter (GFO was a single frequency altimeter). The tsunami wave field spans the region from approximately 45°S to 5°N. For the Ku-band, the statistical significance is generally around 20% in this region, although values near 50% are attained in some parts of the wave field. These results do not suggest positive identification of the tsunami in the radar backscattering strength measurements of GFO.

4.1.3. 2004 Sumatra-Andaman Tsunami Summary

The 2004 Sumatra-Andaman tsunami was an exceptionally large and strong event. Using statistical randomization tests, it has been shown that the tsunami signature can be positively detected in radar backscattering strength variations for both the Jason-1 and Envisat satellite altimeters. Godin et al. (2009) also uses a spectral approach that performs randomization tests on both SSH and radar backscattering strength variations, which confirms these results, but will not be discussed at length here. Measurements taken by GFO, however, do not lead to positive identification, which is likely a result of the greatly attenuated strength of the tsunami over 7 hours after its initial generation. To answer questions about the ability to detect weaker tsunami signals in sea surface roughness variations, it is important to investigate other tsunami events in the modern altimeter record.

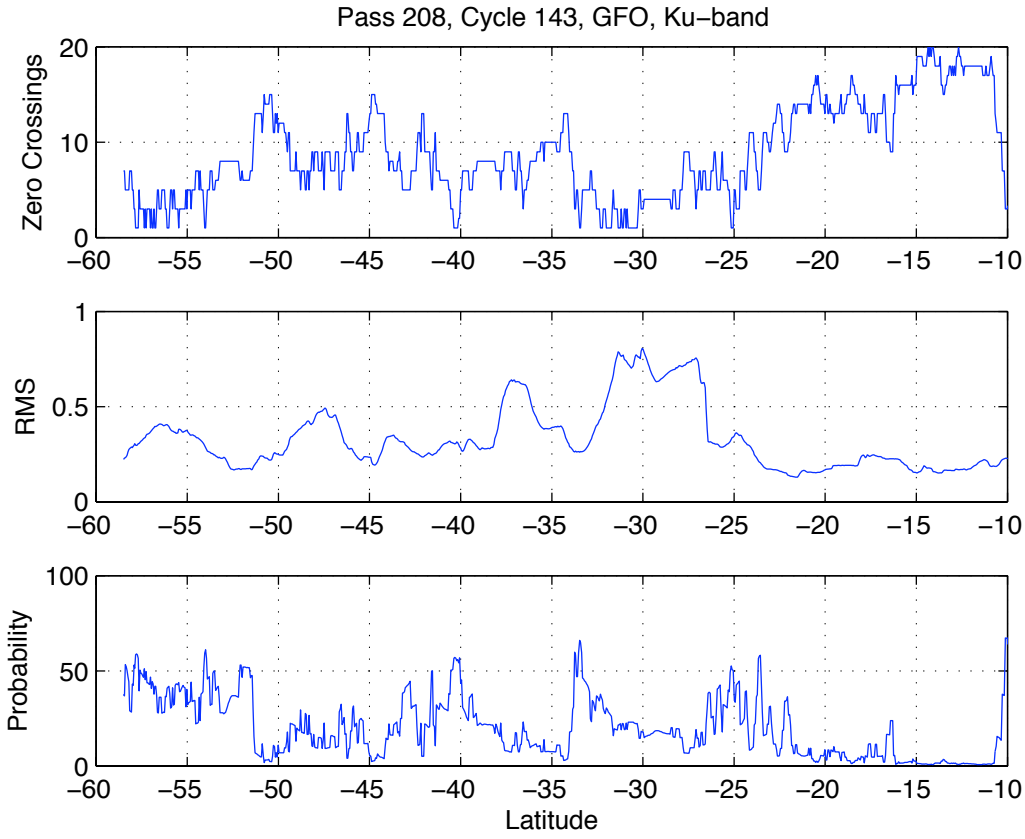

Figure 4.7. Statistical randomization tests on the Ku-band using a "sliding window" for pass 208 of GFO cycle 143. A randomization test is conducted for every 3.2° window and the statistical significance is computed to test the hypothesis that the surface roughness variations with and without the tsunami present are not significantly different. The x-axis values represent the center point of each window.

4.2 2010 Chilean Tsunami

On February 27th, 2010, an earthquake of Mw 8.8 generated a significant tsunami off the coast of Chile. Tsunami waves hit coastal towns in Chile with substantial wave heights and propagated out into the Pacific Ocean, covering large distances. There were multiple satellite altimeters (Jason-1, Jason-2 and Envisat) that overflew the tsunami wave field shortly after the earthquake occurred. Using the SSH and sea surface roughness measurements from these satellite altimeters, the ability of previously employed filtering techniques and statistical analyses to detect the tsunami in the open ocean can be tested. Positive identification would strengthen the confidence in methods and techniques developed in the aftermath of the 2004 Sumatra-Andaman tsunami and would support the ability to detect weaker tsunamis in the open ocean using satellite-based sensors.

4.2.1 Analysis of Sea Surface Height Measurements

There were multiple satellite altimeters that overflew the tsunami wave field shortly after the earthquake occurred. Jason-1 sampled the region affected by the tsunami on several passes of cycle 300 beginning approximately 4 hours after the tsunami occurred on ascending pass 139 (Fig. 4.8). Jason-1 also sampled the tsunami wave field on pass 141 approximately 6 hours after the earthquake, and again on pass 143 approximately 8 hours after the earthquake. Jason-2 sampled the region affected by the tsunami on cycle 61 starting approximately 3 hours after the tsunami occurred on ascending pass 11 (Fig. 4.9). The Jason-2 satellite altimeter also sampled the tsunami wave field on ascending passes 13, 15, and 17 at approximate times of 5, 7 and 9 hours after the tsunami generation, respectively. While the Envisat satellite altimeter also

sampled the region affected by the tsunami, the focus will be on the Jason-1 and Jason-2 satellite altimeters.

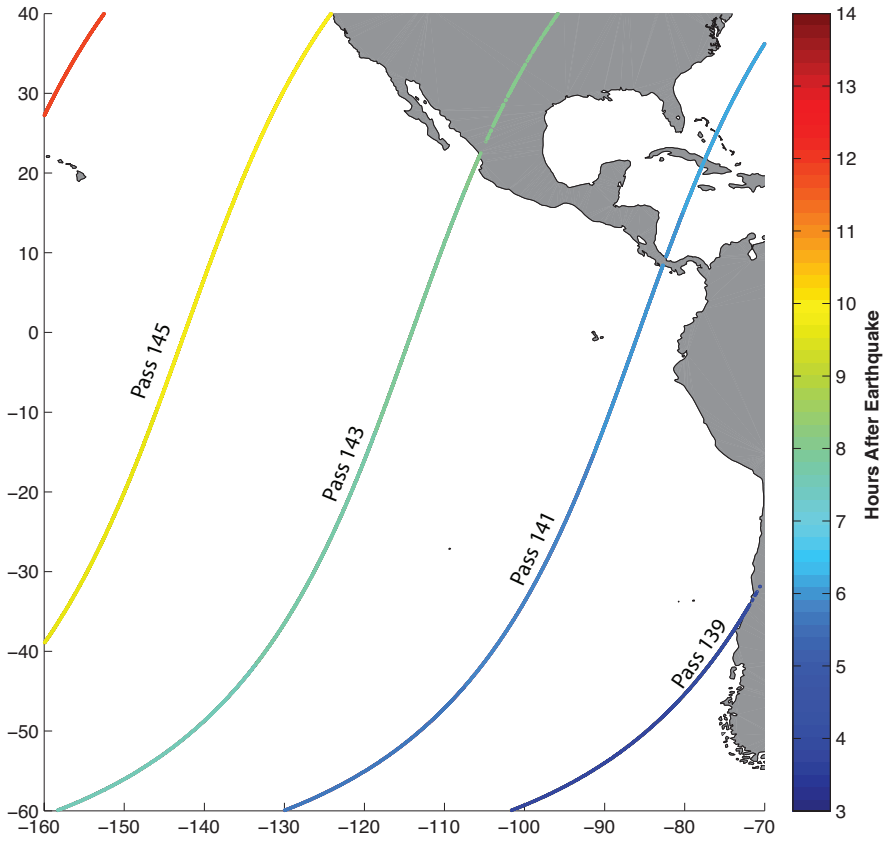

Figure 4.8. Jason-1 passes over the 2010 Chilean tsunami on February 27th, 2010.

Sea surface height measurements were obtained from two separate sources. The satellite altimetry data used in this study was obtained from the Radar Altimeter Database System (RADS). All standard satellite altimetry path-length corrections were applied prior to analysis. To verify the time and location of the tsunami leading edge, the Method of Tsunami Splitting (MOST) model SSH data produced by the NOAA Center for Tsunami Research (Titov et al.,

2005; Titov and Synolakis, 1997) are also used for comparison. The two-dimensional SSH data produced by MOST were interpolated along each altimeter ground-track of interest and compared to the satellite altimetry SSH data. As seen in Fig. 4.8 and Fig. 4.9, the Jason-1 and Jason-2 satellite altimeters both overflew the tsunami wave field multiple times on February 27th, 2010. The focus is on three passes of each satellite altimeter and apply the filtering techniques introduced in chapter 3 in an attempt to extract the tsunami signal from the background SSH variability.

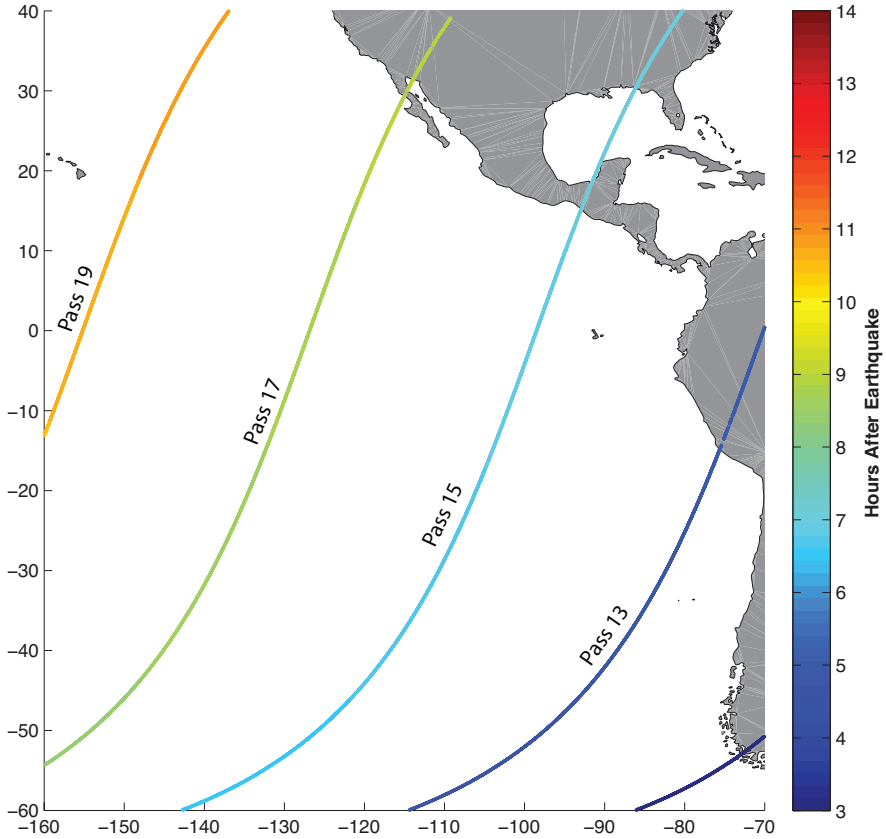

Figure 4.9. Jason-2 passes over the 2010 Chilean tsunami on February 27th, 2010.

4.2.1.1 Jason-1

Jason-1 first sampled the region affected by the tsunami on ascending pass 139 of cycle 300 approximately 4 hours after the tsunami. The top panel of Fig. 4.10 shows the SSH data for pass 139 on cycles 299 and 301 in addition to the SSH data for the tsunami cycle. While an initial check of the SSH data in cycle 300 suggests the presence of a tsunami-like signal around 58°S, this signal is also present in the cycles before and after the tsunami. After using the simple filtering based on the cycles immediately before and after the tsunami that was introduced in section 2, the signal around 58°S is attenuated and only weaker features remain (Fig. 4.10B). By subsampling the results provided by the MOST model along this pass, a comparison can be made between the filtered SSH measurements and the predicted model results. The MOST model suggests that the altimeter should have encountered the leading edge around 57°S, but this is not decisively confirmed by the satellite altimeter data.

Similar results are obtained when looking at pass 141 of cycle 300, sampling the tsunami approximately 6 hours after the generation of the tsunami. SSH data for the tsunami cycle and the cycles before and after the tsunami are shown in Fig. 4.11A. Again, a relatively large signal around 58°S is observed, but once the filtering is implemented, this signal is weakened and positive identification of the tsunami cannot be made. Furthermore, comparison to the MOST model data demonstrates only a weak agreement and suggests the presence of wave amplitudes on the order of 10 cm. The more complex filtering introduced by Ablain et al. (2006) has not been shown for these two passes since similarly poor results are obtained and there is no definitive positive identification.

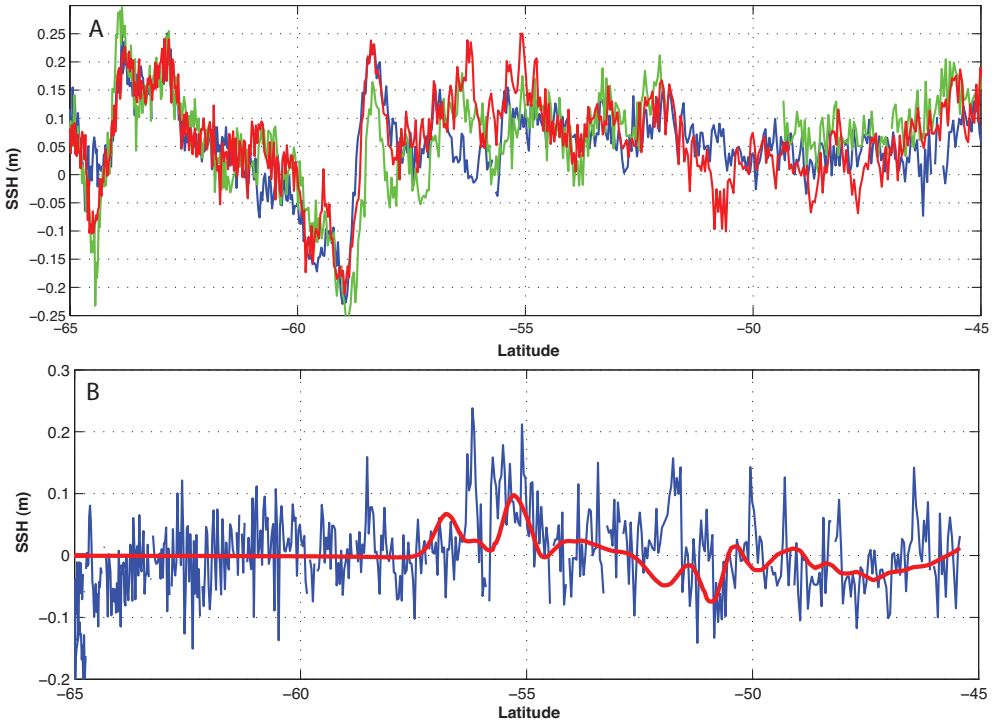

Figure 4.10. (A) SSH data for pass 139 of Jason-1 cycles 299 (blue), 300 (red - tsunami) and 301 (green). (B) Filtered SSH data (blue) for pass 139 of cycle 300 with MOST model results (red) overlaid.

Pass 143 of cycle 300 sampled the tsunami wave field at just less than 8 hours after the tsunamigenic earthquake occurred. A large tsunami-like signal can be seen at 15°S in cycle 300 that is not present in the cycles immediately before and after (Fig. 4.12A). Indeed, once filtering is applied, this feature appears very prominently in the resulting SSH signal with amplitude close to 30 cm. The MOST model suggests a similar location and amplitude for the leading edge of the tsunami signal although with a substantially different wavelength, a feature that will be discussed further later.

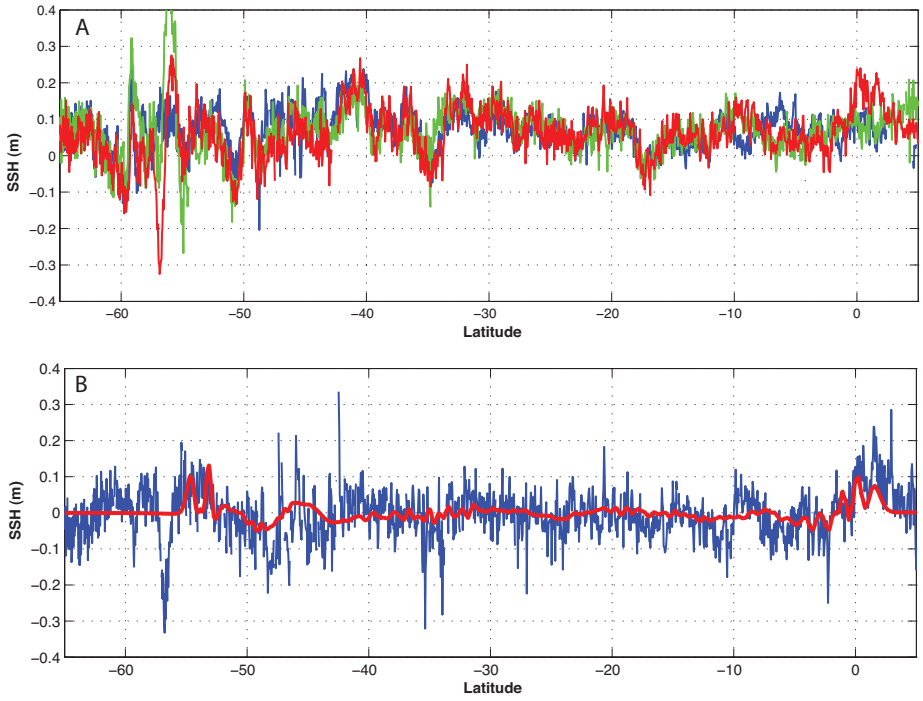

Figure 4.11. (A) SSH data for pass 141 of Jason-1 cycles 299 (blue), 300 (red - tsunami) and 301 (green). (B) Filtered SSH data (blue) for pass 141 of cycle 300 with MOST model results (red) overlaid.

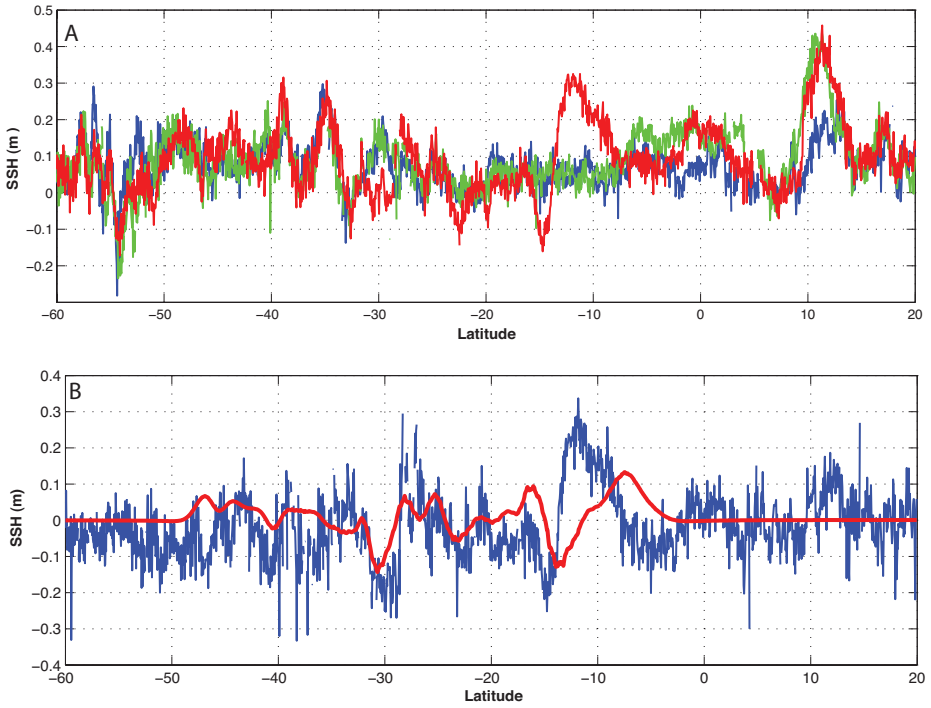

Figure 4.12. (A) SSH data for pass 143 of Jason-1 cycles 299 (blue), 300 (red - tsunami) and 301 (green). (B) Filtered SSH data (blue) for pass 143 of cycle 300 with MOST model results (red) overlaid.

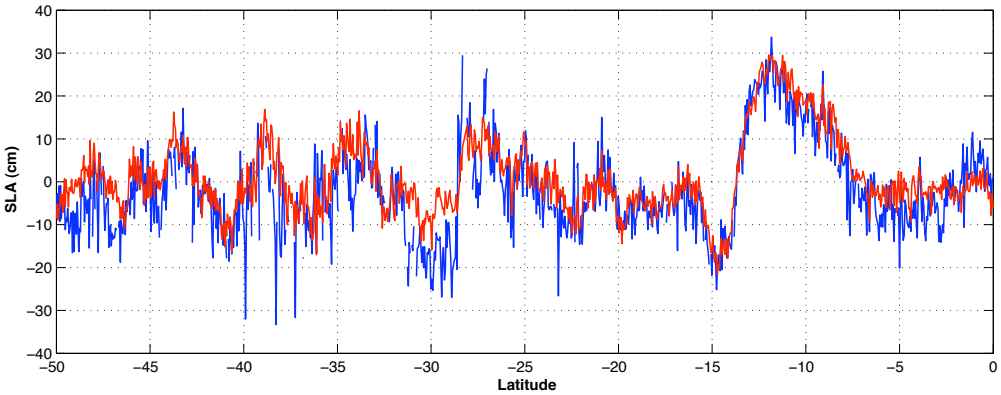

Figure 4.13. Filtered SSH for pass 143 of cycle Jason-1 cycle 300 using the Gower (2007) technique (blue) and the Ablain et al. (2006) technique (red).

After the positive identification from the simple filtering technique, the mapping technique of Ablain et al. (2006) is applied to determine the results obtained from a more sophisticated filtering technique. Fig. 4.13 shows the comparison between the filtered SSH obtained from the Gower (2007) technique and the filtered SSH obtained from the Ablain et al. (2006) technique. Both techniques capture the significant tsunami signal at 15°S, implying positive identification of the tsunami can be made using both techniques. However, a significant difference in the two filtering techniques is seen near 30°S. The simpler filtering technique yields a feature with amplitude approaching 20 cm, while the mapping filter technique yields a much weaker signal. The fact that the more sophisticated technique is theoretically able to better remove the ocean variability suggests that this feature is not associated with the tsunami. Regardless, in contrast to passes 139 and 141, the tsunami signal has been unambiguously extracted from pass 143 of Jason-1 cycle 300.

4.2.1.2 Jason-2

The Jason-2 satellite altimeter first encountered the region affected by the tsunami at high latitude along ascending pass 11 of cycle 61 approximately 3 hours after the tsunami. Due to the limited sampling of the area before reaching the South American coast along pass 11 (Fig. 4.9), we forego analysis and begin our study on pass 13, occurring roughly 5 hours after the tsunami was generated. Fig. 4.13A shows the SSH measurements taken along pass 13 of cycles 60, 61 and 62. Once the filtering is applied, only amplitudes less than 10 cm are observed after the tsunami arrival (Fig. 4.13B). The MOST model provides a leading edge location around 57°S,

but it is difficult to ascertain the location of the leading edge from the filtered SSH data due to the low amplitudes of the variations.

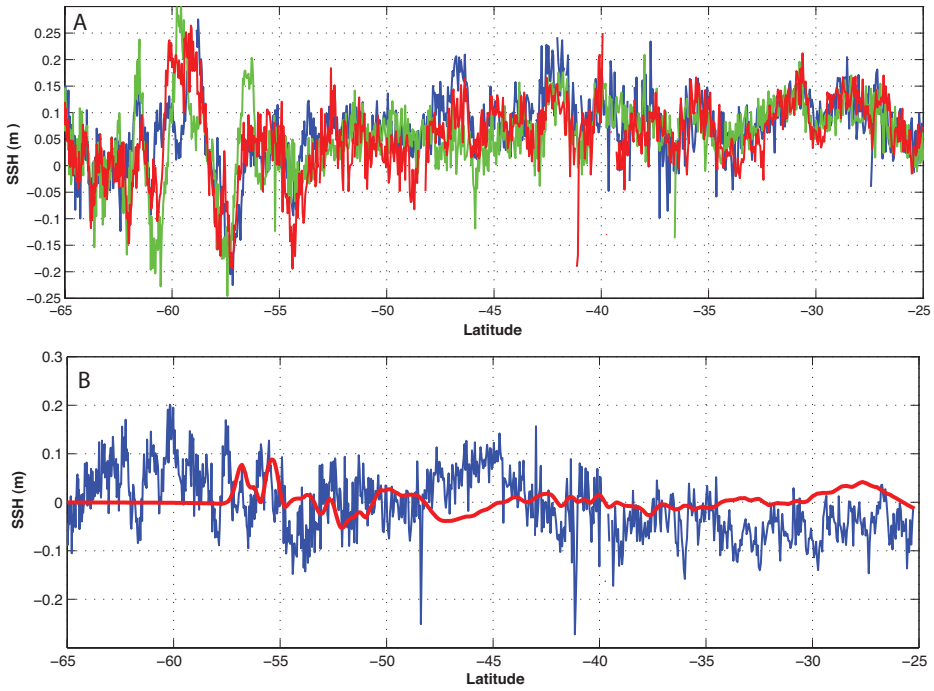

Figure 4.14. (A) SSH data for pass 13 of Jason-2 cycles 60 (blue), 61 (red - tsunami) and 62 (green). (B) Filtered SSH data (blue) for pass 13 of cycle 61 with MOST model results (red) overlaid.

Jason-2 also sampled the tsunami wave field on passes 15 and 17 approximately 7 and 9 hours, respectively, after the generation of the tsunami. Figs. 4.15A shows the SSH for pass 15 for the tsunami cycle and the cycles immediately before and after. The MOST model results show a leading edge location around 50°S, but this is not similarly represented in the filtered SSH (Fig. 4.15B). Additionally, while the filtered SSH data and MOST model data provide similar locations for the leading edge, the amplitudes are much less than 10 cm. Fig. 4.16 shows

similar results for pass 17 of Jason-2 cycle 61 with amplitudes close to 5 cm but with good agreement between the filtered SSH and MOST model data.

None of the three Jason-2 passes over the tsunami allow for a definitive positive identification of the tsunami wave. While some agreement is seen between the MOST model data and the filtered SSH data in terms of the location of the tsunami leading edge, the amplitude of the tsunami wave at these locations is very small making it difficult to fully separate the signal from the background noise and ocean variability. Filtering using the Ablain et al. (2006) mapping technique has yielded similarly poor results and will thus not be shown in detail here.

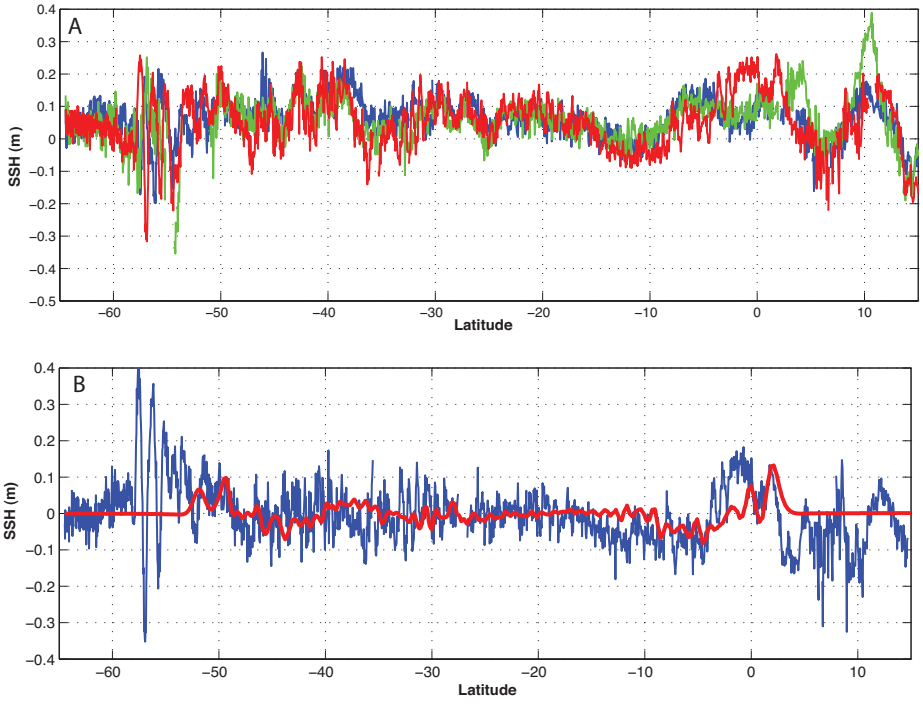

Figure 4.15. (A) SSH data for pass 15 of Jason-2 cycles 60 (blue), 61 (red - tsunami) and 62 (green). (B) Filtered SSH data (blue) for pass 15 of cycle 61 with MOST model results (red) overlaid.

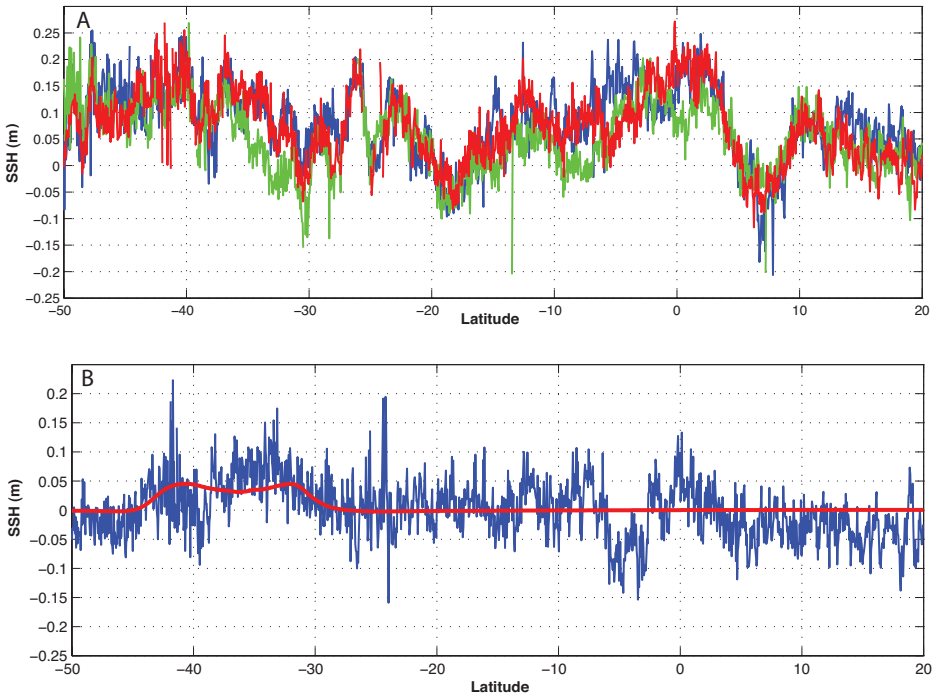

Figure 4.16. (A) SSH data for pass 17 of Jason-2 cycles 60 (blue), 61 (red - tsunami) and 62 (green). (B) Filtered SSH data (blue) for pass 17 of cycle 61 with MOST model results (red) overlaid.

4.2.2 Analysis of Sea Surface Roughness Measurements

With the positive identification of the tsunami signal in pass 143 of Jason-1 cycle 300, a 3.2°-window is selected surrounding the leading front of the tsunami. The window selected is from approximately 16°S and 12°S, with the spatial extent of the segment on the order of the tsunami wavelength. The tsunami is clearly present in this window with amplitude of greater than 20 cm (Fig. 4.12). Data quality in the window is high and there are few data points excluded by quality controls. Radar backscattering strengths measured in both the Ku and C microwave frequency bands in the vicinity of the leading front of the tsunami do not show variations as strong as those observed for the 2004 Sumatra-Andaman tsunami. This is not surprising or unexpected, however, given the great disparity in the strength of the two tsunamis.

The statistical randomization tests on the sea surface roughness data were conducted by randomly selecting one thousand 3.2° windows centered between 50°S and 10°N in the Pacific Ocean from cycles 1-305 of Jason-1. The data was processed as outlined in section 2, and the RMS values and the number of zero crossings were calculated for the σ_0 data in each window. These values were then compared to the respective values in the window covering 15.2°S to 12°S along pass 143 of cycle 300. The statistical significance of the hypothesis that the surface roughness variations with and without the tsunami are not substantially different is 0.7% and 21.9% when estimated using the Ku-band and C-band σ_0 data, respectively (Fig. 4.17). While the randomization test on the Ku-band on the radar backscattering strength yielded positive identification at the 1% significance level, 30 zero crossings and an RMS σ_0 anomaly of only 0.20 dB were found for the window containing the leading front of the tsunami. The primary reason for the high significance level is the large number of zero crossings. Given the physical characteristics of the tsunami and the theoretical explanation of the tsunami-induced variations in sea surface roughness, fewer zero crossings are expected. Using the model outlined in Godin et al. (2009), the expected σ_0 anomaly RMS values can be theoretically predicted for pass 143 of cycle 300. With wind speeds between 7-14 m/s in the region as measured by the Special Sensor Microwave/Imager (SSM/I) instrument on the day of the tsunami, water depths between 3 and 8 km, tsunami wave periods ranging from 30 to 60 minutes, and a tsunami wave amplitude of roughly 0.2 m, σ_0 anomaly RMS values are theoretically predicted to range between 0.1 and 0.2 dB. This shows excellent agreement with the observed σ_0 anomaly RMS values of 0.20 dB for the Ku-band and 0.12 dB for the C-band.

The statistical randomization tests conducted suggest that the leading front of the tsunami is detectable in sea surface roughness measurements. In theory, however, the tsunami signal

should be detectable at other locations within the tsunami wave field. To test this, randomization tests are conducted using a "sliding window" across the tsunami altimeter pass. In other words, a randomization test is conducted for every 3.2° window and compute the statistical significance that the surface roughness variations with and without the tsunami are not significantly different. The results of this test are shown in Fig. 4.18, with the x-axis values representing the center point of each window. Fig. 4.12 shows that the tsunami wave field spans the region from approximately 45°S to 5°S. The statistical significance is generally less than 20% in this region.

For comparison, the same "sliding window" test can be applied to other altimeter passes in which the leading front of the tsunami was not positively identified in the SSH data. Fig. 4.19 shows the results for pass 141 of Jason-1. The significance level in the region over the estimated tsunami wave field has large variability and is well over 20% in many locations. Similarly, pass 15 of Jason-2 (Fig. 4.20) has generally high significance levels over the region of interest. Poor results are also obtained for the other satellite altimeter passes discussed in section 3.1.

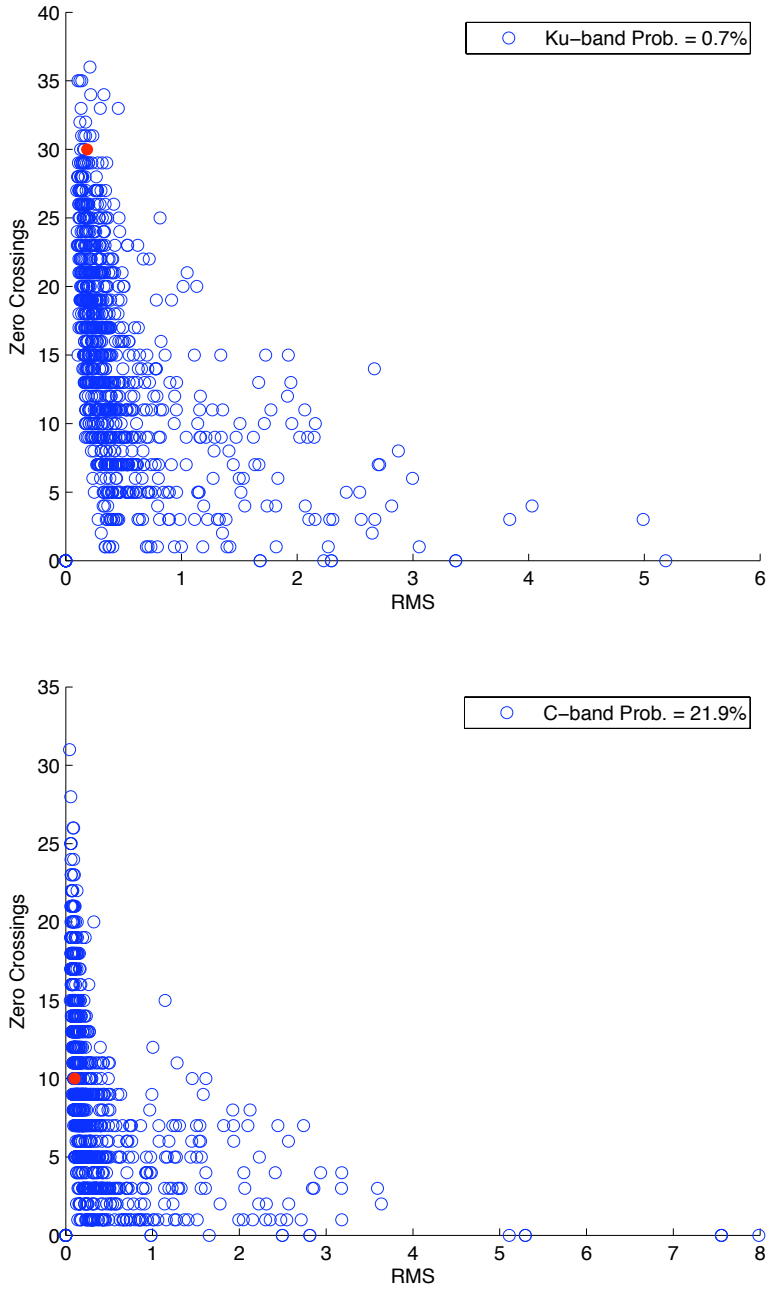

Figure 4.17. Results from the statistical randomization tests on the radar backscattering strength for pass 143 of Jason-1 cycle 300. Statistical significance of the hypothesis that surface roughness variations with and without the tsunami are not substantially different is found to be 0.7% and 21.9% for the Ku-band and C-band measurements respectively.

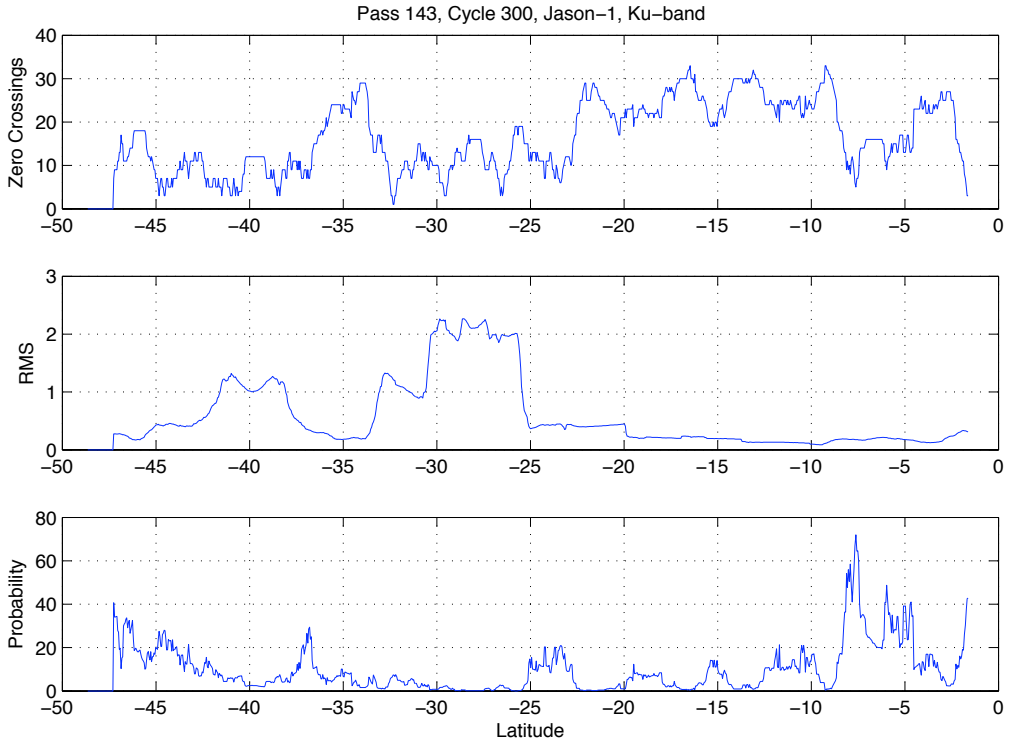

Figure 4.18. Statistical randomization tests using a "sliding window" for pass 143 of Jason-1 cycle 300. A randomization test is conducted for every 3.2° window and the statistical significance is computed to test the hypothesis that the surface roughness variations with and without the tsunami present are not significantly different. The x-axis values represent the center point of each window.

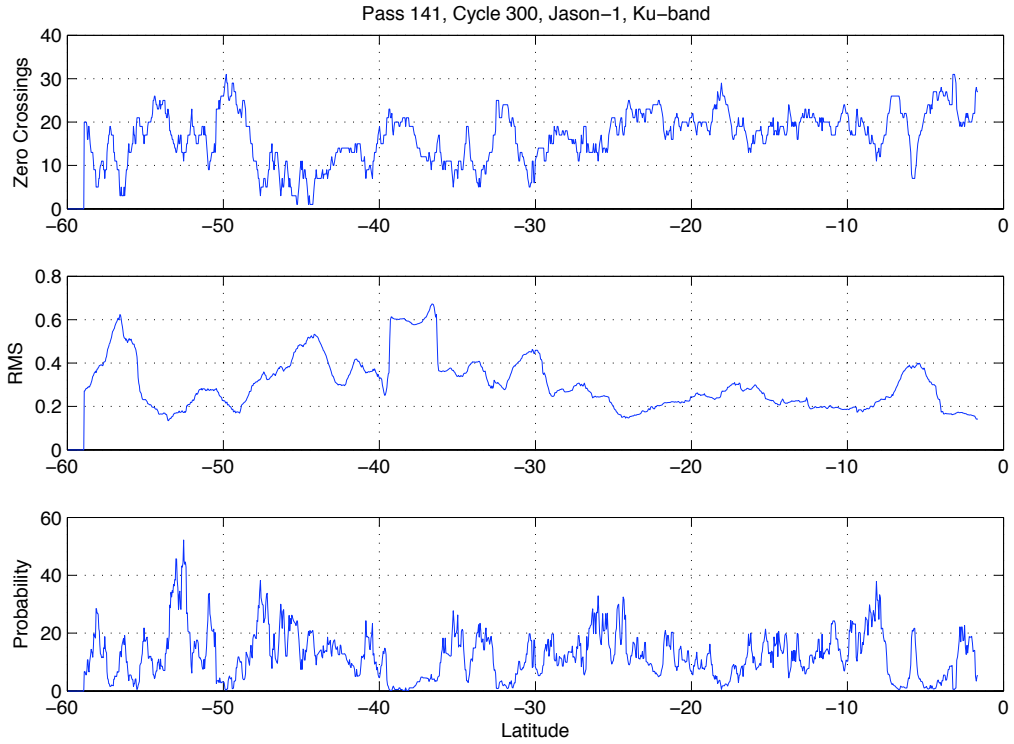

Figure 4.19. Statistical randomization tests using a "sliding window" for pass 141 of Jason-1 cycle 300. A randomization test is conducted for every 3.2° window and the statistical significance is computed to test the hypothesis that the surface roughness variations with and without the tsunami present are not significantly different. The x-axis values represent the center point of each window.

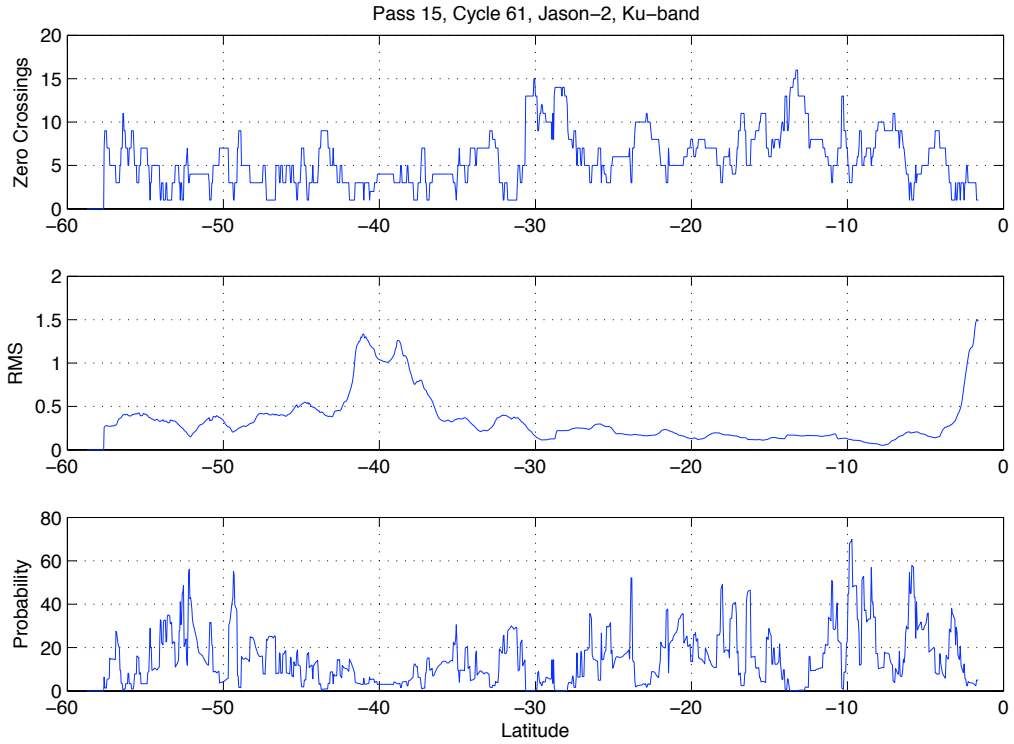

Figure 4.20. Statistical randomization tests using a "sliding window" for pass 15 of Jason-2 cycle 61. A randomization test is conducted for every 3.2° window and the statistical significance is computed to test the hypothesis that the surface roughness variations with and without the tsunami present are not significantly different. The x-axis values represent the center point of each window.

4.2.3 Summary and Discussion of 2010 Chile Tsunami

To summarize the results above, the SSH signal associated with the 2010 Chile tsunami has been positively identified in only one satellite altimeter pass, specifically pass 143 of Jason-1 cycle 300. Two other Jason-1 passes and three Jason-2 passes were also analyzed but were unable to definitively detect the tsunami signal in the filtered SSH data. One reason why it was not possible to extract the tsunami from the background variability is the location that the satellite altimeter encountered the tsunami wave. For most of the passes, the satellite altimeter overflew the leading edge of the tsunami at very high latitude (~60°S) in the Southern Ocean,

within the Antarctic Circumpolar Current. Significant mesoscale activity is present in this region (Fu and Cazenave, 2001), contributing large amplitude variability to the SSH measurements and decreasing the probability of observing the tsunami signal in the background ocean variability. Not surprisingly, the only location where the tsunami was unambiguously present and identified in the SSH measurements was near 15°S.

One way to improve our ability to extract the tsunami signal from the background ocean variability is to filter the data prior to analysis. Gower (2007) and Ablain et al. (2006) use filtering techniques to identify the leading edge of the 2004 Sumatra-Andaman tsunami. These filtering techniques made use of the satellite altimeter measurements before and after the tsunami occurred to remove more persistent signals with longer timescales than the tsunami wave. Although the filtering enhanced the tsunami signal relative to the background variability, the Sumatra-Andaman tsunami had significant amplitude even in the open ocean, making it possible to identify without high-pass filtering the data. Attempting to detect a weaker tsunami provides a much more stringent examination of the filtering techniques. The simple technique presented by Gower (2007) shows very close agreement with the more complex filtering of Ablain et al. (2006). Along pass 143 of Jason-1 cycle 300, the satellite altimeter samples the leading edge of the tsunami twice, once between 50°S and 30°S, and then again around 15°S. A significant tsunami-related signal is seen around 30°S, although the amplitude is attenuated when comparing the results from the Ablain et al. (2006) filtering to the Gower (2007) filtering. This leads to the possibility that the more sophisticated technique could serve to over-smooth the data and thus underestimate the amplitude of the tsunami wave. Regardless, the good agreement between the results produced by the two filtering techniques suggests that the method proposed by Gower

(2007) may be adequate for extracting the tsunami SSH signal from the background variability, even for weaker tsunamis.

One significant advantage of the Gower (2007) filtering is the ability to use such a technique in real-time. The Ablain et al. (2006) filtering method requires 40 days of satellite altimetry data both before and after the tsunami occurs. This data is used to map the ocean variability without the tsunami present, and differencing with the satellite altimeter pass containing the tsunami signal enhances the tsunami signal within the SSH measurements. The Gower (2007) technique, however, only requires the cycle before and after the tsunami to filter the SSH measurements and extract the tsunami signal, and one could easily adjust such a method to only use the data before the tsunami occurs. This would allow the filtering to be applied as soon as a tsunami occurs and satellite altimeter measurements become available. Fig. 4.21 shows the comparison between filtering the SSH measurements from Jason-1 pass 143 using the cycles before and after the tsunami cycle and alternatively using a weighted average of the two cycles before the tsunami cycle (cycle immediately before tsunami is given twice the weight of the cycle two cycles prior to the tsunami). The two filtering techniques yield very similar results, implying that the two cycles prior to the tsunami could be used without a great loss of effectiveness, thus allowing for such filtering to be applied in real-time.

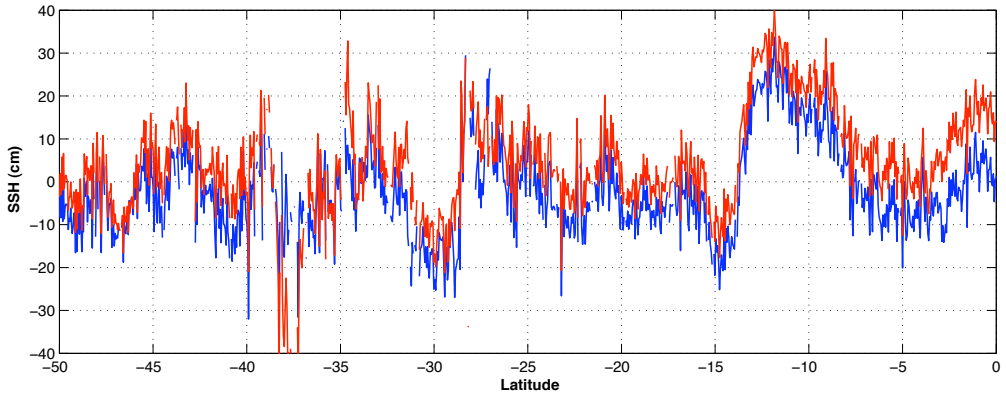

Figure 4.21. Filtered SSH for pass 143 of Jason-1 cycle 300 using the Gower (2007) filtering technique. In addition to using the cycles before and after tsunami for filtering (blue), the two cycles before the tsunami cycle are used (red), suggesting that such filtering techniques could be used in real-time.

In addition to filtering, an important tool for extracting the tsunami signal from the SSH measurements is comparison to the MOST model results. In general, the filtered signals agree well with the MOST model results for the Chile tsunami and, in particular, from the model results we are able to confirm the location of the leading edge in Jason-1 pass 143 of cycle 300 near 15°S. The spatial extent of the leading edge, however, differs significantly between the filtered Jason-1 signal and the results from the MOST model. This is likely a result of the oblique sampling of the tsunami by the Jason-1 satellite altimeter. The Jason-1 ground-track of pass 143 did not enter very far into the tsunami wave field and stayed close to the leading front of the tsunami as the wave propagated across the Pacific Ocean and the altimeter traveled north along pass 143. Fig. 4.22A shows the MOST model results at the approximate time Jason-1 entered the tsunami wave field, while Fig. 4.22B shows the model results at the time the satellite altimeter departed the tsunami wave field (the time delay between Fig. 4.22A and Fig. 4.22B is approximately 15 minutes). As a result of the oblique sampling, a small time difference between reality and the model could result in a considerable change in the estimated location and spatial

extent of the leading edge of the tsunami. Furthermore, the ground-track of the altimeter must be taken into consideration when trying to estimate the wavelength of the tsunami. An altimeter traveling perpendicularly to the tsunami wave front would provide a much different estimate of the wavelength when compared to an altimeter moving more tangentially to the tsunami wave front. This underscores some of the difficulties faced in using satellite altimeters for tsunami detection in the open ocean.

By using measurements of the tsunami-induced changes in sea surface roughness, the limitations imposed by the sampling of satellite altimeters can be overcome. Variations in surface roughness can be detected using orbiting active (scatterometers) and passive (radiometers) scanning microwave sensors, which have broad coverage of hundreds of kilometers across the satellite ground track. In addition to having broader coverage across the satellite ground-track and better temporal sampling characteristics, an instrument sampling the tsunami in two dimensions would provide additional benefits to the detection of the tsunami in the open ocean. Spatial averaging of radar backscattering strength along hypothetical tsunami wave fronts could be used to better separate the tsunami signal from the background noise. Furthermore, a series of two-dimensional snapshots of the tsunami wave field would allow tsunami-related features to be distinguished by their uniquely fast propagation speed in the open ocean.

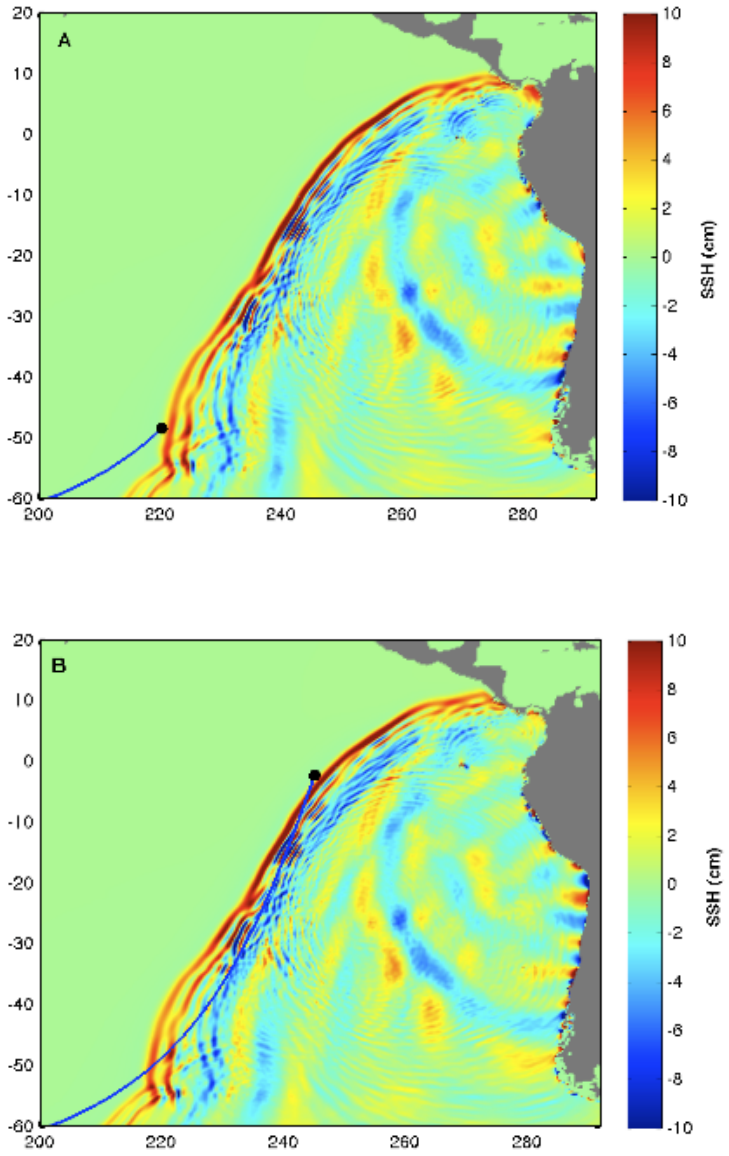

Figure 4.22. MOST model results at the time Jason-1 entered the tsunami wave field on pass 143 (according to the model) (A) and at the time Jason-1 departed the tsunami wave field (B). The time between the two images is ~ 15 minutes. The oblique sampling of the leading front of the tsunami by Jason-1 provides a possible explanation for the discrepancy between model results and Jason-1 data as seen in Fig. 4.12.

While the 2004 Sumatra-Andaman tsunami was detectable in the open ocean from radar backscattering strength measurements, the tsunami was particularly strong and questions remain about the ability to extract the signal from a weaker tsunami. The extensive satellite altimeter coverage of the 2010 Chilean tsunami provided an opportunity to use the statistical randomization tests outlined in Godin et al. (2009) for the detection of the tsunami in the radar backscattering measurements. As seen above, the tsunami was detected with a high degree of certainty in pass 143 of Jason-1 cycle 300, but the results for other passes were inconclusive. The theoretical expectation for the tsunami-induced variation in sea surface roughness is dependent upon the tsunami-induced variations in SSH measurements. In other words, large SSH variations in the open ocean will lead to large variations of the radar backscattering strength. Thus, it is not surprising that the ability to detect the tsunami in the radar backscattering strength coincided with the highest amplitude SSH observations of the tsunami.

4.3 Other Past Tsunamis

While the tsunami-induced variations have been positively detected in ocean surface roughness for the 2004 Sumatra-Andaman tsunami, we have more tentatively identified the tsunami-induced variations for the 2010 Chile tsunami, raising questions about the ability to detect weaker tsunami signals. Okal et al. (1999) studied seven other tsunami events using satellite altimetry. Using only SSH measurements, one tsunami (1992 Nicaragua Tsunami) was positively detected and another tsunami (1995 Chile tsunami) was tentatively detected. Using the statistical randomization tests, an attempt can be made to detect the tsunami-induced variations in ocean surface roughness.

The 1992 Nicaragua tsunami was generated by a "tsunami earthquake," i.e., an earthquake that produces an unusually large tsunami relative to the earthquake magnitude due to a slow rupture (Kanamori & Kikuchi, 1972). The ERS-1 satellite altimeter sampled the tsunami wave field on passes 523 and 525 of cycle 87. Both tracks sampled the tsunami about 3.5 and 5.5 hours after the tsunamigenic earthquake, respectively. Okal et al. (1999) determined that the tsunami signal could not be detected in pass 523 and focused their attention on 525. ERS-1 entered the tsunami wave field around 17°S, with wave amplitudes seen in the SSH of less than 10 cm (Fig. 4.23). Variations in the radar backscattering strength were around 0.5 dB.

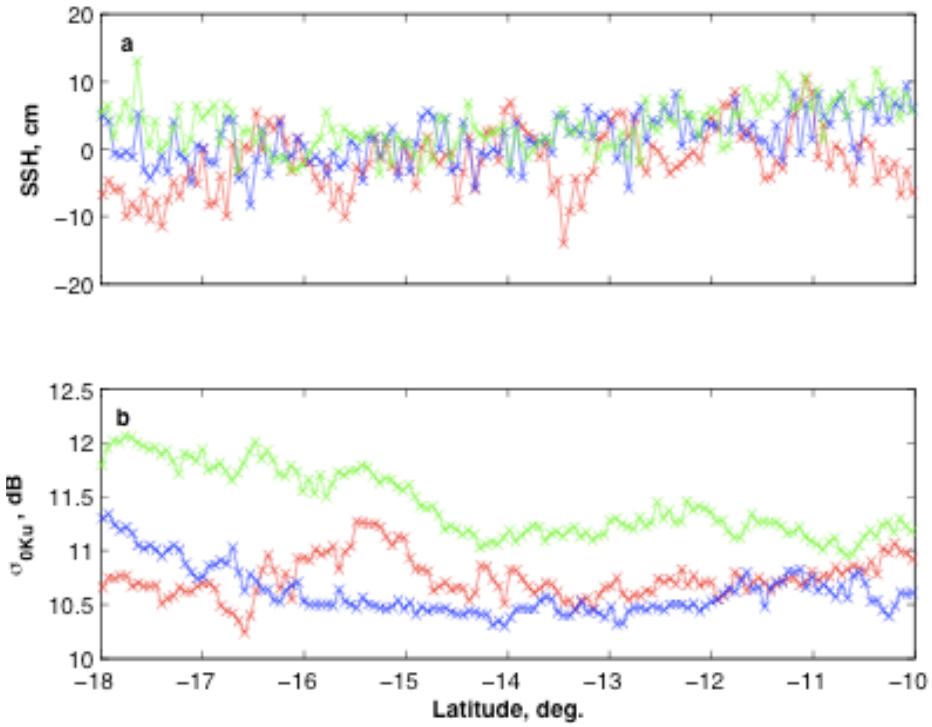

Figure 4.23. ERS-1 data for pass 525 from 18°S to 10°S shown for the cycles before the 1992 Nicaragua tsunami (blue), coincident with the tsunami (red), and after the tsunami (green). (a) Sea surface height. (b) Ku-band radar backscattering strength.

To perform the randomization tests, one thousand 3.2° windows between 40°S and 20°N were randomly selected in the Pacific Ocean from cycles 83-101 of ERS-1. The data was processed as outlined in section 3.2, and the RMS values and the number of zero crossings were calculated for the σ_0 data within each window and compared to the respective values in the window covering 17.0°S to 13.8°S along pass 525 of cycle 87. The statistical significance of the hypothesis that the surface roughness variations with and without the tsunami are not substantially different is 2.6% when estimated using the Ku-band σ_0 data. This suggests a positive identification of the tsunami signal from variations in ocean surface roughness.

As mentioned above, Okal et al. (1999) tentatively identified the 1995 Chile tsunami from SSH measurements. A relatively large earthquake generated a tsunami with run-ups of 2 m in the Marquesas Islands. The TOPEX/Poseidon satellite altimeter sampled the tsunami wave field along two passes (230 and 232) of cycle 105, 3 and 5 hours after the earthquake occurred. The tsunami signal was not detected in pass 230, but there was tentative identification of the tsunami in pass 232. Okal et al. (1999) estimate that TOPEX/Poseidon entered the tsunami wave field around 36°S and exited the wave field around 25°S. SSH wave amplitudes in this region were found to be only 10 cm with maximum variations in the radar backscattering strength of approximately 0.4 dB (Fig. 4.24). Additionally, comparing the SSH data from the cycles before and after the one coincident with the tsunami show very little variation in SSH from cycle to cycle. When using these cycles to filter the target cycle, only a small signal with amplitude of much less than 10 cm remains near 27°S.

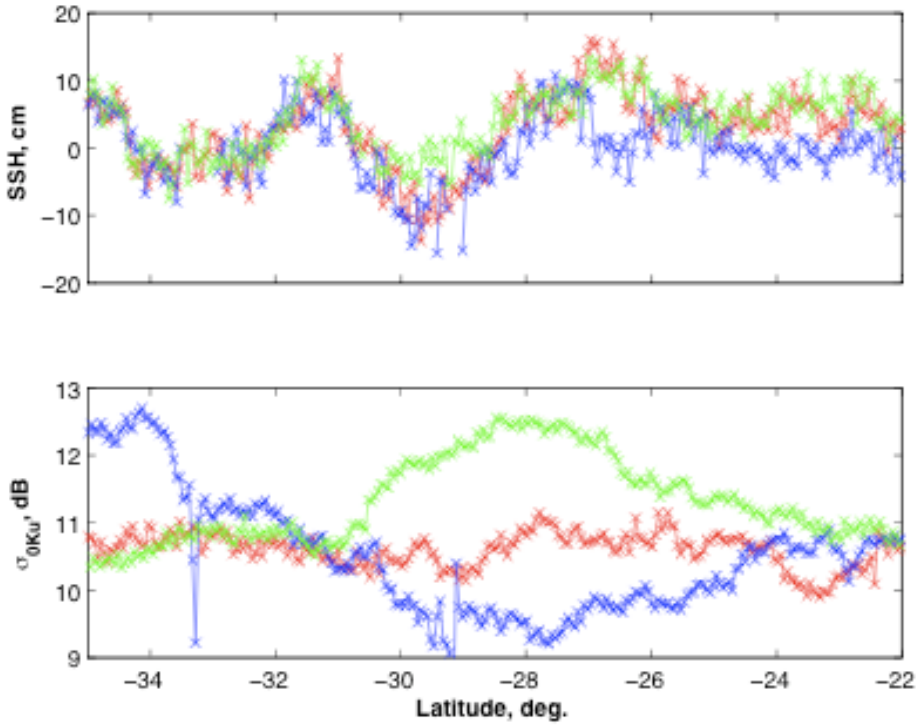

Figure 4.24. TOPEX/Posedion data for pass 232 from 35°S to 22°S shown for the cycles before the 1995 Chile tsunami (blue), coincident with the tsunami (red), and after the tsunami (green). (a) Sea surface height. (b) Ku-band radar backscattering strength.

Randomization tests were performed by randomly selecting one thousand 3.2°-windows centered between 50°S and 10°N in the Pacific Ocean from cycles 50-200 TOPEX/Posedion. The data was processed as outlined in section 3.2, and the RMS values and the number of zero crossings were calculated for the σ_0 data in each window and compared to the respective values in the window covering 29.0°S to 25.8°S along pass 232 of cycle 105. The statistical significance of the hypothesis that the surface roughness variations with and without the tsunami are not substantially different is 2.5% when estimated using the Ku-band σ_0 data. This suggests a positive identification of the tsunami signal from the variations in ocean surface roughness.

CHAPTER 5: DISCUSSION

5.1 Feasibility of tsunami early detection and warning

The use of radar backscattering strength measurements for the detection of a tsunami in the open ocean has been positively demonstrated for the 2004 Sumatra-Andaman tsunami and tentatively demonstrated for the 1992 Nicaragua tsunami, 1995 Chile tsunami, and 2010 Chile tsunami. Satellite altimeters provide concurrent measurements of SSH and σ_0 allowing for the identification of the leading edge in SSH and subsequent testing of this leading edge using randomization tests on σ_0 measurements. While the four tsunamis mentioned above were well sampled by satellite altimeters, historically satellite altimeter measurements of tsunamis are uncommon. Even with several satellites on orbit, nadir-pointing satellite altimeters do not provide the ground track coverage necessary to ensure sampling of a tsunami wave field. Furthermore, as the results above show, even if timely sampling of the tsunami was available in real time, separating the tsunami signal from the background ocean variability is difficult. The use of satellite altimeters as the foundation for an early detection system is not plausible.

While radar backscattering measurements from satellite altimeters are only available along one-dimensional lines traced by the nadir ground track, two-dimensional images of tsunami-induced changes in ocean surface roughness could be obtained by using microwave radiometers and radars already on orbit. As outlined in chapter 3, Godin et al. (2009) present a model for calculating the tsunami-induced changes in ocean surface roughness, providing a factor directly related to SSH that corresponds to the modulation of background wind speed resulting from the passage of a tsunami. The ability to detect the tsunami from such a two-dimensional image is largely dependent on the variability and strength of the background wind field at the time of the tsunami passage. With a constant background wind of physically realistic

magnitude, the tsunami-induced changes in ocean surface roughness are apparent (Fig. 5.1A). Values shown are computed from equations 1 and 2, assuming a constant background wind of 3 m/s and a SSH profile derived from the Jason-1 measurements for the 2004 Sumatra-Andaman tsunami (the two-dimensional SSH values were not measured directly by Jason-1, but are representative of the magnitudes during the Sumatra-Andaman tsunami). When using the QuikSCAT wind speeds from December 26, 2004 (the day of the Sumatra-Andaman tsunami), however, the tsunami-induced σ_0 changes are obscured by the variability of the background wind field (Fig. 5.1B). As in the one-dimensional case, it will likely be necessary to find an appropriate method for filtering the data to allow separation of the tsunami-induced signal from the background wind variability and measurement noise.

To date, searches of two-dimensional images of ocean surface roughness measurements from instruments already on orbit have not yielded any positive identification of a tsunami-induced signal, partially due to poor sampling coincident with the events. Nevertheless, it is possible that sufficient satellite sampling of the tsunami wave front and other physical characteristics of the tsunami could be utilized in the detection of a tsunami using changes in ocean surface roughness. Multiple two-dimensional images of the same region obtained with relatively short time separation could allow for the use of the rapid propagation speed and large spatial extent of the tsunami in the open ocean to aid in the early detection of the tsunami signal.

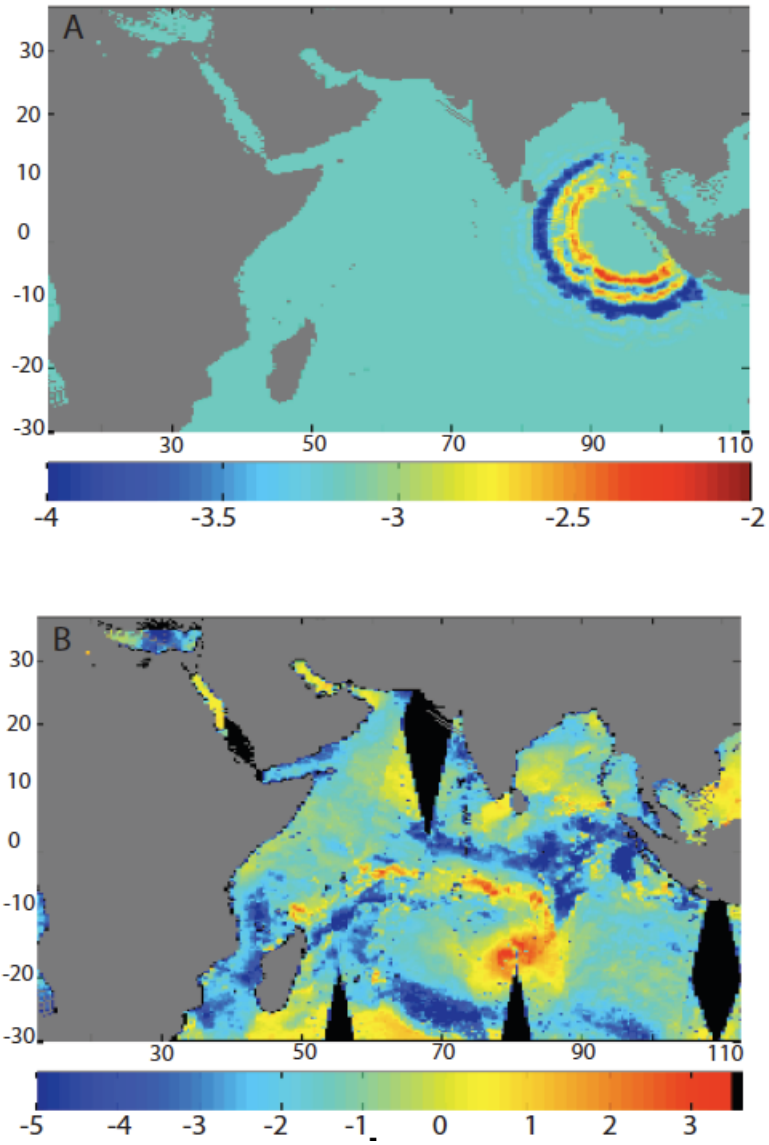

Figure 5.1. Using the model presented in Godin et al. (2009) and equations 1 & 2, the two-dimensional field of radar backscattering strength (dB) is computed for A) a constant background wind of 3 m/s, and B) a background wind field obtained from QUIKSCAT on December 26, 2004. SSH data used for computing the values has been derived from the Jason-1 measurements of the 2004 Sumatra-Andaman tsunami.

5.2 Summary and Conclusions

Satellite altimeters provide the chance to study the effects of a tsunami wave in the open ocean through concurrent measurements of the sea surface height and the radar backscattering strength. Availability of the SSH data allows one to compare statistical properties of the radar backscattering strength when there is and there is not a tsunami wave present, without having to use tsunami source and propagation models. Using satellite altimeter observations, we have demonstrated that tsunamis in the open ocean cause distinct, measurable changes in ocean surface roughness. We have shown this to be true definitively for the 2004 Sumatra-Andaman tsunami and tentatively true for the 2010 Chile tsunami, 1992 Nicaragua tsunami, and 1995 Chile tsunami.

Although the feasibility of tsunami detection from changes in ocean surface roughness has been demonstrated using measurements from satellite altimeters, the practical issue of optimal retrieval of a tsunami signal from other sources of ocean roughness measurements remains an open question. Use of radar backscattering measurements from satellite altimeters would be impractical for tsunami detection and early warning purposes because of the limited number of operational satellite altimeters. Even if the data could be processed quickly enough to be useful, the temporal resolution and spatial coverage of nadir pointing altimeter measurements is not adequate for tsunami detection and warning. The tsunami-induced surface roughness variations, however, are likely to be observable with other types of space and airborne sensors. Unlike the sea surface height, which is measured at nadir points along the satellite ground track, variations in ocean surface roughness can potentially be measured over wider swaths with side-looking radars and scanning microwave radiometers. The broader surface coverage of these sensors suggests that they are more promising for early tsunami detection and may be an

important component in a future global system for tsunami detection and warning. Further research is required to demonstrate tsunami detection with such instruments and, as seen in Fig. 5.1, appropriate analysis techniques will have to be developed to extract the tsunami signal from such data. We anticipate that this study will stimulate the development of data processing algorithms and microwave sensors for the identification of tsunami-induced ocean surface roughness changes to complement or enhance existing regional tsunami detection and early warning systems and contribute to a future global system.

5.3 Future Work

While it has been shown that space-borne instruments can detect tsunami-induced variations in sea surface roughness, more work is required before such techniques can be used as the foundation of an effective system for the early detection and warning of a tsunami in the open ocean. To date, it has been difficult to find satellite observations of tsunamis in the open ocean outside of those provided by satellite altimeters. With the limitations of the satellite altimeters in terms of spatial and temporal sampling, being able to find the tsunami signal in other instruments is a necessary requirement.

Future work on this problem has two main components. The first is determining which instruments can potentially identify the tsunami signal in the open ocean at relatively short notice. The second - and more time-consuming - component involves creating a system capable of analyzing the data from these instruments in real-time once a tsunamigenic has occurred, and assessing the tsunami threat by performing statistical randomization tests as described in the previous chapter. While the work presented here demonstrates that such variations in sea surface

roughness are detectable, a great deal of work is still required to create a practical and effective system for the early detection of tsunamis.

PART II: ESTIMATION OF REGIONAL SEA LEVEL TRENDS

CHAPTER 6: BACKGROUND

Sea level is a measurement of considerable interest for the study of climate because it reflects the mass and heat storage changes in the global ocean. Understanding and predicting future sea level change in response to climate change is one of the most important challenges facing climate scientists, as changes in sea level will likely have significant societal, economic, environmental, and scientific consequences. Millions of people live along the coasts of continents, drawn not only out of necessity, but also by economical and recreational opportunities. Coastal development has accelerated in recent years, but it has taken place with little consideration to rising sea levels. Despite the potentially devastating consequences across all aspects of life, estimates of the timescales, magnitudes, and rates of future sea level rise vary considerably, largely as a result of the lack of detailed understanding of processes in the ocean that may contribute to or be affected by variations in sea level. Over the past few decades, researchers have used various methods to provide a snapshot of the current condition of the ocean and sea level in an attempt to improve our understanding of changing sea level. A critical question, however, is how the current state of the ocean compares to previous ocean states and how we can use this information to predict and project sea level change in the future. Our ability to understand present and future sea level change is largely determined by our understanding of how sea level has fluctuated in the past over a range of different timescales, and the relationship of this sea level change to changes in climate. Therefore, in recent years, an emphasis has been placed on quantifying sea level variations in the past, present and future (Cazenave and Nerem, 2004; Houghton et al., 1996; 2001; Miller and Douglas, 2007; Warrick et al.,1993).

Tide gauges have been the primary source of sea level measurements over the last two centuries. While providing relatively long records, the spatial resolution of tide gauges is poor, thus making accurate estimates of global mean sea level (GMSL) difficult (Douglas, 1991; Groger and Plag, 1993; Nerem, 1995) and studies of regional sea level unfeasible. The vast majority of tide gauges are located around the heavily populated areas of North America, western Europe and Japan, with comparatively few tide gauges located in the southern hemisphere. In addition to poor spatial distribution, tide gauges may move vertically because of processes such as postglacial rebound and tectonic uplift (Mitrovica and Davis, 1995; Peltier and Tushingham, 1989). Long-term averaging is required to overcome these limitations (Douglas, 1991), but estimates of GMSL derived from tide gauges are as varied as the techniques applied to produce these estimates.

In the past couple of decades, satellite altimetry has also provided estimates of patterns and trends in sea level change. The near-global coverage and accurate measurements of satellite altimeters have led to the first definitive estimates of GMSL (Beckley et al., 2007; Leuliette et al., 2004). In principle, satellite altimeters should provide better estimates of changes in global sea level due in large part to the near-global coverage of the measurements. Despite this improved spatial sampling, the satellite altimetry data record spans only 17 years, leading to difficulties in separating the secular trend from low-frequency sea level variability and providing no information about the state of the ocean prior to 1993. Ideally one would want the record length of tide gauges and the spatial resolution of satellite altimetry to obtain the best possible understanding of changing sea level.

Even with long records of spatially dense measurements, our understanding of changing sea level is limited by the ability to extract physically meaningful signals and information from

the data. Sea level records contain time-dependent signals from a wide array of geophysical processes including tides, post-glacial rebound, and natural ocean variability. The problem of detecting a signal related to or masking underlying climate change in the sea level record is of obvious importance in any attempt to understand global climate changes. A variety of statistical methods and tools have been developed and applied to climatological records to try to gain insight into the changing climate. In this thesis, the focus is on one particular tool, cyclostationary empirical orthogonal function (CSEOF) analysis. In chapter 7, CSEOFs will be introduced and compared and contrasted to traditional EOF analysis. Chapter 8 will demonstrate how CSEOFs can be used to improve estimates of the regional distribution of sea level rise. Finally, chapter 9 will discuss the topic of sea level reconstructions, and in particular how CSEOFs can be used to improve upon current sea level reconstructions.

CHAPTER 7: CYCLOSTATIONARY EMPIRICAL ORTHOGONAL FUNCTIONS

7.1 Motivation for CSEOFs

In empirical orthogonal function analysis, data is decomposed into the sum of a set of individual modes composed of a single spatial pattern and a corresponding amplitude time series, which we will refer to as the loading vectors (LVs) and principal component (PC) time series, respectively, following the naming conventions of Kim et al. (1996). By definition, the spatial patterns represented by the EOF LVs are time independent (stationary) and only the amplitudes vary in time as described by the PC time series. These empirical basis functions are often used to provide useful insight into physical processes in the data. The underlying assumption in EOF analysis, however, is the stationarity of the analyzed data; that is, the covariance function does not vary in time. This stationarity assumption is rarely justifiable for geophysical and climate variables even after removing cyclic components like the annual and semi-annual cycles. Subsequently, physical inferences based on EOFs can be misleading and potentially erroneous.

The spatial patterns of many known phenomena in climate science and geophysics show the presence of seemingly random fluctuations in addition to a deterministic component such as the annual cycle. Such signals change in time with well-defined periods (deterministic component) in addition to fluctuating at longer timescales, and thus exhibits a time-dependent covariance function. Such signals are said to be periodically correlated or cyclostationary. Typical responses of a physical system are not stationary but evolve and change over time, and a suitable representation of this time-dependent response is important in order to accurately extracting physically meaningful modes and their space-time evolutions from the data. This also has implications for finding the physically consistent evolution of a signal and identifying teleconnections.

7.2 EOFs vs. CSEOFs

The decomposition of data in terms of a set of basis functions is often very useful in understanding the complicated response of a physical system. By decomposing into less complicated patterns, it may be easier to understand and shed insight on the nature of the variability in a dataset. While theoretical basis functions have been studied extensively, exact theoretical basis functions are very difficult to find and in general, computational basis functions are sought instead. Perhaps the simplest and most common computational basis functions are empirical orthogonal functions. Consider a simple system defined by:

$$T(x,t) = \sum_i LV_i(x)PC_i(t) \qquad (7.1)$$

where LV(x) is a physical process (termed to be the loading vector, as above) modulated by a stochastic time series PC(t), which is called the principal component time series. Each loading vector and principal component time series pair represents a single EOF mode. As mentioned above, however, physical processes and the corresponding statistics are time-dependent, and representing the data with stationary loading vectors can lead to erroneous interpretation of the data.

One example of a cyclostationary signal in the ocean is the annual cycle. The annual cycle signal in sea level not only oscillates with one-year periodicity, it also changes amplitude over time, giving rise to a modulated annual cycle (MAC), and other ocean variability associated with the annual cycle cannot be captured by a single spatial pattern. Similarly, the signal associated with the El Niño-Southern Oscillation (ENSO), which is phase-locked to the annual cycle, consists of a quasi-biennial component and a lower frequency component (Goswami 1995; Philander 1990; Rasmusson et al. 1990; Rasmusson and Wallace 1993). The biennial component

represents phases of El Niño and La Nina and, like the annual cycle, its amplitude varies over longer timescales.

Kim et al. (1996; 1997; 1999; 2001) introduced the concept of cyclostationary empirical orthogonal function (CSEOF) analysis to capture the time-varying spatial patterns and longer-timescale fluctuations present in geophysical signals. The significant difference between CSEOF and EOF analysis is the LVs' time dependence, which allows the spatial pattern of each CSEOF mode to vary in time, with the temporal evolution of the spatial pattern of the CSEOF LVs constrained to be periodic with a selected "nested period". In other words, the system is defined as:

$$T(x,t) = \sum_i LV_i(x,t)PC_i(t) \qquad (7.2)$$
$$LV(x,t) = LV(x,t+d)$$

where the loading vectors are now time dependent, and are periodic with the nested period, *d*. Each CSEOF mode, therefore, is composed of twelve LVs and one PC time series when using, for example, monthly data and a one-year nested period. This allows the evolution of the annual cycle to be captured in a single mode. In an EOF decomposition, the evolution of the seasonal signal is typically split into several orthogonal computational modes (Kim and Chung 2001), which is one reason the signal is usually removed from the data record by some other means. Recent studies, however, have demonstrated the efficacy of CSEOFs to extract robust modes representing the MAC and ENSO variability (Trenberth et al. 2004; Hamlington et al. 2011). This leads to the possibility of removing the MAC or ENSO variability from the data without affecting signals associated with other ocean variability. Stationarity, and hence empirical orthogonal functions, is a special case of CSEOFs, in which the nested period is equal to one.

Furthermore, as the period of a signal becomes much larger than the selected nested period, the loading vectors for that mode will approach a single time-independent pattern.

7.3 Nested Periodicity

While the assumption of periodic statistics is reasonable for many geophysical variables, it can be difficult to prove this periodicity and subsequently choose the nested period for the CSEOF decomposition. The nested period must be determined based on *a priori* physical understanding of the physical process to be investigated. In many cases, there exists an obvious choice for the nested period. For instance, if one is studying the annual cycle signal which is prominent in the sea level data, the nested period would obviously be one year. Sometimes, however, the period of the physical process of interest is not as obvious. For example the widely-known ENSO signal does not have a well-defined period, but instead falls somewhere in the range between (approximately) two and five years. Furthermore, what should the nested period be if one is studying several different geophysical signals, with a range of periods? It is a simple matter to show that the nested period should be selected as the least common multiple of the periods of signals of interest. For instance, if there is a dataset in which semi-annual, annual and biennial periodic signals are all present, the nested period should be set at two years. The semi-annual cycle LVs would simply repeat four times, while the annual cycle LVs would repeat twice.

7.4 Previous Applications of CSEOFs

The concept of CSEOF analysis was first developed by Dr. Kwang-Yul Kim (1995; 1996) as a way to describe climatic time series with well-defined periods but unpredictable

amplitude fluctuations. The first published application involved performing a CSEOF decomposition of the globally averaged surface air temperature field (Kim et al. 1996). The use of CSEOFs was extended to detecting a variety in signals including ENSO, greenhouse warming, and sunspot fluctuations (Kim et al. 1998). More recently, CSEOFs were used to extract the annual cycle from the tropical Pacific sea surface temperature field (Kim and Chung 2000). This analysis was able to accurately explain the detailed structure and temporal modulation of the annual cycle. Similar work was completed on the satellite altimetry sea level record, demonstrating the ability to use CSEOFs to extract not only the modulated annual cycle, but also the ENSO signal that is present in the sea level data (Hamlington et al, 2011).

Given the recent development of CSEOFs, the applications to this date are still somewhat limited. The advantages of CSEOF analysis over more traditional EOF analysis suggest that CSEOFs should see expanded use in the future, particularly as more researchers become familiar with the concept.

CHAPTER 8: EFFECT OF SIGNAL-TO-NOISE RATIO ON THE STUDY OF SEA LEVEL TRENDS

8.1 Introduction

One of the main challenges in estimating secular trends in sea level is overcoming the low frequency variability present in measurements of sea level. Sea level records contain time-dependent signals from a wide array of geophysical processes including tides, post-glacial rebound, and natural ocean variability that can obscure secular trends in the data. Furthermore, signals that are in reality periodic may appear secular and contribute to the secular trend estimate in a shorter time series, such as that provided by satellite altimetry. While the only way to fully overcome this issue is to wait until a longer time series is available, it is important to consider the implications that such low-frequency signals will have on estimates of the secular trend. By secular trend, we refer to the monotonic, non-periodic portion of the signal. This definition allows for the possibility of acceleration in addition to the linear rate of sea level change. For the purposes of this study, however, we will focus strictly on the linear portion of this secular trend. While methods exist for removing a secular trend from a short and noisy time series (Wu et al., 2007), estimations of sea level trends in literature are typically given as linear trend estimates. For this reason, the discussion here is limited to this commonly accepted understanding of "sea level trend" as opposed to the definition of the "secular trend" given above, and henceforth, any discussion of the sea level trend will refer only to the linear contribution of this trend. The ability to extract the sea level trend from the background variability of the ocean is limited by how well one can correct for the time-varying and periodic signals in the record (Sturges, 1990; 2001). Some of these signals, the annual and semi-annual cycles for example, have a relatively short and well-defined period and several techniques are widely accepted for removing them from the

data. Other sea level variations are more irregular, such as those associated with El Nino-Southern Oscillation (ENSO), making filtering of these signals prior to estimating the trend in sea level more difficult. Recent studies have shown that ENSO variability can have a substantial effect on estimations of low-frequency variability and trends (Compo and Sardeshmukh, 2010). The problem of estimating and removing ENSO-related variations from climate records has been addressed in several past studies implementing a variety of techniques, all of which have difficulties in completely capturing the ENSO signal (Penland and Matrosova, 2006). In short, if the temporal span of the data is not long enough to resolve a longer period signal, there is no way to distinguish this signal from the trend in the data.

Typically a least squares approach has been used to remove the annual and semi-annual signals and estimate the trend in the filtered signal (Beckley et al., 2007; Leuliette et al., 2004; Nerem et al., 1999). This approach assumes the annual cycle to be a pure harmonic that does not vary from year to year, which may be physically justified given the cyclical variations of solar radiation incident at the top of the atmosphere that occur repeatedly year after year at every location on earth. However, incident solar radiation is not purely periodic and is seen to exhibit longer period fluctuations (Meehl et al., 2009; Wu et al., 2008). Additionally, the periodic forcing is not of as much interest as the effect it has on variables like sea surface height and temperature. Earth's climate is a nonlinear system, and these nonlinearities prevent the response resulting from a periodic forcing to be similarly periodic. From a more simplistic perspective, it is not uncommon to experience an unusually cool summer followed by a warmer than normal winter and another cool summer, which would comprise a weaker than normal annual cycle. This idea of a modulated annual cycle has been recognized in other climate studies (Gu et al., 1997; Kim and Chung 2001; Pezulli et al., 2005; Wu et al., 2008).

By using a least squares approach to remove the annual cycle and estimate the trend, the low frequency modulation of the modulated annual cycle is not removed from the data and may contribute to the estimated trend. Another commonly used method of removing high-frequency variability and the annual cycle, low-pass filtering, will have similar difficulties. Furthermore, such methods do little or nothing to account for variability arising from non-secular signals such as the sea level variability associated with ENSO. Previous studies have used bandpass filtering between approximately 2 and 6 years to identify ENSO-related variations, but this assumes that all of the variability in the chosen band and none outside of it is associated with ENSO (Folland et al., 1999; Lau and Weng, 1999; Parker et al., 2007; Zhang et al. 1997). Linear regression of well-known ENSO indices has also been implemented to extract the ENSO-related variability, but this assumes that ENSO-related variations occur in phase at all points around the globe (Cane et al., 1997; Chiang and Vimont, 2004; Kelly and Jones, 1996; Robock and Mao, 1995l Vyushin and Kushner, 2009). In spite of the inability of commonly practiced techniques to remove variability unrelated to the linear trend, there has been little discussion of the signal-to-noise ratio (SNR) between the linear trend and the "background noise" obtained from such approaches. Any variability from signals that are unaccounted for and remain in the analyzed signal will serve to decrease the SNR and potentially hinder the ability to accurately estimate sea level trends. The term "background noise" is used to describe the variability present at relatively low frequencies that cannot be estimated and understood physically and is on the same order as the trend in sea level (Sturges, 1990). Hughes and Williams (2010) investigated the statistical error caused by this background noise in estimated regional sea level trends and found that most areas of the ocean will require a fairly extensive record length to estimate trends with error even at the 1 mm/yr level. The analysis of sea level, however, can be greatly improved if as much of the

background noise as possible is explained and treated as known signal rather than noise that confuses the estimation of the trend. By using a method to account for more of the underlying signal including the low-frequency fluctuation of the annual cycle, the SNR, in addition to the error on trend estimates, can be improved. Furthermore, by looking at the global variation of SNR, areas can be identified in which the sea level trend is significant relative to the background noise. Conversely, areas can be mapped in which the background noise still dominates the trend and it can thus be inferred where a longer time series is needed to achieve a reasonable SNR that would make regional studies of sea level change feasible.

An attempt has been made to improve the SNR between the trend and background noise in the altimetric sea level record by identifying signals that are not associated with the trend in sea level and subsequently removing those signals from the sea level record. The SNR associated with commonly used least squares methods can be improved, and additional insight into the trends in sea level may be obtained using a more sophisticated statistical method, specifically cyclostationary empirical orthogonal functions. In section two of this chapter, the way in which the CSEOF analysis was applied to estimate and improve the SNR between the trend and background variability is described. Section three provides an overview of the results obtained using CSEOF analysis including the spatial variation of the SNR and standard error obtained using both the CSEOF method and the traditional least squares method. Finally, section four outlines the importance of understanding and improving the SNR and some of the implications that this could have on the estimates of the trend, both in terms of regional and global mean sea level change.

8.2 CSEOF Analysis of the Satellite Altimetry Data

The quarter-degree resolution AVISO multiple altimeter gridded global dataset composed of sea level measurements spanning 1993-2008 is used for this study. The altimeter products were produced by Ssalto/Duacs and distributed by AVISO, with support from CNES (http://www.aviso.oceanobs.com/duacs/). Using CSEOF analysis, it is possible to extract the time-variant, or modulated, annual cycle in the sea level data. First, the time series at each grid point is individually detrended - and thus centered - by removing the linear trend computed by least squares. Since the CSEOFs are used to separate signals from the linear trend, the linear trend should not be represented in our CSEOF decomposition. In order to distinguish the variability associated with the annual cycle, a nested period of 12 months is used in the CSEOF analysis. The annual cycle is described by the first CSEOF mode as it is the dominant signal in the detrended data. The top panels in Fig. 8.1 show the time-dependent loading vectors associated with the annual cycle, while the bottom panel shows the PC time series of the CSEOF mode. The PC time series does not exhibit the annual cycle period of 12 months, which is instead described by the LVs that are required to have a period of one year. The PC time series describes the longer timescale fluctuations of the annual cycle. The fluctuations of the annual component time series reflects variation of the strength of the annual cycle about some mean amplitude. The amplitude of the annual cycle varies within 20% of the mean, with values that are less than the mean, indicating weaker than normal annual cycles and values greater than the mean, indicating stronger than normal annual cycles. The PC time series shows interannual variability that can be related to ENSO. The El Nino phase of ENSO tends to weaken the annual cycle and a weak negative correlation is observed between the PC time series and an ENSO index, such as the multivariate ENSO index (MEI) (Wolter and Timlin, 1998). The MEI can be understood as a

weighted average of the main ENSO features contained in six different variables and serves as a tool for monitoring ENSO events. In addition to its relationship with ENSO, the CSEOF mode also contains oscillations with the period of six months, which are likely due to the semiannual cycle present in sea level time series. By combining the loading vectors and the principal component time series and then averaging, a global mean sea level (GMSL) time series associated with the annual cycle can be formed (Fig. 8.2). The 12-month periodicity is clear from this figure, as well as the time-varying amplitude of the GMSL annual cycle that is produced by the CSEOF analysis.

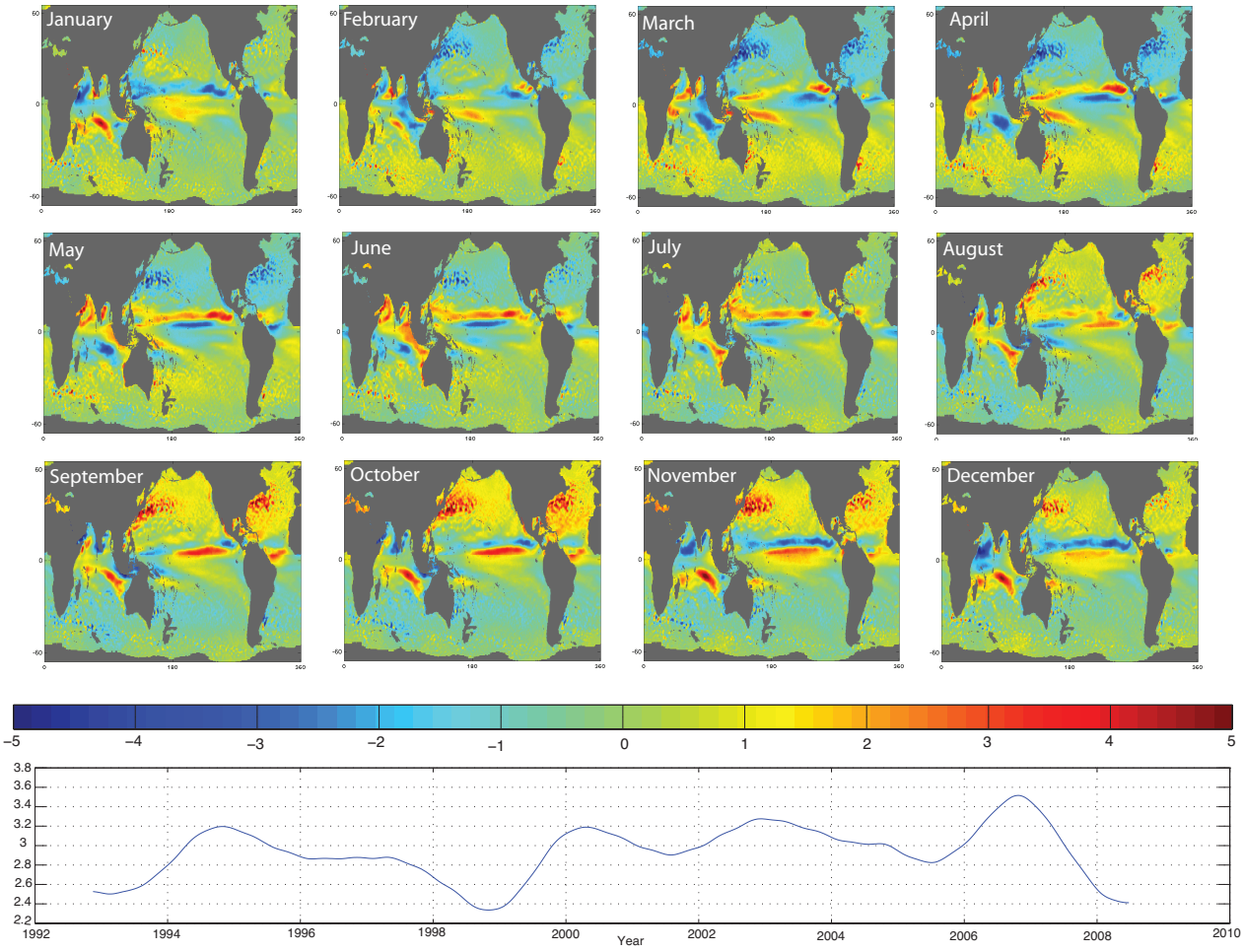

Figure 8.1. Once the AVISO data is centered using least squares, CSEOF analysis is performed on the residual using a nested period of 12 months. The first CSEOF mode explains the annual cycle signal. The top panels show the time-dependent loading vectors while the bottom figure shows the PC time series. The time series displays the time-varying amplitude of the annual cycle.

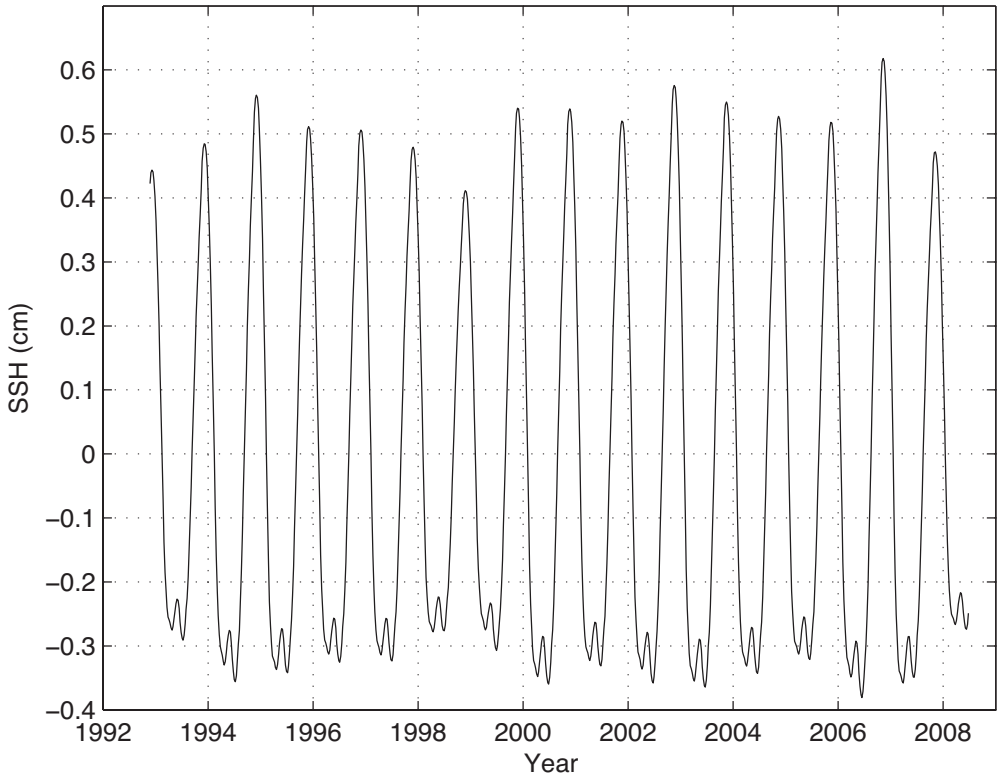

Figure 8.2. The time-dependent loading vectors and the PC time series (Fig. 8.1) are combined and averaged to form a global mean of the annual cycle mode. This time series exhibits the expected 12-month periodicity associated with the annual cycle. The double-trough occurs as a result of the semi-annual cycle.

In addition to the ability to extract a modulated annual cycle, another advantage of the CSEOF technique comes from the potential to extract physically interpretable modes with less, albeit still significant, variability. The second CSEOF mode is shown in Fig. 8.3. The top panels show the temporally varying loading vectors while the bottom panel shows the associated PC time series. After plotting the MEI with the global mode associated with the second CSEOF mode as seen in Fig. 8.4, the significance of this mode becomes clear. With a correlation of 0.80 between the MEI and global mean time series of the CSEOF mode and by looking at the spatial patterns of the loading vectors, it is clear that the second CSEOF represents the ENSO variability

in the dataset. The ability to extract a mode directly related to the ENSO signal represents one of the strengths of the CSEOF method.

As previously mentioned, in studies of sea level trends, commonly the annual and semiannual signals are estimated and removed from the data using least squares, and the linear fit associated with the trend is simultaneously extracted. No attempt is made to identify and remove other signals in the data that are not associated with the sea level trend. Doing so could greatly improve the SNR between the linear trend and the background noise, thus improving the confidence we have in our trend estimates. A primary reason for why other signals are not extracted from the data prior to estimating the trend results from the limitations of the least squares method. Both the least squares method and the CSEOF technique require *a priori* physical understanding of the underlying signals being analyzed. For CSEOF analysis, this *a priori* knowledge is used to set the nested period of the signal that is to be extracted. Other than the nested period, no assumption is made about the signal and no restriction is placed on the modes resulting from the CSEOF technique. For the least squares technique, a set of functions with a known period must be selected. Once solved, the amplitudes of these functions may vary spatially but not temporally. Furthermore, if a signal, such as ENSO, is to be extracted from the data, a function must be defined that can describe the variability associated with ENSO locally at each location around the globe.

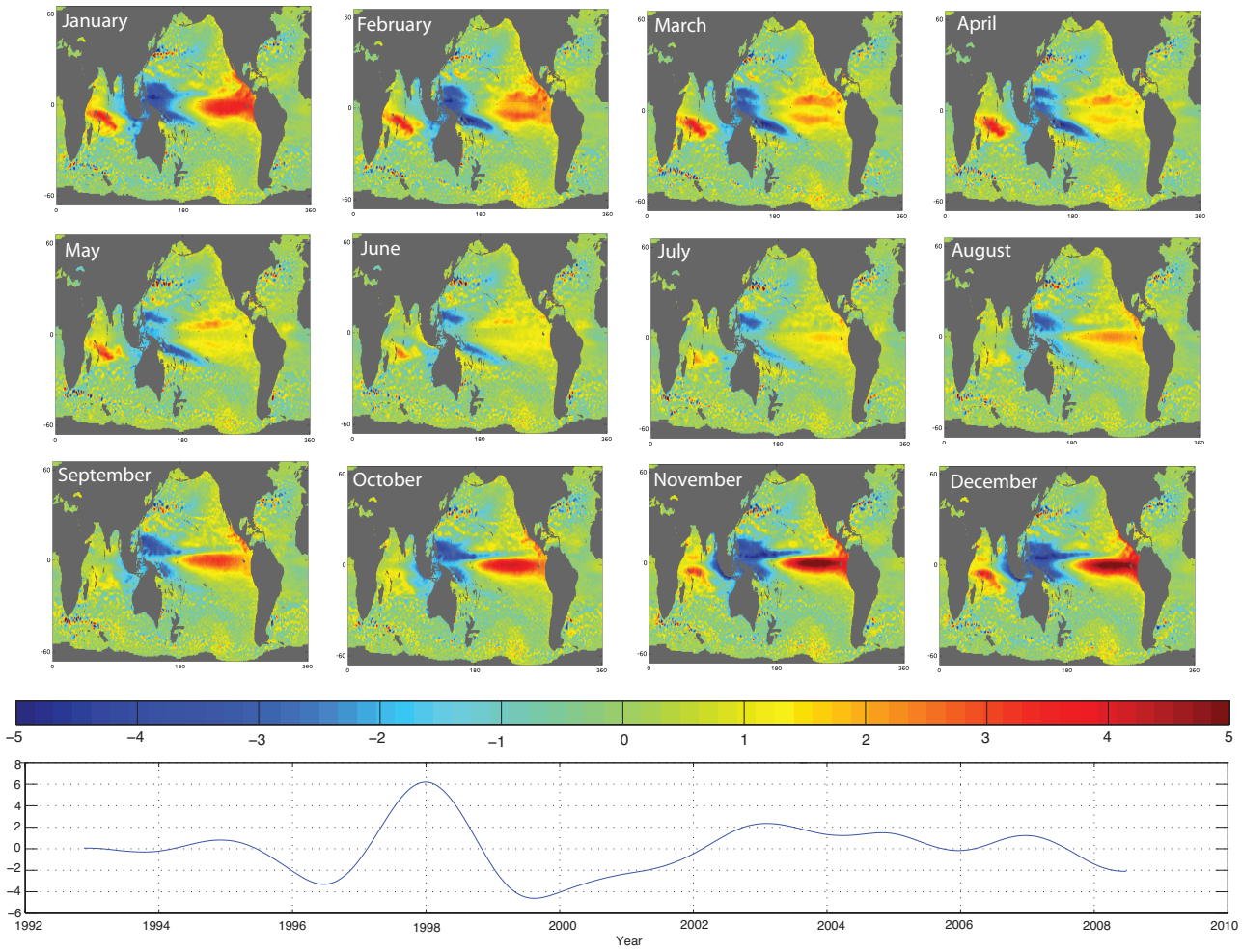

Figure 8.3. The second CSEOF mode is shown with the loading vectors in the top panels and the PC time series shown in the bottom panel. Based on the spatial pattern of the loading vectors and the PC time series, this mode is related to the ENSO signal. The PC time series has a very high correlation with the MEI.

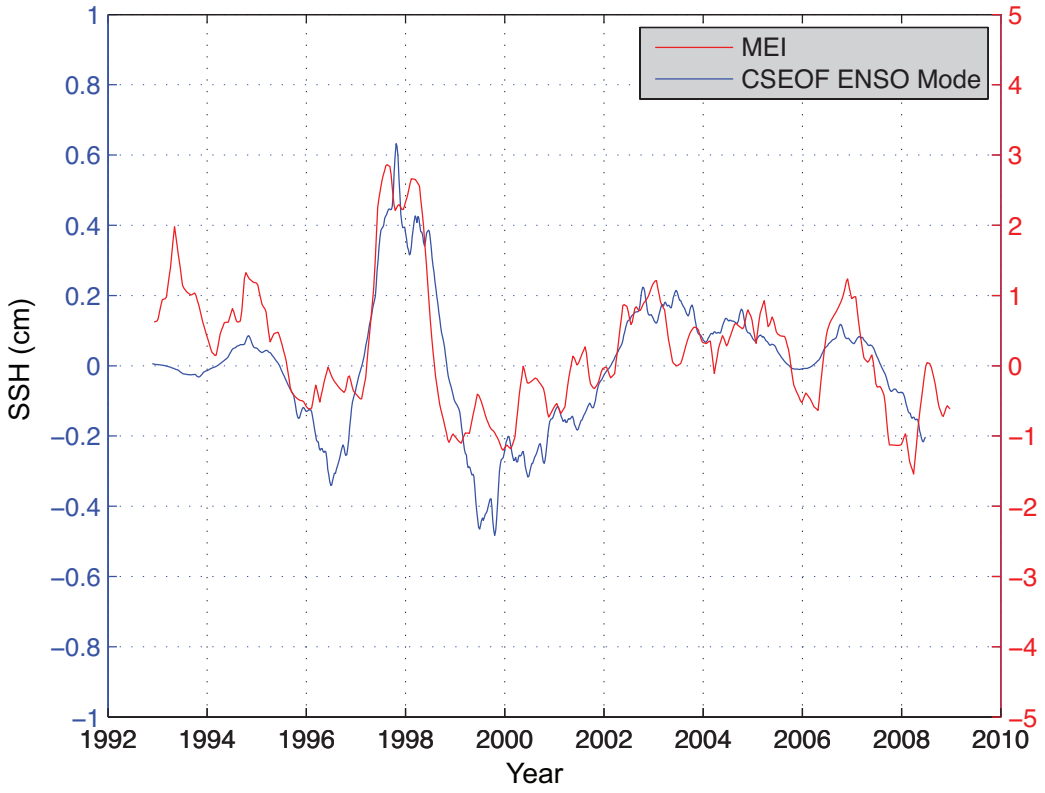

Figure 8.4. The global mean time series of CSEOF mode 2 (blue) and the MEI (red) show a very strong correlation of 0.80. Coupled with the loading vectors, the second CSEOF mode is physically interpretable as being associated with ENSO.

8.3. Results

To demonstrate the differences between the least squares approach and the CSEOF technique, it is instructive to look at the SNR between the linear trend and the underlying background noise for each method. For the CSEOF analysis, a nested period of 12 months is used, and the signals associated with the modulated annual cycle and ENSO (as seen in Figs. 8.1 and 8.3) are estimated and removed from the original data. The linear trend in the remaining data is computed using least squares. This linear trend is then removed from the data, and the residual is smoothed using a six-month running average to remove the higher frequency signals. Finally, the remaining signal is considered to be unexplainable -- at least in the context of the CSEOF analysis -- background noise. The six-month running average is selected to remove any remaining variability associated with the semiannual cycle in addition to higher frequency signal that has little effect on estimating the linear trend. The power associated with both the linear trend and background noise is estimated by integrating the squared time series for each. SNR values are then computed by dividing the linear trend power by the background noise power. For comparison, using least squares, the annual signal, semi-annual signal, and linear trend are simultaneously removed from the data. After the data is similarly smoothed using a six-month running average, the residual is considered to be the background noise. Fig. 8.5 shows the spatial variation of the SNR between the linear trend and the background noise computed from the CSEOF method and from the common least squares method. Areas in which the SNR is greater than one are distinguished from areas with SNR less than one. Roughly 9.9 % of the world's oceans have an SNR greater than one for the CSEOF method, while only 4.0% of the oceans

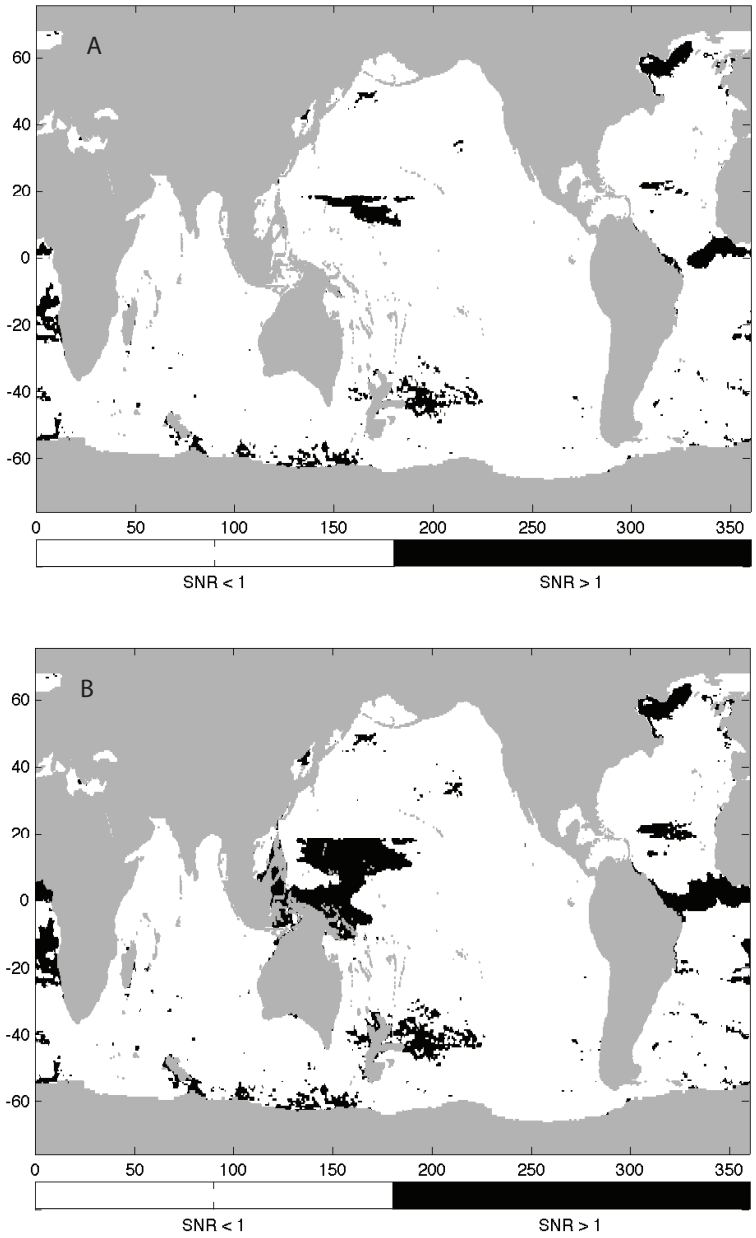

Figure 8.5. Map of SNR between the secular trend and background noise. A) SNR computed solely using least squares, B) SNR from least squares incorporating CSEOF analysis. White represents areas in which SNR is less than 1, while black shows where the SNR is greater than 1.

have an SNR greater than one for the least-squares method. While both of these values are small, it is perhaps more instructive to consider that 89.7% of the oceans have undergone an improvement in SNR when incorporating the CSEOF analysis.

From a standpoint of signal detection, a higher SNR implies a narrower confidence band. Similarly, a reduction in the amount of signal considered to be unexplainable background noise leads to a decrease in the standard error of the least-squares estimate of the linear trend. The standard error (Acton, 1966; Montgomery, 1982) is first computed for the estimate obtained solely using least squares to fit simultaneously the annual, semi-annual, and linear trend to the data (Fig. 8.6a). Next, the standard error is computed for the estimate of the linear trend obtained after removing the modulated annual and ENSO signals resulting from CSEOF analysis (Fig. 8.6b). While the global mean trend does not change significantly, the standard error for the linear trend estimate is reduced in 97.1% of the oceans when the CSEOF analysis is included, with reductions of up to 45% in some locations (Fig. 8.6c).

The CSEOF analysis was performed on varying lengths of the overall time series to better understand the effect of record length on the SNR. Specifically, SNR maps were computed for the first four years, the first eight years, and the first twelve years of measurements in the sea level dataset. Fig. 8.7 shows the spatial variation of the SNR for each with the results for the full time series included for comparison. The percentage of area with SNR greater than one is 10.4%, 10.5% and 6.8% for the four, eight and twelve-year time series lengths, respectively. For the four-year time series, only the first mode was physically interpretable as being associated with the annual cycle. Thus, no other mode was removed from the data before computing the power associated with the

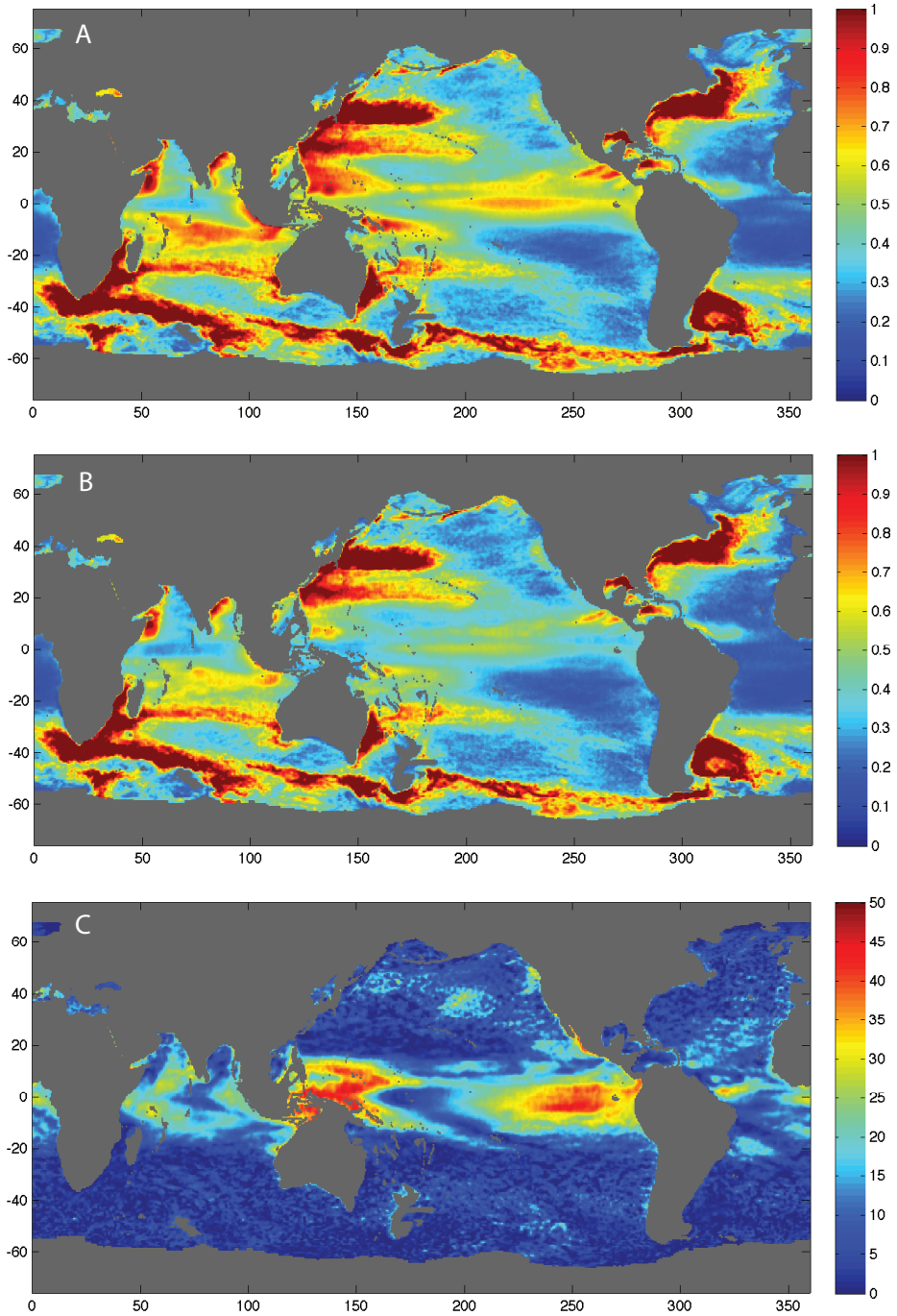

Figure 8.6. Maps of standard error on the estimated linear trend computed from A) a simple least squares approach and B) least squares incorporating CSEOF analysis to estimate and remove the time-varying annual and ENSO signals. Standard error estimates are shown with units of mm/yr. The percentage reduction in standard error obtained from the inclusion of CSEOF analysis is shown in C.

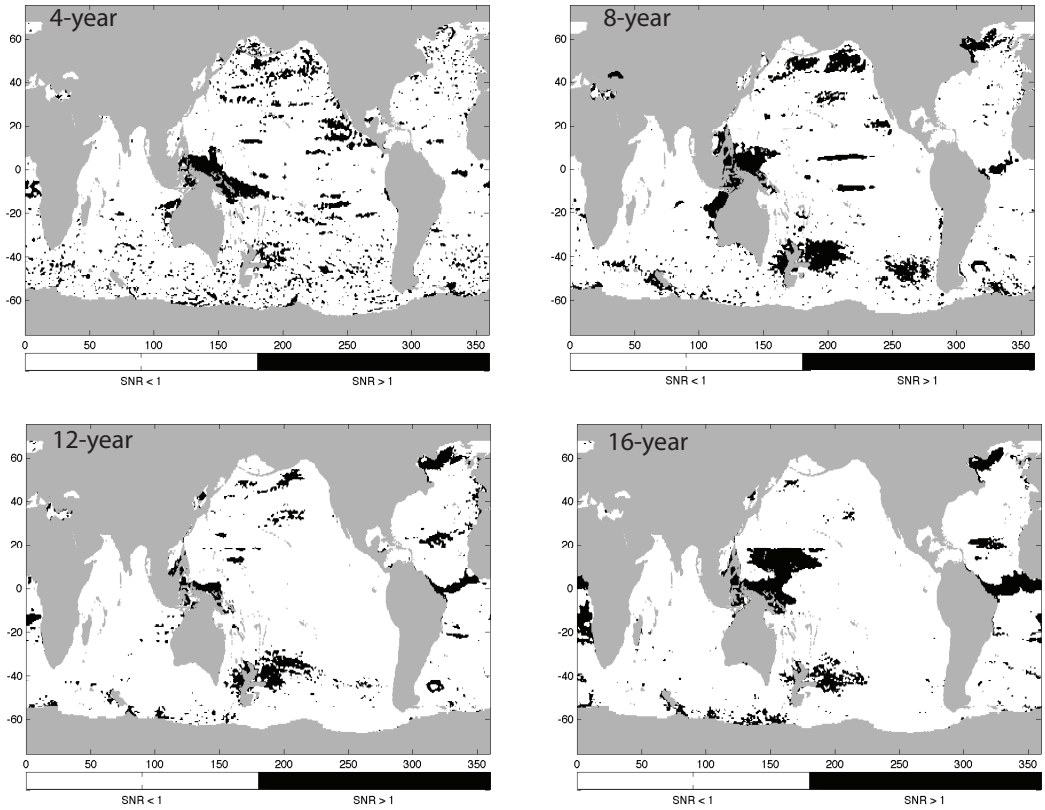

Figure 8.7. Maps of SNR computed using varying lengths of original time series. Top left panel shows SNR for first four years of data, top right shows SNR for first eight years of data, bottom left shows data for first 12 years of data, and bottom right shows SNR for full time series. Percentages of areas with SNR greater than one are 10.4%, 10.5%, 6.8% and 9.9%, respectively.

background noise. The first two modes of the eight-year time series appeared to be a mixture of annual and ENSO signals, and both were removed from the data prior to the calculation of the trend and noise power. Similarly, the standard error on the linear trend can also be estimated for each time span. Fig. 8.8 shows the spatial variation of the standard error for the four-year, eight-year, twelve-year, and 16-year time series. As

expected, the standard error is dramatically reduced when the annual and ENSO signals can be identified and extracted using CSEOF analysis, as was the case for the twelve-year and full time series.

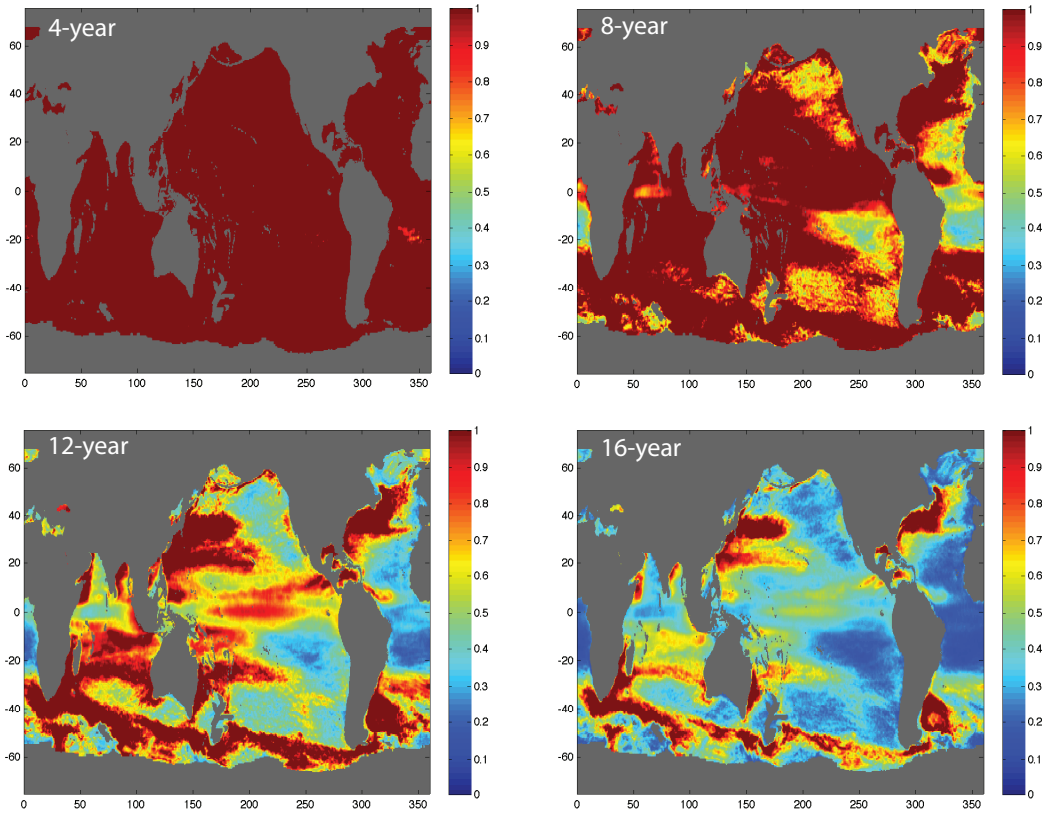

Figure 8.8. Maps of standard error on the estimated linear trend computed using varying lengths of original time series. Standard error is shown with units of mm/yr.

Since the launch of TOPEX/Poseidon in 1992, several studies have been completed on the change in global mean sea level. While global averaging reduces many of the signal-to-noise issues present in point-to-point analysis of sea level change, using different lengths of time series as above allows us to understand the relative confidence with which each GMSL trend was estimated in past studies. We can also estimate how the error on the sea level trend would have

improved if an ENSO mode had been available for a shorter time series. Table 8.1 shows the results for the GMSL trend, SNR, and the ratio of GMSL trend to standard error computed using a variety of different methods for different time series length. The ENSO CSEOF mode from the full 16-year time series was used in the computation for each different length of time series, These results show the extent to which the SNR and ratio of trend to error would be improved if a fully resolved ENSO CSEOF mode had been available after four years and eight years of measurements. The GMSL trend is also noticeably affected when removing the ENSO CSEOF mode, particularly for the 4- and 8-year time series lengths.

In addition to looking at the SNR for the present time period, we project future values of SNR, assuming that the linear component of the secular trend and the noise level do not change over time. SNR maps for 2015 and 2020 estimated in this manner are shown in Fig. 8.9. While it is highly unlikely that these signals are exactly stationary, such an assumption highlights the idea of using SNR to examine the ability to detect secular trends in the near future. The area of SNR greater than one is found to increase to 22.4% in 2015 and to 32.7% in 2020. A similar study was done by Hughes and Williams (2010), in which they determined the amount of time needed to for the error on the trend to drop below 1 mm/yr, a typical accuracy requirement for distinguishing causes of regional patterns of sea level trends. As with the results computed in Fig. 8.9, this requires an extrapolation of the trend and noise into the future. They showed that by adding white noise to extrapolated trends rather than more realistic red noise, the statistical error on the estimated trends can be seriously underestimated, by as much as a factor of ten in some regions. Keeping this in mind, a figure depicting the length of time series required to achieve standard error less than 1 mm/yr is computed here. The trend estimated over the 17-year altimetry record is again assumed to not change, and the residuals between the trend and actual

SSH measurements are sub-sampled and added to the extrapolated measurements. This serves to whiten the noise on the data, and it can then be assumed that the estimates shown in Fig. 8.10 are optimistic. These results are computed for two separate cases: 1) the annual cycle is removed by a least squares fit (Fig. 8.10A), and 2) the annual and ENSO CSEOF modes are removed (Fig. 8.10B). The pattern in Fig. 8.10A is very similar to that shown in Hughes and Williams (2010), although in general the estimated times are reduced. Fig. B shows that times can be improved by more than five years in the equatorial Pacific by accounting for the modulated annual cycle and ENSO signals.

Table 8.1. Trend (T) (mm/yr), SNR, and the ratio of secular trend to standard error for GMSL using different time series lengths and different methods of computation. First column shows results for least squares computation with no other signals fitted or removed. Second column shows results for least squares computation with an annual fit. Third column shows results for least squares computation with the annual CSEOF removed. Finally, the fourth column shows the results for least squares computation with annual and ENSO CSEOF modes removed. Note, GIA correction has not been applied to the trend estimates.

Time Series Length	**Least Squares**			**Least Squares w/annual fit**			**Least Squares w/ annual CSEOF removed**			**Least Squares w/ annual and ENSO CSEOFs removed**		
	T	**SNR**	**T/SE**	**T**	**SNR**	**T/SE**	**T**	**SNR**	**T/SE**	**T**	**SNR**	**T/SE**
4-Year	1.95	0.360	8.34	1.86	1.22	15.5	1.92	1.68	18.1	2.67	2.73	23.1
8-Year	2.91	1.99	28.2	2.94	5.04	44.8	2.93	5.36	46.2	3.22	10.1	63.3
12-year	3.04	5.55	57.9	3.06	15.0	95.3	3.04	16.1	98.4	3.03	23.6	119
16-year	2.97	9.40	87.6	2.99	25.4	143	2.97	27.7	149	2.96	36.9	173

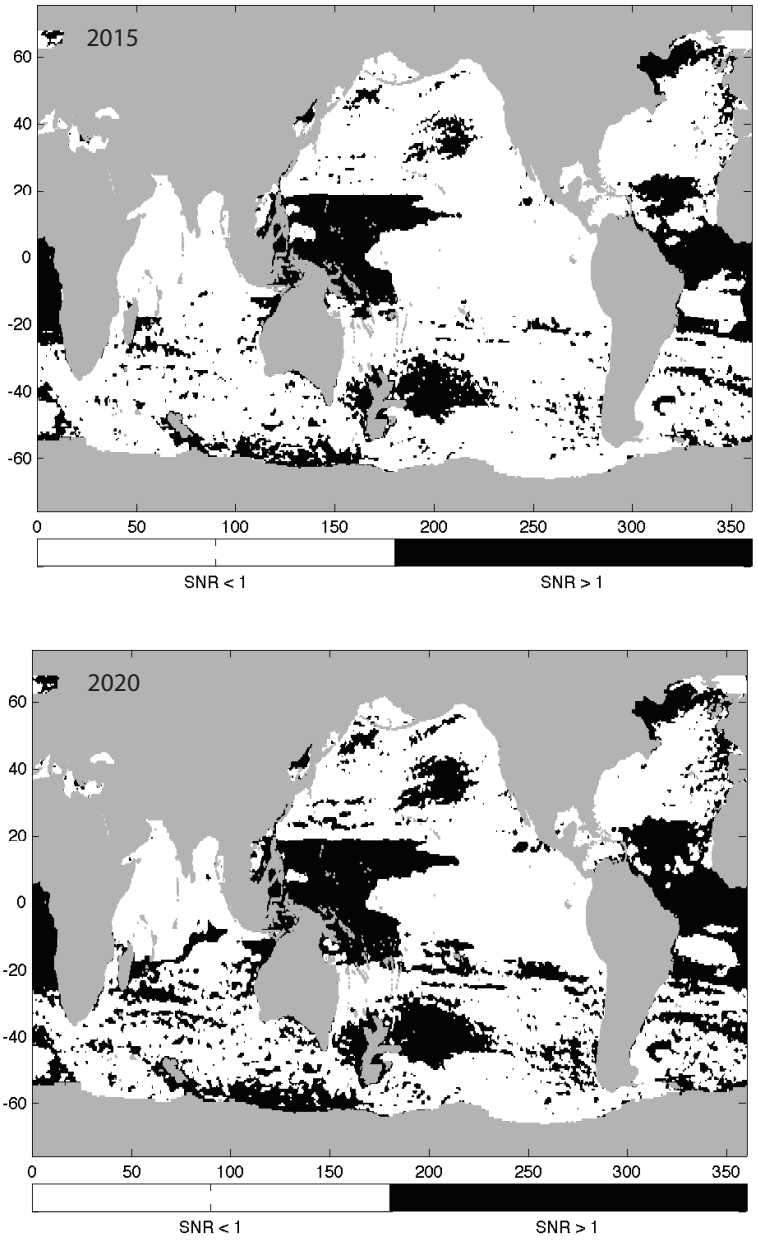

Figure 8.9. SNR maps are created by projecting results to the years 2015 and 2020. The linear portion of the secular trend is assumed to be stationary and the power associated with the background variability of the signal increases linearly with time. In 2015, the percentage of area with SNR greater than one is 22.4%, while in 2020, the percentage of area with SNR greater than one increases to 32.7%.

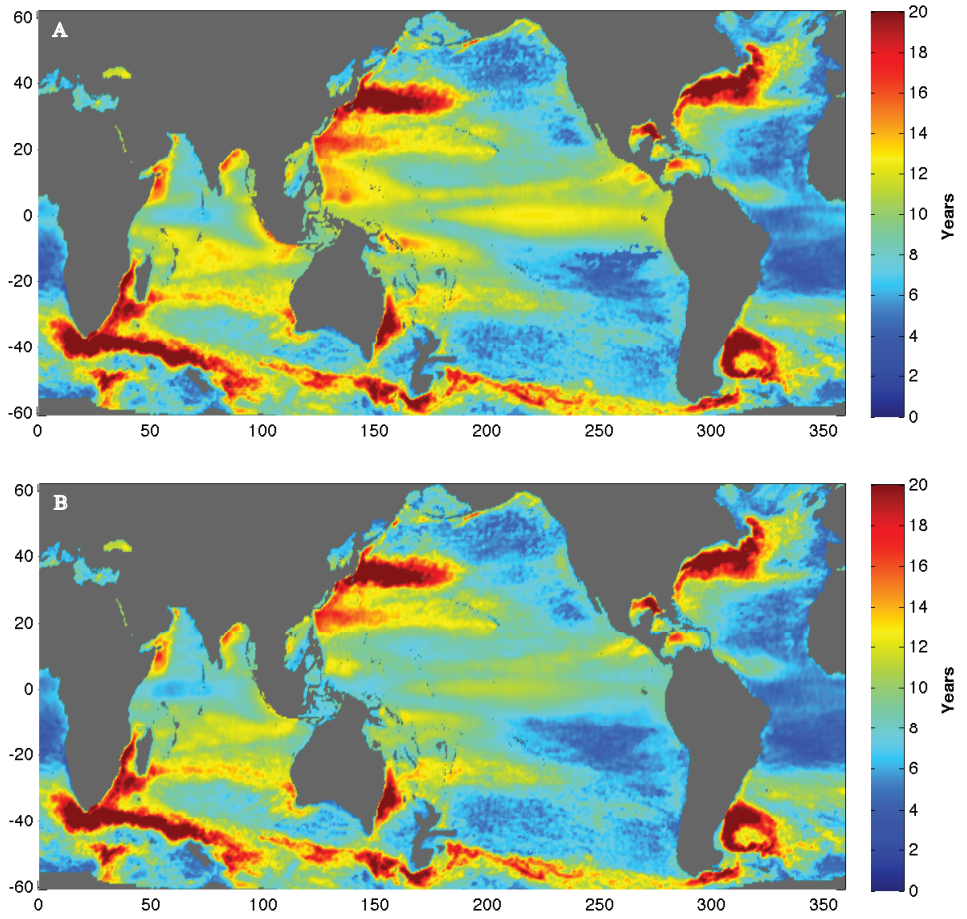

Figure 8.10. The length of sea level time series which would be necessary for the standard error in trend to reduce to 1 mm/yr, based on least squares fit to the time series at each point. A) Annual cycle removed by least squares. B) Annual and ENSO CSEOF modes removed.

8.4 Discussion and Conclusion

The SNR between the secular trend and background noise can be improved by separating the non-secular background variability from the secular trend, which leads to a significant reduction in formal estimates of the standard error on the linear trend computed using least squares. The CSEOF method is uniquely suited to extract this background variability. Specifically, the traditional least squares technique is improved by using CSEOF analysis to

estimate and remove the modulated annual cycle mode and a mode associated with ENSO variability. While the percentage of the globe with an SNR ratio greater than one shows only a modest increase when the CSEOF method is employed, the SNR is improved by some measure over the majority of the oceans. From a standpoint of signal detection, this implies that the secular trend in a greater portion of the globe can be estimated with a higher degree of confidence. A higher SNR naturally suggests a narrower confidence band, and the standard error in the least-squares estimate of the linear trend is reduced across 97.1% of the globe when incorporating CSEOF. While the actual value of the linear trends do not necessarily change dramatically when CSEOF is incorporated, the estimate of the secular trend is improved by lowering the standard error.

By shortening the length of the time series, it is possible to examine how the SNR converges over time and, perhaps more importantly, how the CSEOF method behaves for varying time series lengths. When performing the analysis for the first four years and first eight years of the data, over 10% of the world's oceans have an SNR greater than one. In the case of the four-year time series, only the first CSEOF mode is physically interpretable as the annual signal. There is no single mode showing a strong correlation with ENSO. For the eight-year time series, the first two modes appear to be a mixture of annual and ENSO signals, with neither mode clearly identifiable as one or the other. One may ask why the percentage of area with SNR greater than one for the four-year and eight-year time series is greater than that for the twelve or sixteen-year time series. By considering the standard error for each time series length, the reason for this becomes more apparent. While we can use least squares to estimate the linear portion of the trend, little confidence can be placed in such estimates as a result of the large amount of error. An overestimation of the linear trend, which could occur from such a short time series,

would lead to an apparent increase in the SNR. The four-year time series is not long enough to separate the ENSO signal from the secular trend, and the anomalously strong 1997-98 ENSO event that falls near the end of the eight-year period likely influences the linear trend computed from the eight-year time series. Furthermore, the spatial distribution of the areas with SNR greater than one for the four-year time series contains few large-scale, well-defined patterns. However, from the twelve-year and full time series, we can see that the SNR patterns begin to converge, and an increase of areas with SNR greater than one occurs from twelve years to sixteen years. With twelve years of measurements, the ENSO signal can be resolved in the record, and the first two CSEOF modes are physically interpretable and thus removable from the dataset. The locations with SNR greater than one are also better confined to well-defined areas in the oceans without exhibiting the scatter found from the shorter length time series.

Resolving low frequency signals in the record also has implications for estimates of GMSL trend. In particular, studies have shown that unaccounted for ENSO signal can have a large effect on the estimation of global trends. As mentioned above, the ENSO CSEOF mode could not be fully resolved in the 4- or 8-year records. If such a mode had been available after four years of data had been collected, however, the SNR and standard error of the GMSL trend estimate could have been improved when compared to the more conventional least squares techniques for estimating sea level trends. While the focus of this study is not on the actual estimate of the trend in GMSL in each case, accounting for the ENSO variability has a significant effect on the computed trend value for both the 4-year and 8-year time series. If there exists a low frequency signal that is yet to be resolved in the 16-year time series, the GMSL trend could be markedly different from the estimates that are cited today.

As the length of the data record obtained from satellite altimetry increases, the SNR between the secular trend and background noise should improve. A map of the SNR at a future time can be computed by assuming that the linear component of the secular trend found from the full time series and the power in the background noise are both stationary. The SNR maps are shown for 2015 and 2020 in Fig. 9. In 2015, the area of the ocean with SNR greater than one is over 20%, increasing to more than 30% in 2020. Simply stated, the area with SNR greater than one will still only be less than one-third with twelve more years of measurements, assuming that the trend is stationary and that we are unable to resolve any other signal with a longer time series.

Based on the maps of SNR and standard error, the secular trend is still dominated by unaccounted for signal in the majority of the oceans, even when using sophisticated techniques like CSEOF analysis that are able to extract more of the signal from the background noise. By stating that signal is unaccounted for, it is not suggested that the sources of such signal are entirely unknown. There are a wide variety of physical phenomena that are well understood and contribute to what is defined as background noise in this study. The difficulty, however, lies in being able to extract and separate such signals from the linear trend. It is possible that the CSEOF analysis will extract an additional mode that is physically interpretable in a longer time series. While the ENSO signal was not resolved in the four-year time series, for example, the signal is resolvable using the 12-year record. Similarly, while it may be impossible to resolve a longer period signal in the 16-year time series, it is possible that we can in a 20-year or 25-year time series. Additionally, more sophisticated techniques for removing signal could be implemented to further improve the results presented in this chapter. For any analysis technique, however, there is some minimum length of time series that is necessary to resolve a signal of a

certain oscillation. In the case of the ENSO variability, the CSEOF method was only able to begin resolving the signal in eight years of data, and it was not fully resolved until twelve years of data were utilized. For a signal with decadal oscillations, it may require 20 or 30 years of measurements before it can be accurately resolved. Until we are able to identify and interpret additional signals, it seems unlikely that the SNR between the secular trend and background climate noise will improve significantly in the coming years to the point where the majority of the ocean has an SNR greater than one. Regional sea level trends, therefore, will remain uncertain until we are able to extract the secular trend from the background variability at more locations across the globe.

CHAPTER 9: CSEOF SEA LEVEL RECONSTRUCTION

9.1 Introduction

Chambers et al. (2002) (hereafter Ch02) made one of the first attempts at combining tide gauge data and satellite altimetry data using a technique known as empirical orthogonal function (EOF) reconstruction. Although EOF reconstruction was originally developed for use with sea surface temperature measurements, the method has since been modified for sea level studies, using least squares fitting of satellite altimetry-derived EOFs to the tide gauge data to reconstruct sea level. Building on this work and that of Kaplan et al. (1998; 2000), Church et al. (2004) (hereafter CW) produced the most comprehensive and widely cited sea level reconstruction to date, which spans 1950 through 2001. The CW reconstruction, which was later updated (Church et al. 2006) to extend back to 1870, has the spatial coverage of satellite altimetry and spans most of the tide gauge record. However, only the portion from 1950 through 2001 has been publicly released. While this sea level reconstruction has been cited frequently and used for future sea level projections (Church et al. 2006; Vermeer and Rahmstorf 2009), the fidelity of the reconstructed dataset is subject to debate. To date, no published attempt has been made to improve upon the CW reconstruction, and there has been little discussion regarding deficiencies of the reconstruction.

One primary shortcoming of sea level reconstructions stems from the use of EOFs as basis functions. EOFs decompose a data record into the sum of a set of individual modes composed of a single spatial pattern and a corresponding amplitude time series, which we will refer to as the loading vectors (LVs) and principal component (PC) time series, respectively, following the naming conventions of Kim et al. (1996). By definition, the spatial patterns represented by the EOF LVs are time independent (stationary) and only the amplitudes vary in

time as described by the PC time series. The spatial patterns of many known phenomena in climate science and geophysics, however, change in time with well-defined periods in addition to fluctuating at longer timescales. Typical responses of a physical system are not stationary but evolve and change over time.

The annual cycle signal in sea level not only oscillates with one-year periodicity, it also changes amplitude over time, giving rise to a modulated annual cycle (MAC), and other ocean variability associated with the annual cycle cannot be captured by a single spatial pattern. Similarly, the signal associated with the El Niño-Southern Oscillation (ENSO), which is phase-locked to the annual cycle, consists of a quasi-biennial component and a lower frequency component (Goswami 1995; Philander 1990; Rasmusson et al. 1990; Rasmusson and Wallace 1993). The biennial component represents phases of El Niño and La Nina and, like the annual cycle, its amplitude varies over longer timescales.

Kim et al. (1996; 1997; 1999; 2001) introduced the concept of cyclostationary empirical orthogonal function (CSEOF) analysis to capture the time-varying spatial patterns and longer-timescale fluctuations present in geophysical signals. The significant difference between CSEOF and EOF analysis is the LVs' time dependence, which allows the spatial pattern of each CSEOF mode to vary in time, with the temporal evolution of the spatial pattern of the CSEOF LVs constrained to be periodic with a selected "nested period". Each CSEOF mode, therefore, is composed of twelve LVs and one PC time series when using, for example, monthly data and a one-year nested period. This allows the evolution of the annual cycle to be captured in a single mode. In an EOF decomposition, the evolution of the seasonal signal is typically split into several orthogonal computational modes (Kim and Chung 2001), which is one reason the signal is usually removed from the data record by some other means. Recent studies, however, have

demonstrated the efficacy of CSEOFs to extract robust modes representing the MAC and ENSO variability (Trenberth et al. 2004; Hamlington et al. 2010). This leads to the possibility of removing the MAC or ENSO variability from the data without affecting signals associated with other ocean variability.

By using CSEOFs in place of EOFs, it is possible to create an improved and alternative reconstruction to a reconstruction based solely on EOFs. The motivation for using CSEOFs in place of EOFs is fourfold. EOFs are not an optimal basis for geophysical signals with cyclostationarity (such as the MAC and ENSO). CSEOFs account for the high and low frequency components of the annual cycle and do not necessitate the removal of the annual signal from the satellite altimetry or the tide gauge records before reconstruction. Specific signals, such as those relating to the MAC and ENSO that account for the majority of the variability in the altimetric record, can be reconstructed individually using CSEOFs with little mixing of variability between modes. The reconstruction procedure using CSEOFs provides for a less noisy reconstruction, thereby reducing the sensitivity of the reconstruction to erroneous tide gauge measurements and poor tide gauge sampling.

Other considerations, in addition to the choice of basis functions, must be made when attempting to perform the most accurate sea level reconstruction. The reconstruction procedure amounts to solving a weighted least squares problem. The selection of weights can be shown to have a significant impact on the resulting reconstruction. When estimating GMSL from tide gauges, regional clustering of tide gauges needs to be avoided or accounted for in the weighting scheme. To account for the latitudinal differences in the tide gauge distribution in a similar way to Merrifield et al., (2009) (hereafter M09), a latitudinal-band weighting scheme can be introduced that accounts for the uneven distribution of tide gauges in the northern and southern

hemispheres. Previous sea level reconstructions do not avoid or account for clustering of the tide gauges, and little discussion has been presented on how this has affected the accuracy of the reconstructions.

In this chapter, a modified reconstruction method is introduced for combining satellite altimetry data with *in situ* tide gauge data utilizing CSEOFs as basis function in the place of EOFs. Section two discusses the satellite altimetry data and tide gauge data that is used for the reconstruction. A description of how the reconstruction is performed using CSEOFs is given in section three. Section four shows the results of the CSEOF sea level reconstruction covering the period 1950 through 2009. The CSEOF reconstruction will be compared to other sea level datasets where available. Section five gives an evaluation of the present reconstructions and describes the benefits of the CSEOF reconstruction technique.

9.2. Data

Both the tide gauge data records and the satellite altimetry data record are required to reconstruct sea level. The satellite altimetry data is used to find the patterns of spatial variability that will be used as basis functions in the reconstruction procedure. These basis functions are then fit in a least squares sense to the tide gauge records extending back over the time period of interest. Brief descriptions of both the tide gauge and satellite altimetry datasets are given below.

9.2.1 Tide Gauge Data

The tide gauge dataset used in the reconstruction procedure is the monthly mean sea level records gathered from the data archive at the Permanent Service for Mean Sea Level (PSMSL) (Woodworth and Player, 2003). The tide gauges in Brest in western France (starting in 1807) and

Swinoujscie in Poland (1811) are the two longest records contained in the PSMSL dataset. However, most of the historical records extending back into the 19th century contain large gaps and can be biased by high water readings. Furthermore, only two reliable tide gauges in the southern hemisphere have observations prior to 1900. The poor coverage of the tide gauge records, both spatially and temporally, makes estimating rates of sea level rise on a global scale exceedingly difficult. As a result of the limitations imposed by the sampling, the study presented here will focus on the time period between 1950 to 2010.

Only the Revised Local Reference (RLR) data provided by PSMSL are used, which are measured sea level at each site relative to a constant local datum over the complete record. The RLR tide gauge records are screened for reference datum stability over time relative to benchmarks on the nearby land. No correction, however, is provided by PSMSL for the movement of the benchmarks themselves. At present, none of the metric data offered by PSMSL have been included as they can have substantial unknown datum shifts and their use in time series analysis is generally not recommended. The dataset used from PSMSL was downloaded in December 2010 and contains 1197 tide gauge records extending into 2010.

Even though PSMSL provides an initial screening of the RLR data that they provide, generally additional editing is done to the tide gauges before being used for analysis. How this editing is completed, however, is subject to debate. Holgate (2007) attempted to show that nine carefully selected tide gauges can be used to compute a global mean sea level (GMSL) time series which is reasonably close to GMSL computed from many more tide gauges (Woodworth et al., 2009). Only one of the nine tide gauges is in the southern hemisphere, while another tide gauge is located in the Mediterranean Sea. Merrifield et al. (2009) showed that mean sea level trends computed from tide gauges in the southern hemisphere are much different than those

computed from tide gauges in the northern hemisphere, suggesting that the agreement seen between the nine gauges of Holgate (2007) and the 177 tide gauges from Holgate and Woodworth (2004) is either a coincidence or, more likely, the product of selective editing.

The concept of "careful" editing of tide gauges is one that propagates throughout recent literature on computing trends from tide gauges. Until recently, most tide gauge-based estimates of GMSL change were computed as the average of linear trends obtained from a relatively small number of tide gauges (Peltier and Tushingham, 1991; Douglas, 1991). The assumption of these studies was that by selecting gauges with a suitably long time series (at least 60 to 70 years), the impact of low-frequency variability on the trend estimate could be minimized. In addition to editing based on record length, tide gauges in tectonically active regions were removed and the remaining gauges were grouped into 10 different geographic areas. The trend in GMSL computed for the period from 1880 to 1990 was found to be 1.8 mm/yr (Douglas 1991; 1997). One of the conclusions that can be drawn from these studies is the necessity to manually edit the tide gauge dataset and to discard any tide gauge with a potential problem. Without a tide gauge expert, it is suggested that it is difficult to produce a suitable and widely acceptable set of tide gauges to use for analysis.

More recently, attempts have been made to incorporate more tide gauges in the estimation of both global and regional sea level trends. Church et al. (2004) performed an EOF reconstruction of sea level using 426 tide gauges with measurements between 1950 and 2001. The authors suggest that their method allows for a larger number of tide gauges to be used in the computation of the GMSL time series. Interestingly, a trend of 1.8 mm/yr was found over the period from 1950 to 2001 (Church et al., 2004) and 1.7 mm/yr over the period from 1870 to 2004 (Church and White, 2006). Despite discarding fewer tide gauges, Church et al. (2004) implement

several standard editing criteria, as well as editing and removing some tide gauges based on visual inspection.

Should tide gauges simply be edited in such a way that the trend over the last century produced by the dataset is close to 1.8 mm/yr? Is it best to use relatively few "carefully" selected tide gauges or rather more "less carefully" selected tide gauges? In an attempt to answer this question, several tide gauge datasets are produced using a variety of editing criteria. In addition to performing a reconstruction with each dataset, a GMSL sea level time series is reproduced for each. By comparing the results, it can be shown how trend estimates vary and how sensitive the reconstruction itself is to tide gauge editing.

In total, seven tide gauge datasets have been produced. The first set simply uses every tide gauge available in the PSMSL dataset with no user-defined editing. One set uses criteria similar to Church et al. (2004), while another is very similar to that used in Merrifield et al. (2009). A set of 89 tide gauges developed for an upcoming reconstruction paper by Ray and Douglas (2011) is also studied. The final three sets of tide gauges are created with defined editing criteria and no visual inspection. The first set retains only tide gauges with records longer than 40 years. The second set uses the longest record in every 10x10 degree box around the ocean, while the final set uses the longest record in every 5x5 degree box. The last two sets are an attempt to achieve a good spatial distribution of tide gauges and avoid regional clustering. A summary of the seven tide gauge datasets is given in Table 9.1.

The primary reconstruction that will be shown in the results section below is obtained by following procedures similar to those of CW (TG set #2), and the reader is referred to their paper for detailed information on the editing criteria. In summary, tide gauge records of short length

and tide gauges with unphysical datum shifts were removed, while also editing tide gauges undergoing a month-to-month change of greater than 250 mm. Although the set of tide gauges used in this paper is not identical to that of CW, an effort has been made to produce a dataset comparable to the CW tide gauge dataset. While it may be appropriate in future studies, no attempt has been made to avoid regional clustering when selecting tide gauge records for this set, resulting in large clusters of tide gauges in Europe, Japan, and North America. The use of tide gauges with very short records was avoided, instead favoring gauges with good coverage across the 60-year period wherever possible.

The monthly tide gauge data are linearly interpolated to weekly intervals to match the one-week temporal resolution of the altimeter-derived CSEOFs. Prior to this, gaps of 1 to 2 months are filled in the tide gauge records using cubic spline interpolation. The nearest grid point is found for each tide gauge as the basis functions obtained from the satellite altimetry are on a quarter-degree resolution grid. If the nearest grid point was further than 250 km away, the tide gauge in question was removed from the set. Finally, the available tide gauge records were averaged to produce a single time series if there were multiple tide gauges associated with a single spatial grid point. After the editing procedure, 508 tide gauges remained for use in our reconstruction compared with 426 for CW.

The PSMSL sea level data are relative sea level, therefore the records must be corrected for the ongoing glacial isostatic adjustment. The ICE-5G VM2 model described by Peltier (2004) is used for all seven datasets. Since an inverted barometer correction is applied to the satellite altimetry data, the sea level measurements from the tide gauges were corrected using an inverted barometer response of sea level to atmospheric loading based on the pressure fields from the NCEP/NCAR reanalysis (Kalnay et al. 1996).

Table 9.1. Different tide gauge sets considered for study of GMSL and sea level reconstruction.

#	Tide Gauge Set	Number of Tide Gauges	Editing Criteria
1	All PSMSL Gauges	1179	GIA Corrected, IB correction Applied
2	Church et al. (2004)	508	GIA Corrected, IB correction Applied, see Church et al. (2004)
3	Merrifield et al. (2009)	122	GIA Corrected, IB correction Applied, see Merrifield et al. (2009)
4	Ray and Douglas (2011)	89	GIA Corrected, IB correction Applied, see Ray and Douglas (2011)
5	40-year minimum	289	GIA Corrected, IB correction Applied, all TGs with < 40 year record length removed
6	5-degree box	268	GIA Corrected, IB correction Applied, longest record in every 5-degree box retained
7	10-degree box	143	GIA Corrected, IB correction Applied, longest record in every 10-degree box retained

While most of pre-processing of the tide gauge records is similar to that used in CW, two significant differences require mention. First, the annual and semi-annual cycle signals are not removed from the tide gauge time series prior to performing the reconstruction. One benefit of the CSEOF reconstruction is the ability to account for the MAC in the reconstruction procedure. The second significant departure from CW is that we fit the sea level measurements, not their

first derivative, to the LVs used in the reconstruction. Using first derivatives of the tide gauge record is a robust technique to overcome the fact that sea level measurements are made relative to a local datum that varies from one site to another (Holgate and Woodworth 2004; Church et al. 2004; Holgate 2007). Fitting CSEOFs to differenced tide gauge time series, however, is significantly more complicated than with EOFs, given the additional time-dependence of the CSEOF LVs. In the future an approach permitting the use of differenced tide gauge data may be adopted, but in the present work the time mean value is simply subtracted from each sea level record. This approach works well when fitting the altimeter-derived CSEOF basis functions, which are constrained to have a periodicity of one-year. The process of fitting the CSEOF basis functions is found to be relatively insensitive to the small datum shifts or biases that may occur in the edited tide gauges and the effect of not using differenced data can be minimized by selecting longer tide gauge records. Given the considerations above and after conducting some simple tests, it is determined that fitting of the CSEOF basis functions to differenced tide gauge data is not required for the 1950 to 2010 record. This is not likely true when extending the record to earlier than 1950 because the number of available tide gauges varies significantly, thus magnifying the effect of the unknown datum levels. This is the subject of ongoing work and will not be discussed at length here. To account for the secular GMSL trend in the reconstruction over the period from 1950 to 2010, however, differencing techniques must be used on the tide gauge records as will be discussed in section 9.3.4.

9.2.2 Satellite Altimetry Dataset

CSEOF basis functions for our reconstruction were estimated from the AVISO quarter-degree resolution multiple altimeter product based on satellite altimeter measurements spanning

1992-2009 collected by the TOPEX/Poseidon, ERS-1&2, Geosat Follow-On, Envisat, Jason-1 and OSTM satellites. This updated and reprocessed gridded data product, which was released in June 2010, was created using the delayed time Ssalto/DUACS multi-mission altimeter data processing system with improved homogenous corrections and inter-calibration applied to the entire data record. Global crossover minimizations (LeTraon and Ogor, 1998) and local inverse methods are used to derive inter-calibrated highly accurate along track data that are referenced to a consistent mean. The along track data were then merged through a global space-time objective mapping technique that takes into account correlated noise (Ducet et al., 2000; LeTraon et al, 1998).

Very little additional processing is applied other than removing the mean and a linear least-square fit from the time series at each spatial grid point. The seasonal signal was not removed from the time series prior to computing the CSEOFs. Before CSEOF decomposition, the data was weighted using the square root of the cosine of latitude to yield an area-weighted variance decomposition, grid points at locations with an ocean depth of less than 1000 m were flagged to mitigate deficiencies in the gridded product associated with measurement and processing errors in shallow water and near the coast, and any grid points without a continuous record over the entire time period were also flagged.

9.3. Methods

Using basis functions computed from a short, spatially dense dataset to interpolate a long time series of spatially sparse observations was first implemented in sea surface temperature (SST) studies. Smith et al. (1996) computed EOFs from twelve years of satellite-derived SST data and used them as basis functions to estimate global SST temperature fields from 1950 to

1992. Kaplan et al. (1998; 2000) improved on this procedure by adding weighting dependent on known errors in the data to the reconstruction procedure. Sea level reconstructions soon followed using the techniques developed for SST. The mathematical details are found in Kaplan et al. (2000) and CW, and will only be discussed briefly here.

9.3.1 Previously Published Sea Level Reconstructions

Ch02 computed EOF basis functions from seven years of satellite altimetry data and used the Smith et al. (1996) technique to create a sea level reconstruction from tide gauges. Ch02 removed the linear trend and annual signal from both the altimetry and tide gauge data prior to reconstruction. As given in equation 7.1, the satellite altimetry is initially decomposed into a series of loading vectors (LVs) and PC time series (PC). These LVs are fit to the tide gauge data to compute a time series of amplitudes corresponding to a PC time series. More specifically, the reconstructed sea level fields H are given by:

$$H(r,t) = \sum_n V_n(r)\alpha_n(t) \qquad (9.1)$$

where V is the loading vector (substituted for LV to save confusion in the equations below) computed from satellite altimetry and $\alpha(t)$ is the time series of the amplitude of the LV. Smith et al. (1996) and Chambers et al. (2002) compute the value of $\alpha(t)$ at each month by minimizing the cost function:

$$S(\alpha) = (V\alpha - H^0)^T (V\alpha - H^0) \qquad (9.2)$$

where H^0 are the tide gauge observations. Note, LV is sub-sampled at each of the tide gauge locations and does not contain every value from across the globe.

In their more recent reconstruction, CW also computed basis functions from seven years of altimetry data. However, they adopt the more sophisticated technique of Kaplan et al. (2000) by adding weighting to their cost function. The amplitudes of their LVs are found by minimizing the cost function:

$$S(\alpha) = (V\alpha - H^0)^T M^{-1}(V\alpha - H^0) + \alpha^T \Lambda \alpha \qquad (9.3)$$

where Λ is a diagonal matrix of the eigenvalues of the covariance matrix and M is the error covariance matrix, given by:

$$M = R + V\Lambda V^T \qquad (9.4)$$

Here, R is the variance of the instrumental error, and the second term represents the errors of omission introduced by deleting higher-order EOFs in the reconstruction. Once the cost function is minimized, the resulting amplitudes are given by:

$$\alpha = PV^T M^{-1} H^0 \qquad (9.5)$$
$$P = (V^T M^{-1} V + \Lambda^{-1})^{-1}$$

The amplitude of each LV is computed simultaneously. In other words, if ten different LVs are used, the solution procedure will produce ten amplitude time series, one for each LV.

In addition to following the procedure of Kaplan et al. (2000), CW accounted for the secular trend in the tide gauge data by adding an artificial constant basis function to the EOFs used in the reconstruction, and the annual cycle signal was removed from both the tide gauge and satellite altimetry data prior to analysis. The CW reconstruction was later updated (Church et al., 2006), and is the most widely cited and available reconstructed sea level dataset. Nevertheless, no published work to date has evaluated or attempted to improve upon the CW reconstruction

technique. Three main issues have been identified to investigate ways in which this reconstruction could be improved: 1) choice of basis functions, 2) selection of weighting scheme, and 3) method of accounting for GMSL.

9.3.2 Basis Functions: CSEOFs vs. EOFs

When compared to CSEOFs, EOFs have characteristics that make them suboptimal for use as basis functions for sea level reconstruction. EOFs enforce a stationarity on the spatial variability. A single spatial map defines the basis function, and the reconstruction procedure simply computes the amplitude modulation of this map through time. Given the evidence that many signals in geophysical data are cyclostationary, CSEOFs provide significant advantages over EOFs when dealing with signals such as the MAC and ENSO.

As mentioned above, CSEOFs are defined to be periodic with a certain nested period. When focusing on the annual and ENSO signals, the nested period is defined to be one year. In chapter 8 and in Hamlington et al. (2010), the ability of CSEOF analysis with a nested period of one year to extract the MAC and ENSO signals from the AVISO satellite altimetry data has been demonstrated. Figs. 8.1 and 8.2 show CSEOF modes 1 and 2 computed from 17 years of the AVISO multi-satellite altimetry data. These two modes capture the MAC and ENSO signal, respectively, and account for nearly 50% of the sea level variability. For the weekly AVISO data, 52 separate LVs are obtained for each mode (only 12 interpolated monthly LVs are shown in Figs. 8.1 and 8.2 in the interest of conserving space), with the PC time series representing the amplitude modulation of these LVs over time.

The one-year periodicity associated with the annual cycle is not seen in the PC time series of mode one (Fig. 8.1), but instead is contained in the twelve LVs. Fig. 8.2 shows the

annual cycle contribution to GMSL calculated by combining the mode 1 LVs and PC time series. The one-year cycle and its lower frequency modulation are apparent, and one begins to appreciate how a CSEOF mode is both similar and different to an EOF mode. Additionally, as a result of the relationship between the annual cycle and ENSO signal, a one-year nested period results in a mode directly linked to the ENSO variability in the satellite altimetry data (Fig. 8.3). Only nineteen CSEOF modes are needed to explain 95% of the variance in the altimetric record. When performing sea level reconstructions, every LV space/time pattern associated with an individual CSEOF mode is fit simultaneously, which reduces the sensitivity of the resulting reconstruction to sampling error associated with the limited number of tide gauge measurements and to erroneous tide gauge measurements at a single point in time. This allows more robust reconstructions to be produced using fewer tide gauges when compared to reconstruction techniques using EOF basis functions.

The MAC signal is well captured by the first CSEOF mode and there is no leakage into the second mode, which is associated with ENSO variability in the altimetry record (illustrated in Figs. 8.1 and 8.3). On the other hand, when performing EOF decomposition, the annual cycle signal is spread across several computational modes, which is a well-known issue with EOF analysis (North, 1984; Kim and Wu, 1999; 2001). Therefore, CSEOF basis functions allow for the reconstruction of specific signals, such as those attributed to the MAC or ENSO. More important, if a CSEOF mode can be physically interpreted and identified as belonging to a certain climate or geophysical process, the mode can be used as a basis function to reconstruct that process back in time. This has important implications for climate monitoring and allows for the possibility of estimating the MAC or ENSO signal dating back to the earliest tide gauge measurements. EOF basis functions, on the other hand, do not separate physical processes nearly

as well, making it more difficult to reconstruct cyclostationary signals. In the Ch02 and CW sea level reconstructions, the annual and semiannual cycle signals are removed from both the satellite altimetry data and tide gauge data prior to performing the reconstruction.

9.3.3 Weighting Scheme

In addition to the choice of a basis function, careful consideration must be given to the weighting scheme used in the reconstruction procedure since the amplitudes of each basis function are calculated by solving a weighted least squares problem. Kaplan et al. (2000) and CW utilize truncation and measurement errors for weighting, while Smith et al. (1996) and Ch02 omit weighting. As discussed in M09, the sparse spatial distribution of the tide gauges must be taken into account to get a meaningful estimate of GMSL from tide gauges. Although regional clustering around heavily populated areas can be avoided by careful selection of tide gauges, it is difficult to account for the latitudinal differences in the number of tide gauges used in the analysis. There are many more tide gauges in the northern hemisphere when compared to the southern hemisphere, and weighting each tide gauge equally would lead to a reconstruction strongly biased by northern hemisphere signals. In their paper, M09 show the disparity between GMSL trends in the southern hemisphere vs. the northern hemisphere over the last fifty years. For this reason, a more appropriate weighting may be one similar to the one M09 employed that uses weights inversely proportional to the number of tide gauges in each ten-degree latitude band while also accounting for the relative differences in ocean area contained in each band. This weighting scheme should lead to a more accurate sea level reconstruction and a more accurate estimate of GMSL.

9.3.4 GMSL

Estimating GMSL using reconstruction techniques is not a trivial task. While CSEOF basis functions describe the periodic variability in sea level, as a result of initial detrending prior to computation, no single CSEOF or sum of CSEOFs represents the secular trend. CSEOF analysis is capable of extracting the secular trend from the AVISO data, but we cannot assume that the resulting spatial pattern is true for the entire 60-year time period. CW approximate the trend in their reconstruction by introducing a constant basis function that is intended to effectively calculate a weighted average of the sea level measured by the tide gauges at each point in time and distributes that mean value to every spatial point in the reconstruction. This leads to mean sea level being very similar when values are averaged independently over the northern and southern hemispheres, which contradicts the tide gauge analysis of hemispheric mean sea level presented in M09. Fig. 9.1 shows the similarity between mean sea level computed over both the northern and southern hemispheres, while Fig. 9.2 shows the mean sea level similarities when computed over even smaller regions. Furthermore, the CW method of handling GMSL also does not account for sampling biases caused by the sparse distribution of tide gauges. On a global scale, each of the reconstructed CSEOF modes has a small secular trend. However, when sampled at the tide gauge locations, the individual modes could contribute significant trends to GMSL.

Rather than introducing an additional basis function in an attempt to account for the secular trend as in CW, we compute our reconstruction with secular trends present in the tide gauge sea level measurements. No ad hoc basis function is needed since the altimetry-derived CSEOF basis functions are insensitive to the secular trend due largely to the annual nested

periodicity imposed on the spatial and temporal variability of the relatively short altimetric record. The following procedure is used to estimate GMSL, including the secular trend.

a. The full CSEOF reconstruction is computed and subsampled at each of the tide gauge locations.

b. The subsampled reconstruction is then differenced, ensemble averaged using latitude-band weighting, and finally re-integrated (first differences of the tide gauge data are used to mitigate the lack of a consistent datum for the tide gauges).

c. The raw tide gauge data is also differenced, averaged using latitude-band weighting, and then re-integrated to form a GMSL time series associated with the original tide gauge data.

d. The time series computed in part (b) is subtracted from the time series computed in part (c) to form an estimate of the GMSL time series with all reconstructed signals removed, including the MAC and ENSO, thus correcting for any trend resulting from the spatial subsampling of signals captured by the reconstruction.

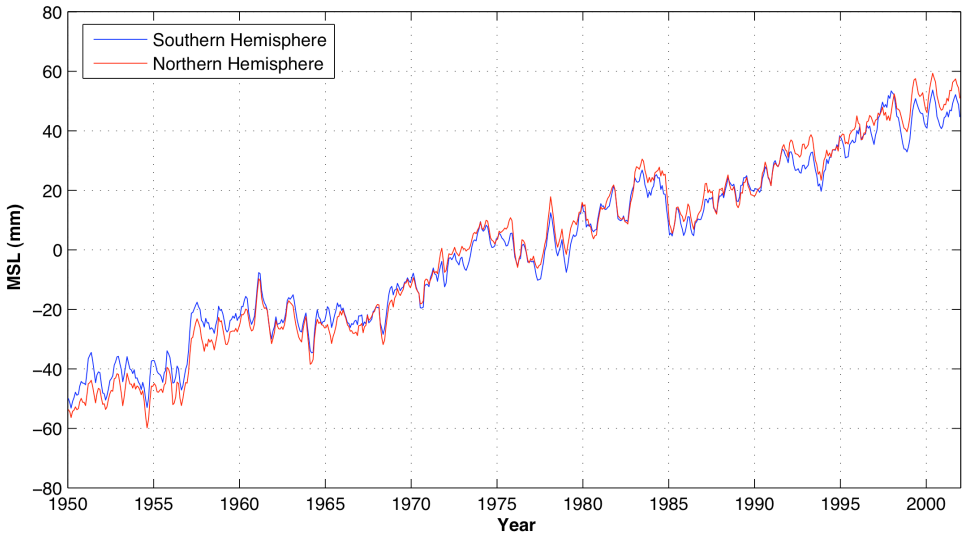

Figure 9.1. Mean sea level computed for the southern and northern hemispheres from the sea level reconstruction of Church et al. (2004) over the period from 1950 to 2001.

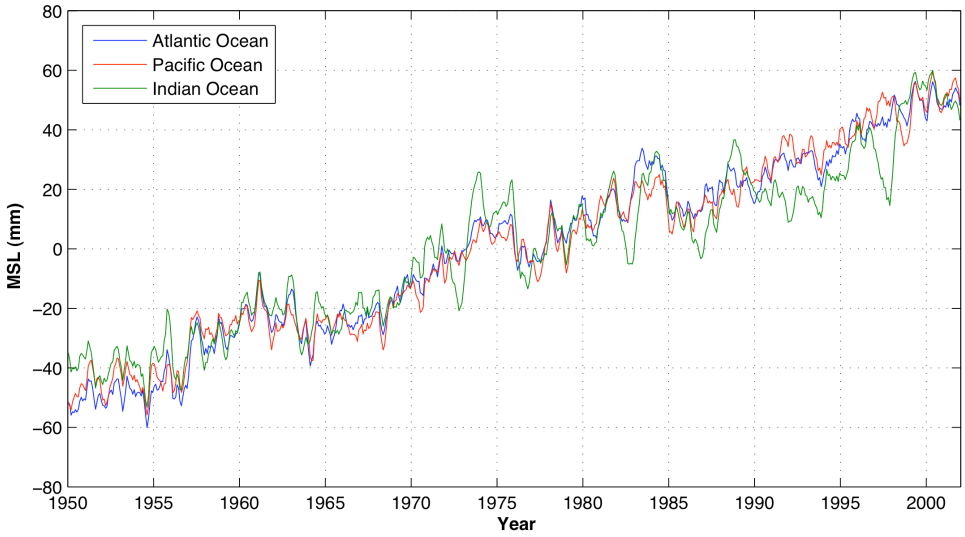

Figure 9.2. Mean sea level computed for the Atlantic (Blue), Pacific (Red) and Indian (Green) Oceans from the sea level reconstruction of Church et al. (2004) over the period from 1950 to 2001.

9.4. Results

With the considerations outlined above, a CSEOF sea level reconstruction for 1950-2009 has been computed using latitude-band weighting and a set of tide gauges obtained using editing criteria very similar to that described in CW (tide gauge set #2). An inverse barometer correction was applied to both the tide gauge data and the altimetry, and no attempt was made to remove the annual cycle signal. The basis functions for the reconstruction are given by a CSEOF decomposition of the AVISO merged satellite altimetry data spanning the period 1993 through 2009. Before decomposition, the time series at each grid point was detrended by removing a least squares fit linear trend and the resulting value was area-weighted by multiplying by the square root of the cosine of the latitude to yield an area-weighted variance decomposition. A nested period of one year was used to capture the variability associated with the MAC and ENSO. While other (longer) nested periods could be used, the selection of one year allows robust representation of the variability associated with both the MAC and ENSO (Figs. 8.1 and 8.3). As

mentioned above, the 19 leading CSEOF modes describe 95% of the variability in the original dataset. Once obtained, these 19 CSEOF modes are used as basis functions and fit to the tide gauge data using weighted least squares. Results obtained using this reconstructed dataset are described below.

9.4.1 Comparison to Altimetry

Since the LVs for the AVISO satellite altimetry CSEOF decomposition and the reconstructed dataset are identical, the goal of our work is to reproduce the PC time series associated with each LV (basis function) back through time using the tide gauges. The tide gauge reconstructed PC time series for the first five CSEOF modes are shown in Fig. 9.3 overlaid with the original altimeter-derived PC time series. The quality of the reconstruction is clearly seen by the close agreement between the two. The first mode captures the MAC well and the result is stable back to 1950, demonstrating the significant advantage of the CSEOF method versus sea level reconstructions computed using EOF basis functions without the annual cycle. The second mode in Fig. 9.3 captures ENSO. The correlation between tide gauge reconstructed and altimetry PC time series is 0.97 between 1993 and 2009. Similarly, modes 3, 4, and 5 have correlations of 0.94, 0.82 and 0.67, respectively, over the same time period. These high correlations demonstrate the ability of the CSEOF reconstruction method to estimate modes from sparse tide gauge samplings that agrees very well with the modes derived from satellite altimetry.

While the comparison of the PC time series arising from the reconstruction and CSEOF decomposition of the satellite altimetry gives an indication of the quality of the reconstruction, there is a direct comparison between the reconstructed sea level data and the AVISO satellite altimetry data. The regional trends over the period 1993 through 2009 are computed for both the

AVISO data (Fig. 9.4A) and the CSEOF reconstruction data (Fig. 9.4B). We observe good agreement between the two trend maps, particularly in the Pacific and Atlantic Oceans. The spatial distribution of the correlation between the CSEOF reconstruction and AVISO data (Fig. 9.4C) over the 17 years from 1993 to 2009 has a global area-weighted average of 0.68, with much higher correlations in the tropics.

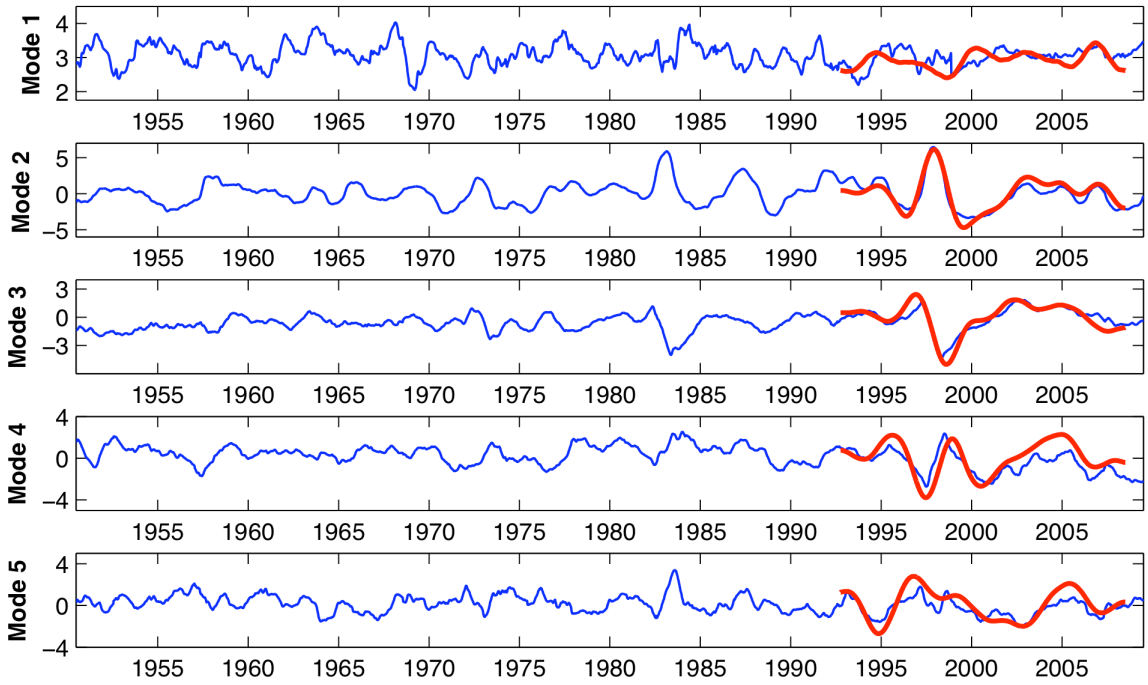

Figure 9.3. Reconstructed amplitudes computed for the first five CSEOF modes (blue). The first mode is associated with the annual cycle while the second mode is associated with the ENSO signal. The CSEOF PC time series (red) computed from the altimetry data are also plotted and seen to have excellent agreement with the computed amplitudes.

As noted in CW, the higher correlation in the tropics reflects the dominance of the low-order basis functions that contain the variability associated with the large-scale signals in the data. The correlations found in the northern Pacific Ocean and Atlantic Ocean using the CSEOF

reconstruction are markedly higher than those found from the EOF reconstruction of CW, suggesting that CSEOFs better capture the ocean variability in those regions.

9.4.2 Comparison to other sea level data

As with any new technique, it is important to compare how the new results compare to results obtained from previous techniques. The CW dataset covering the period 1950 to 2001 is publicly available through the PSMSL website and can be used for comparison to our CSEOF reconstructed sea level data. CW use TOPEX/Poseidon satellite altimetry data from 1993 through 2001 to compute their basis functions. Their reconstructed data compares favorably to the satellite altimetry data over this time period. As expected, the trends computed from the CSEOF reconstruction from 1993-2001 (Fig. 9.3A) show good agreement with the CW trends over the same period (Fig. 9.3B). However, there is little agreement between the spatial variability of the trends computed from the CSEOF reconstruction (Fig. 9.5C) and the CW reconstruction (Fig. 9.5D) when comparing the trends computed from 1950-2001. This could be a result of the different basis functions, different tide gauge set, and/or different weighting scheme. Since these datasets are the only two available sea level reconstructions, it is difficult to determine which is more accurate without independent comparisons.

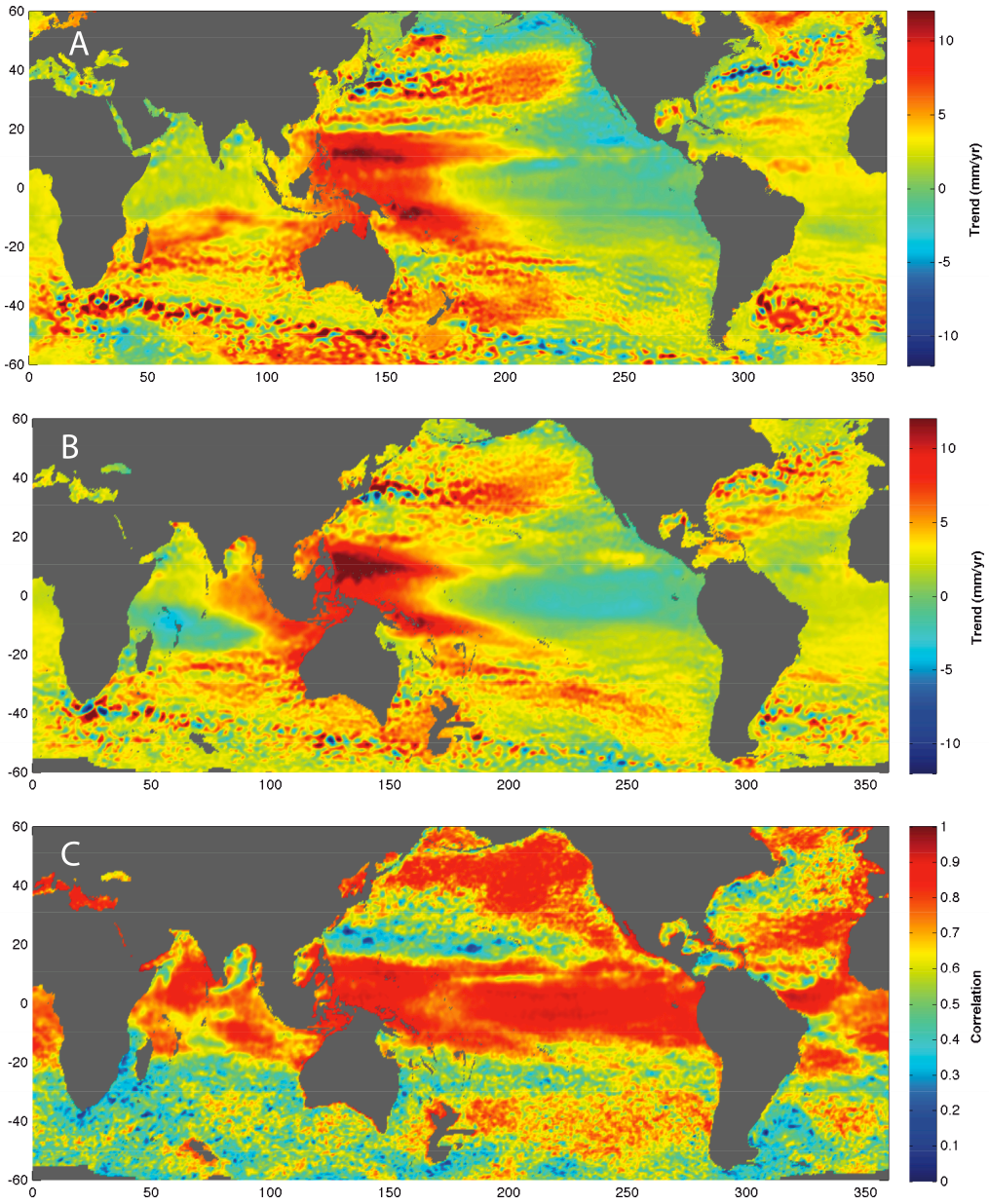

Figure 9.4. Regional sea level trends from 1993 to 2009 computed from the AVISO satellite altimetry data (A) and from the CSEOF reconstruction (B). The spatial variation of correlation between the AVISO and CSEOF reconstruction data over the same time period is also shown (C).

In a recent paper, Han et al. (2010) identified the spatial pattern of sea level change in the Indian Ocean since the 1960s by analyzing independent oceanographic and atmospheric datasets, performing model experiments using Ocean General Circulation Models (OGCM) and Atmospheric GCMs, and analyzing coupled global climate model solutions. They suggested that the spatial pattern of sea level change is robust to cross-data sampling and cross-model differences, and agree well with tide gauge and satellite observations during their overlapping periods. Qualitatively, the Indian Ocean trends in Han et al. (2010) (Fig. 9.6C) appear to agree better with the trends computed from the CSEOF reconstruction (Fig. 9.6B) than with the CW reconstruction (Fig. 9.6A) when computed over the period 1961 through 2001, particularly in the southern tropical and eastern areas of the Indian Ocean. This independent validation of the CSEOF reconstruction from 1961 through 2001 suggests that the CSEOF-based technique likely provides improved estimates of sea level trends from 1950-2009 when compared to past sea level reconstructions at least for the dominant trend signal in the Indian Ocean.

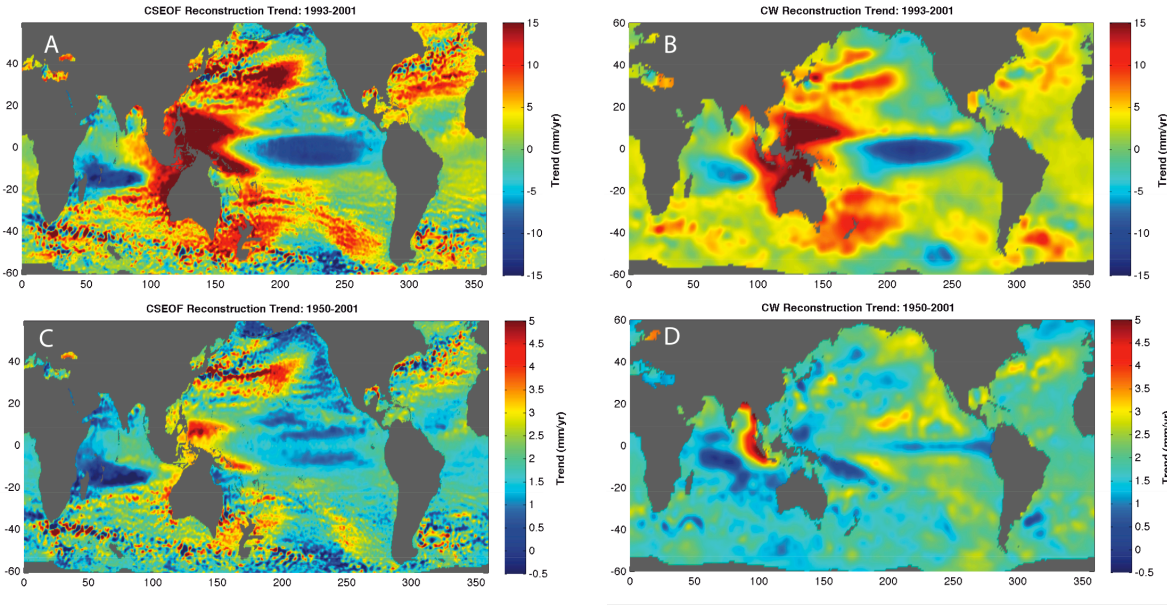

Figure 9.5. Regional sea level trends from 1993 to 2001 computed from the CSEOF reconstruction (A) and from the CW EOF reconstruction (B), and from 1950 to 2001 computed from the CSEOF reconstruction (C) and the CW EOF reconstruction (D).

9.4.3 ENSO

ENSO is described by CSEOF mode 2 in both the satellite altimetry (Fig. 8.3) and the reconstructed sea level (Fig. 9.3). A variety of indices are used to monitor ENSO. One commonly cited index is the Multivariate ENSO Index (MEI). The MEI is computed using six different variables, but does not include SSH measurements (Wolter and Timlin 1998**)**. In Fig. 9.7, the reconstructed ENSO mode is shown along with the MEI for the period 1950 to 2009. The correlation between the MEI and the reconstructed ENSO (mode 2) is 0.91. Although CW found a single EOF mode related to ENSO, the correlation between their reconstructed amplitude and the Southern Oscillation Index (SOI) was only 0.78 over from 1950 to 2000**,** underlining the ability of the CSEOF-based technique to better reconstruct the ENSO signal back in time.

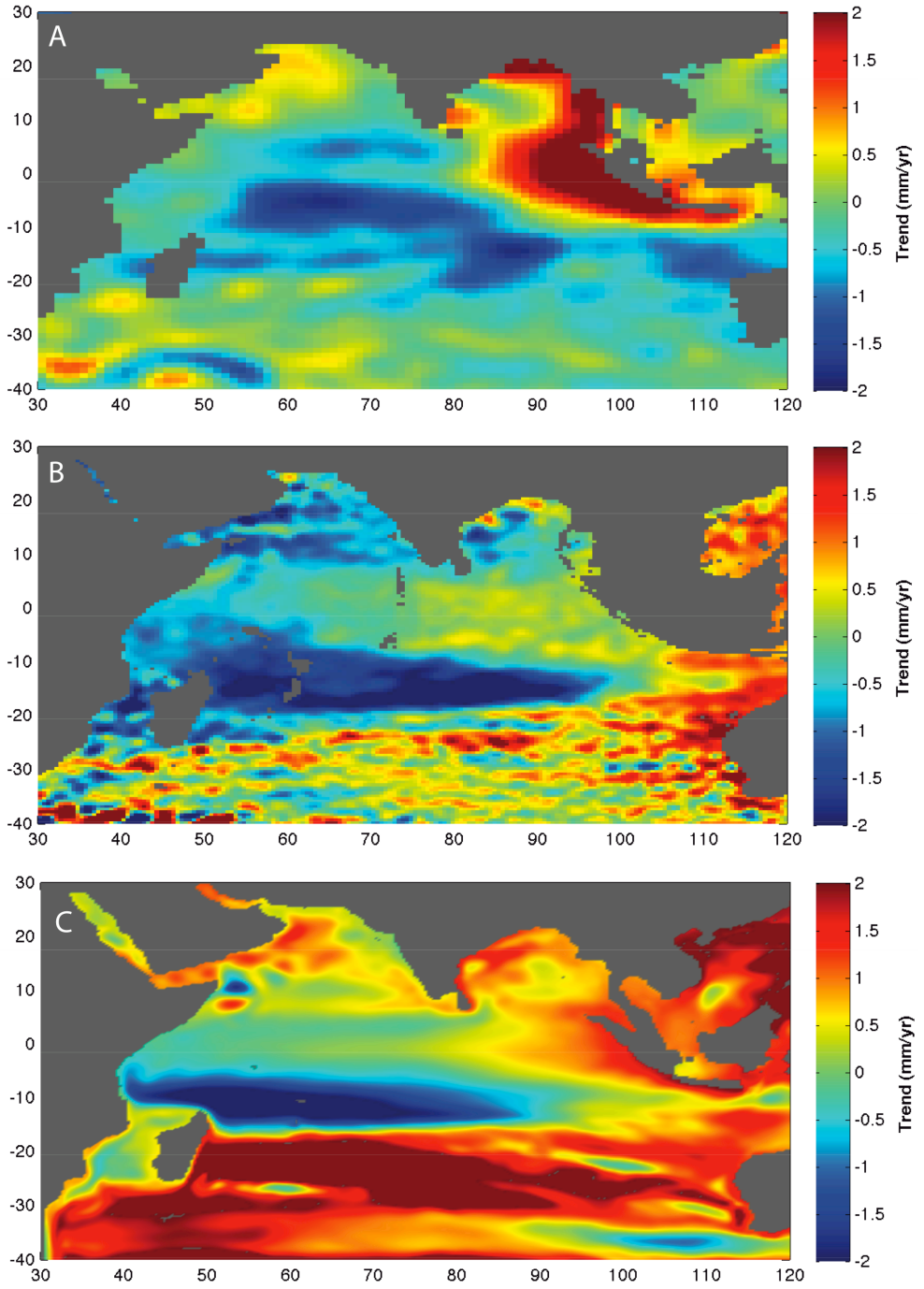

Figure 9.6. Regional sea level trends from 1961 to 2001 computed from the CW EOF reconstruction (A), from the CSEOF reconstruction (B), and from the HYbrid Coordinate Ocean Model solution of Han et al. (2010) (C). Note, different bathymetry editing was applied to the datasets used to compute the three figures above.

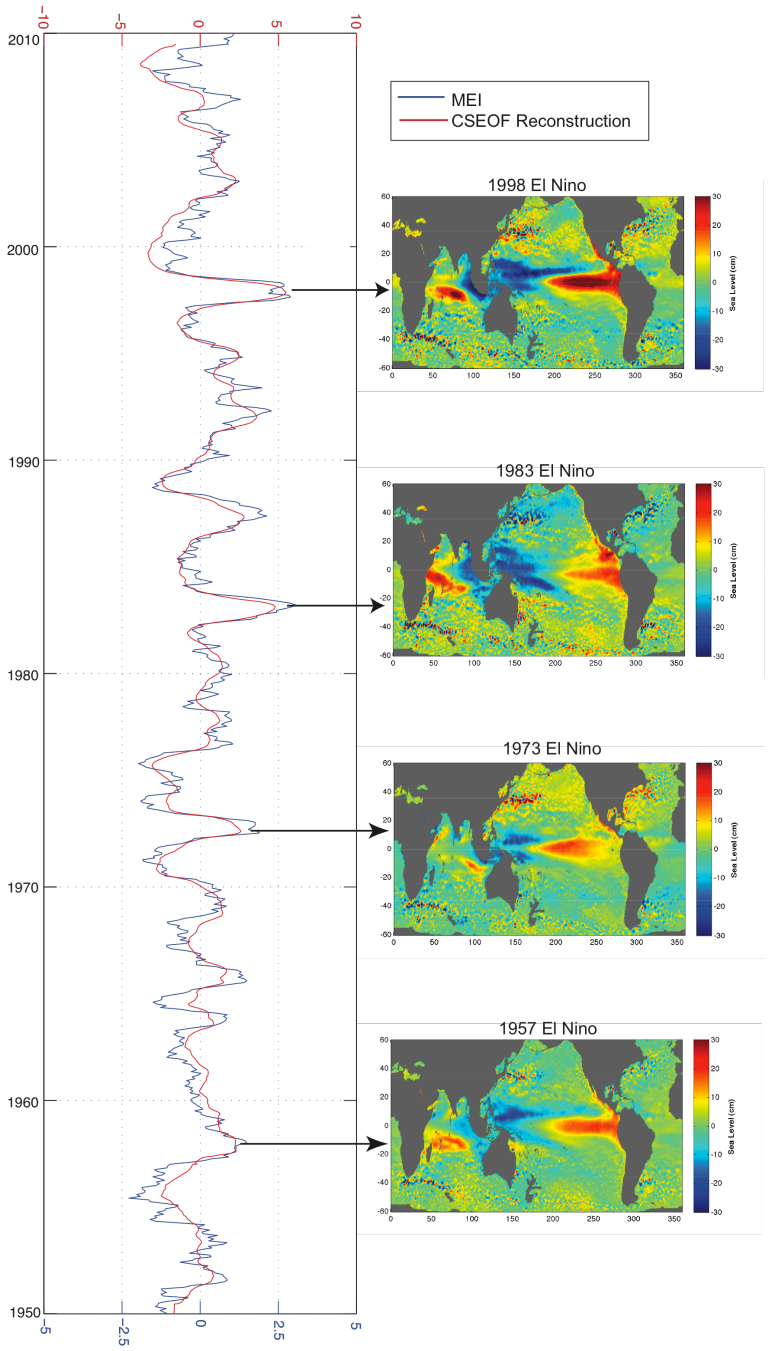

Figure 9.7. ENSO SSH index calculated from reconstructed CSEOF mode 2 (red line) with comparison to MEI (blue line) from 1950 to 2009. The spatial maps of sea level for four significant El Niño events over the 60-year record are also shown.

While a single CSEOF mode captures the signal represented in common ENSO indices, it is unlikely that this is the entirety of the signal. Recent studies suggest that ENSO cannot be explained by a single index or mode, but is better defined as a set or series of dynamical modes (Compo and Sardeshmukh 2010). By using CSEOFs, it is likely that we are capturing most of the ENSO dynamical signal in a single mode; however, initial reconstructions also suggests that higher order modes may explain other components of the ENSO signal. The third CSEOF mode in Fig. 9.3 likely captures the El Niño Modoki signal (Ashok et al. 2007). Unlike the more common eastern Pacific El Niño, the El Niño Modoki signal is a central Pacific event and shows a weak negative correlation with the more traditional ENSO signal. The reconstructed PC time series has a correlation of 0.57 with an El Niño Modoki SST index computed from the Extended Reconstructed Sea Surface Temperature (ERSST) over the period from 1950 to 2010 (Fig. 9.8). The LVs of the third CSEOF mode also confirm the relation to a central Pacific ENSO signal. While the first three reconstructed modes seem to be relatively easy to interpret physically, further analysis is needed of the higher modes to gain a more thorough understanding of their physical basis. It is also possible that the higher order modes do not represent a particular physical process individually, but rather some combination of modes has physical meaning. This will be the subject of future work.

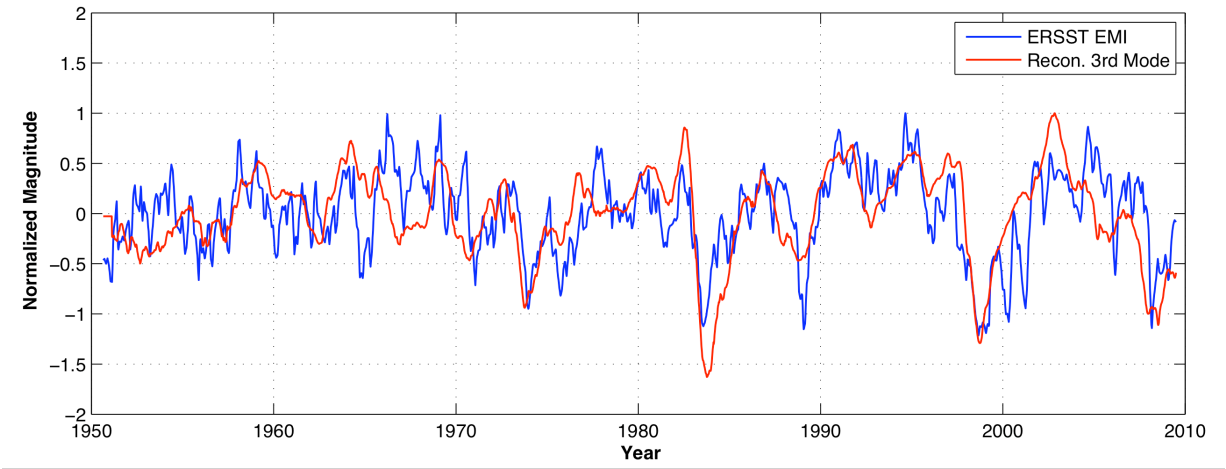

Figure 9.8. El Niño Modoki Index EMI computed from the reconstructed SSH (red), specifically the third mode of the reconstruction. The EMI computed from the ERSST dataset is also shown, with a correlation of 0.57 between the two over the period from 1950 to 2010.

9.4.4 Global Mean Sea Level

The GMSL time series computed from a sea level reconstruction is heavily dependent upon the tide gauge dataset that is used. As discussed in section 9.2.1, seven different tide gauge datasets are used for computing GMSL, including the dataset used to produce the results shown in sections 9.4.1 to 9.4.3. GMSL trends over the periods from 1950 to 2009 and from 1993 to 2009 are estimated for each set. Additionally, a CSEOF reconstruction is performed for each tide gauge dataset, and the correlations between the second and third modes with the MEI and the EMI, respectively, are computed. Finally, the trends in the northern and southern hemispheres are calculated. Both latitude-band weighting and equal weighting are used for all the calculations listed above. The results are summarized in table 9.2 for each of the seven tide gauge datasets considered.

Table 9.2. Trends computed from seven different tide gauge datasets. Datasets are numbered according to table 9.1.

#	Weight.	Trend: 1993-2009	Trend: 1950-2009	Southern Hemisphere 1950-2009	Northern Hemisphere 1950-2009	MEI Correlation 1950-2009	EMI Correlation 1950-2009
1	Lat	3.09	2.21	3.08	1.23	0.88	0.62
	Mean	2.72	2.08	1.95	1.20		
2	Lat	3.16	1.88	1.24	2.56	0.91	0.57
	Mean	3.18	2.15	0.73	2.38		
3	Lat	3.84	2.48	1.55	1.83	0.86	0.49
	Mean	2.53	1.54	0.63	1.77		
4	Lat	3.34	1.73	2.11	2.88	0.85	0.45
	Mean	3.08	2.19	1.43	2.50		
5	Lat	3.04	0.98	2.72	0.76	0.80	0.39
	Mean	2.85	1.67	0.64	1.78		
6	Lat	2.92	2.87	2.96	2.90	0.82	0.54
	Mean	2.05	2.29	1.81	2.41		
7	Lat	2.98	3.34	3.90	1.51	0.74	0.50
	Mean	1.74	1.69	2.47	1.40		

The trends shown in table 9.2 highlight some of the difficulties in estimating GMSL from tide gauges. Not only do trends differ greatly from different sets of tide gauges, there is a significant difference depending on the type of weighting used in the calculation. Tide gauge datasets 1 through 4 produce results most in-line with previously published estimates, while sets 5 through 7 must be questioned given the large trends estimated over the 1950 to 2009 time period. The trends in the southern and northern hemispheres also show very little agreement between tide gauge datasets. Merrifield et al. (2009) suggest that the trend from 1950 to 2009 should be higher in the southern hemisphere than the northern hemisphere, but this is reflected in only tide gauge datasets 1, 5, 6 and 7.

Although the GMSL is very sensitive to the tide gauge dataset, it is important to consider how the reconstruction procedure itself is affected by different sets of tide gauges. Table 9.2 summarizes the correlation between the reconstructed PC time series for ENSO CSEOF mode with the MEI over the time period from 1950 to 2009. Despite the questionable trends from some of the tide gauge datasets, only one produces a correlation below 0.80. Similarly, for the correlation between the PC time series for the third CSEOF mode and the EMI, values generally above 0.50 are obtained. Interestingly and perhaps not surprisingly, the two tide gauge datasets (#1 and #2) that provide the best correlations are also the two containing the most tide gauges. In general though, the reconstruction of these two signals does not appear to be very sensitive to the tide gauges used in the reconstruction procedure, and one would then expect the overall results, such as those shown in sections 9.4.1 to 9.4.3, to be similarly insensitive.

In addition to simply estimating the trends, the GMSL time series can be computed from each set of tide gauges using both a simple mean calculation and latitude-band weighting. The

procedure for computing GMSL is as follows: 1) remove annual cycle using a least-squares fit; 2) compute first differences of the edited tide gauge data; 3) compute a simple mean or weighted mean of all available tide gauges at each point in time; 4) re-integrate to obtain a GMSL time series in physical units. Note that this computation is completely independent of the CSEOF reconstruction and is designed only to highlight the differences in GMSL that arise from different tide gauge datasets. Fig. 9.9 shows the GMSL time series estimated for each of the seven tide gauge datasets using both a simple mean calculation and latitude-band weighting, and serves to highlight the significant differences shown in Table 9.2. In addition to GMSL, MSL for both the northern and southern hemispheres are computed following the same procedure outlined above. The resulting trends in each hemisphere are shown for the different tide gauge datasets in Fig. 9.10. Only latitude-band weighting is used to obtain these time series. Finally, similar to the study of Merrifield et al. (2009), the 15-year trends in GMSL are computed for each of the seven tide gauge datasets using latitude-band weighting. This gives a better indication of the differences in decadal time-scale variability in GMSL for differing sets of tide gauges. The results are shown in Fig. 9.11, with tide gauge datasets 1 through 4 providing the most agreement. The results for tide gauge dataset #3 are similar yet different to those shown in Merrifield et al. (2009), underscoring the fact that while the dataset should be representative of what is in their work, there are still significant differences.

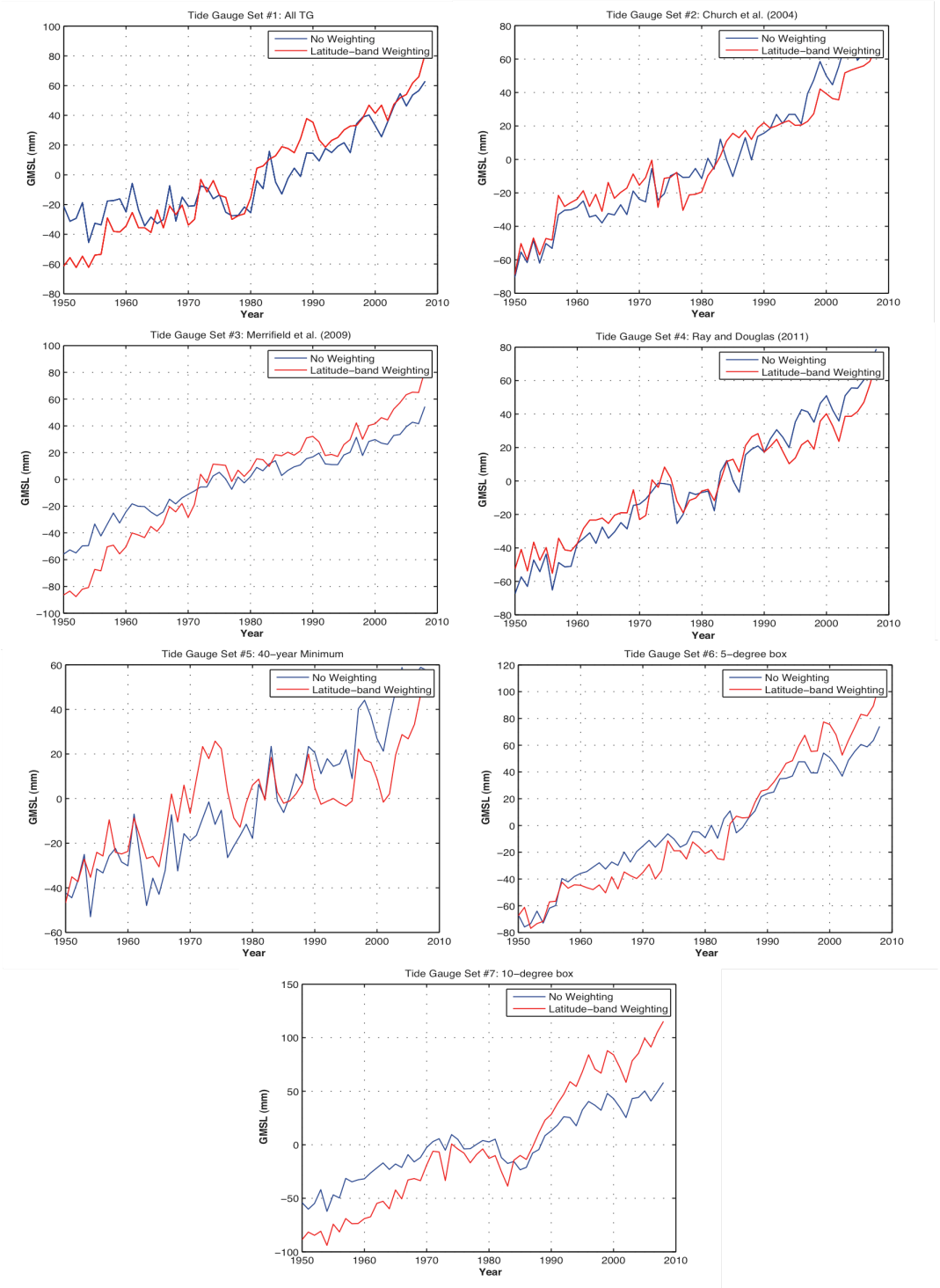

Figure 9.9. GMSL computed for each of the seven tide gauge datasets using both a simple mean calculation (blue) and latitude-band weighting (red). GMSL trend estimates for each dataset are summarized in table 9.2.

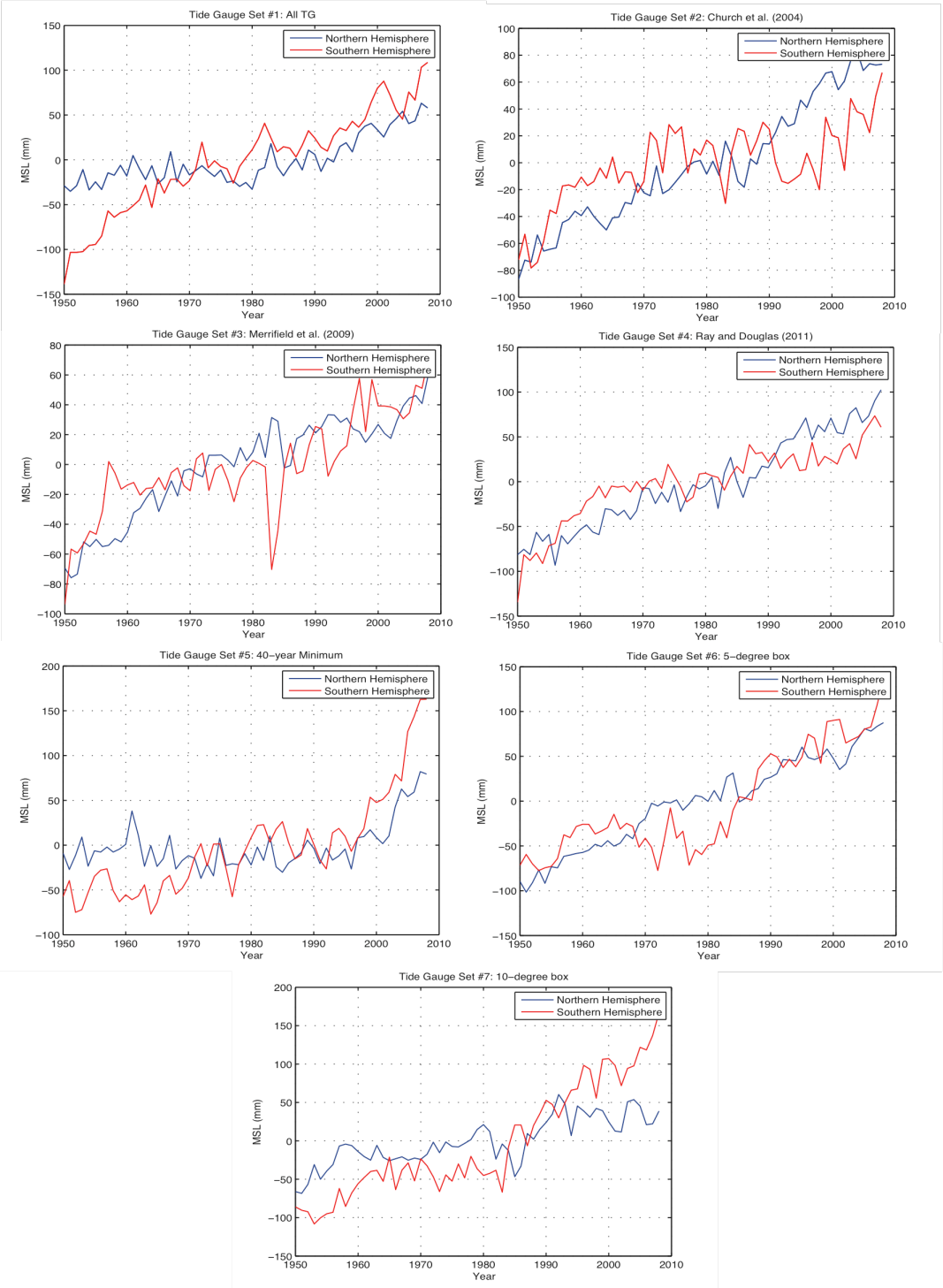

Figure 9.10. MSL of both the southern (red) and northern (blue) hemispheres computed for each of the seven tide gauge datasets using latitude-band weighting. MSL trend estimates are summarized in table 9.2.

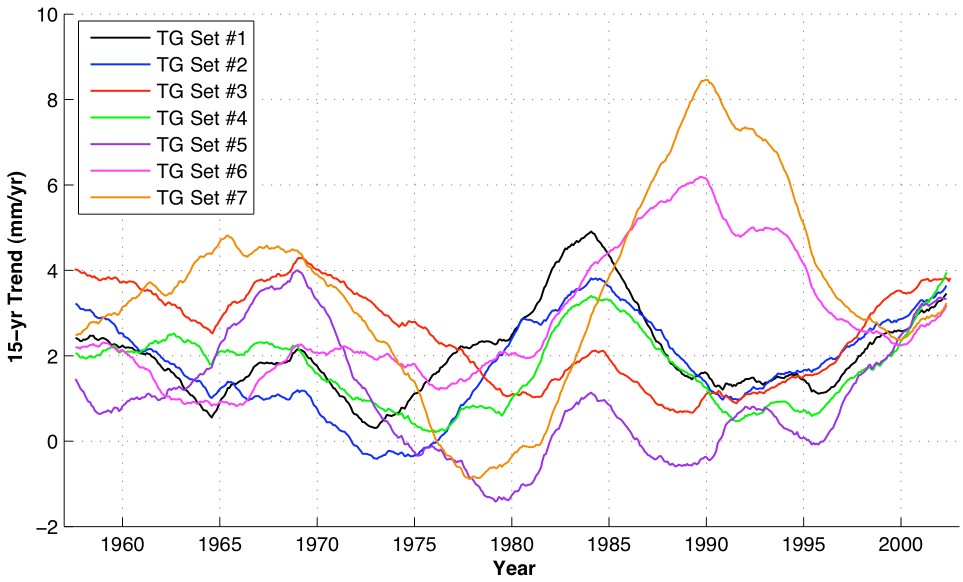

Figure 9.11. 15-year trends over the period from 1950 to 2010 for each of the seven tide gauge datasets considered. Latitude-band weighting is used for computing the trends.

As mentioned above, the reconstruction results shown in sections 9.4.1 to 9.4.3 are computed using tide gauge dataset #2 with editing criteria similar to Church et al. (2004). The trend in GMSL from 1950 to 2009 is estimated to be 1.81 mm/yr (Fig. 9.12), using the CSEOF reconstruction and the technique outlined in section 9.3.4 for correcting the trend. Meanwhile, the subsampled reconstruction accounts for 0.08 mm/yr of GMSL trend at the tide gauge locations. Without correcting for the sampling bias using the reconstruction, a trend of 1.88 mm/yr is found using latitude-band weighting of the tide gauges. For comparison, the CW estimate the trend in GMSL to be 1.8 mm/yr from 1950 through 2001 with the trend from the CSEOF reconstruction computed to be 1.73 mm/yr over the same period. While the two estimates of the trend in GMSL show good agreement, the variability in each of the GMSL time series is substantially different. This

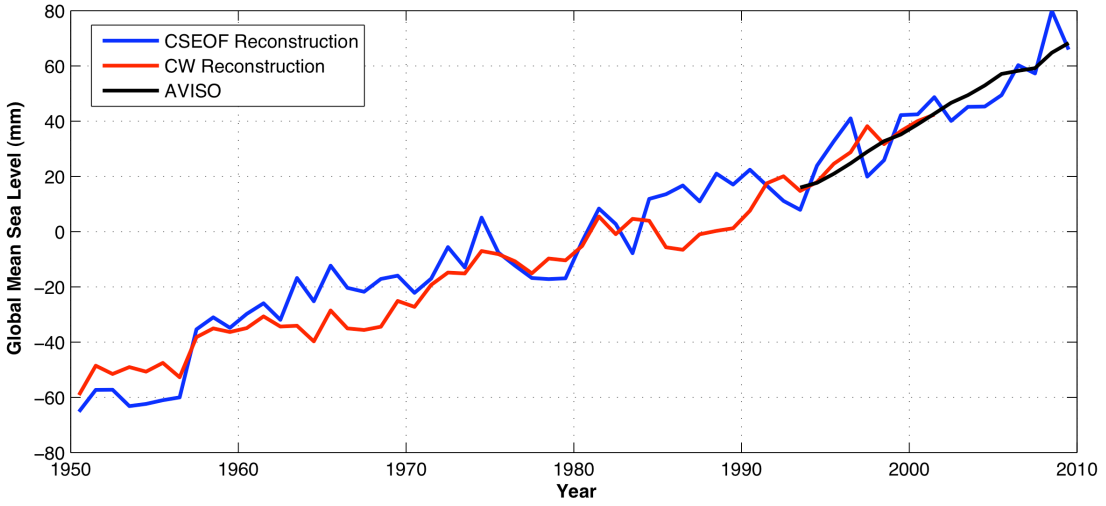

Figure 9.12**.** A comparison of GMSL derived from satellite altimetry (1993-present; black) from the CSEOF reconstruction using latitudinal-band weighting (blue) and from the CW EOF reconstruction (red).

could be a result of differences in the tide gauge data, but more likely represents the differences that occur from the reconstruction correction that is made in the case of our CSEOF reconstruction GMSL estimate.

The corrected trend in GMSL from the CSEOF reconstruction technique is estimated to be 3.11 mm/yr. from 1993 to 2009. The subsampled reconstruction accounts for an additional 0.04 mm/yr. of GMSL at the tide gauge locations. For comparison, the GMSL estimated from the AVISO satellite altimetry data is 3.28 mm/yr., again showing good agreement with the reconstructed GMSL.

While it is difficult to obtain a formal estimate of the error on the GMSL trend, we can use a randomization procedure to determine the sensitivity of the trend to the tide gauge selection. The sensitivity was estimated using a Monte Carlo procedure in which only 70% of the total available tide gauges were used for the reconstruction. The entire reconstruction procedure was carried out (including the correction of GMSL) one hundred times, and the statistics were computed from

the results. The reconstruction itself was relatively insensitive to the tide gauge selection. The ENSO mode correlation with the MEI was found to be 0.90 ± 0.04 across the 100 trials. On the other hand, the GMSL estimates were much more sensitive to selection of tide gauges. Over the period 1950 to 2009, the estimate of the trend in GMSL was 1.84 ± 0.4 mm/yr. across the 100 trials. Furthermore, the estimate of the trend in GMSL from 1993 to 2009 was 3.42 ± 0.6 mm/yr. These standard deviations are much larger than those found in CW using similar randomization tests. This increased sensitivity likely results from the use of latitude-band weighting. If a given ten-degree latitude band contains only two tide gauges at a certain time, removing one of these will have a significant effect on the estimate of GMSL since each latitude band is weighted equally. This effect is more pronounced at the ends of the time series, where the total number of tide gauges available is smaller. While this may be one advantage of using other weighting schemes to compute GMSL, the robustness of the CSEOF reconstruction with latitude-band weighting to tide gauge selection is encouraging, and regard the arguments of M09 as further support of the selection of this weighting scheme.

9.5. Discussion

The work of Ch02 and CW has helped transition the reconstruction techniques of SST into techniques for reconstructing SSH. There is clearly room, however, for improvement. EOFs are simple to compute from satellite altimetry, but are not entirely suitable as basis functions for a reconstruction. EOFs enforce stationarity of the spatial pattern on the resulting reconstruction. We can lessen the impact of stationarity assumptions by using CSEOFs while also capturing the cyclostationary signals in the ocean. The CSEOF loading vectors are periodic with a certain nested period, defined to be one year when attempting to extract the annual cycle signal. Perhaps

the greatest advantage in using CSEOFs over EOFs is the ability to capture the evolution of cyclostationary geophysical signals in a single mode.

Past reconstructions have removed the annual cycle signal from both the satellite altimetry and tide gauge data prior to performing the analysis, in part due to the spreading of annual cycle signal across several EOF modes. CSEOF decomposition, on the other hand, separates the annual cycle (Fig. 8.1), capturing the one-year periodicity as well as its lower-frequency amplitude modulation. The second mode obtained from a CSEOF decomposition of the satellite altimetry data represents the ENSO variability in the dataset (Fig. 8.3) with no apparent leakage from the annual cycle signal. Initial CSEOF reconstructions demonstrate an improvement in the correlation of ENSO-reconstructed amplitude and common climate indices from 0.78 to 0.91 when compared to the results reported by CW. Reconstructing individual modes that are dynamically important benefits the evaluation of GMSL and climate indices.

In addition to the choice of basis functions, the weighting used in the reconstruction procedure and the selection of tide gauges has considerable effect on the reconstruction. The choices made by CW provide for a reconstructed dataset, but questions remain whether it is the most accurate reconstruction possible. Table 9.2 demonstrates the consequences of different tide gauge editing on resulting trends over both long and short time periods. Experts with extensive knowledge of the quality of individual tide gauge sites heavily edited tide gauge datasets #3 and #4. This results in a dataset with relatively few tide gauges. The question remains as to whether such a set is superior to one with much looser editing criteria (#2) or no editing criteria at all (#1). The reasonable trend and very high correlations in Table 9.2 suggest that simply using the PSMSL dataset (with IB and GIA corrections) in its complete form may be superior to manual editing and would certainly be free of any biases introduced as part of the editing process.

The weighting used in the reconstruction procedure also influences the GMSL estimates computed from a given set of tide gauges. M09 provides justification and support for adopting a latitude-band weighting scheme, and the CSEOF reconstruction computed using such a scheme exhibits good agreement with other sea level datasets. However, the large differences between a simple mean calculation and a latitude-band weighting calculation underscores the need for further investigation on this issue.

The procedure of reconstructing sea level does not lend itself well to estimating GMSL. There is no basis function calculated from the short altimetric record – either EOF or CSEOF – that captures and explains mean sea level from 1950 to 2009. One way to address this issue is to introduce an artificial basis function, as done in CW, that essentially computes a weighted average of the tide gauges at each point in time. It is important to understand that although they have included this computation as part of their reconstruction, it is really an independent computation and should be viewed separately from the reconstruction of signals like ENSO. The computation of GMSL is only as good as the tide gauges used and the reconstruction procedure itself does not provide any significant benefit.

It is possible, however, to use the reconstruction to improve on estimates of the trend in GMSL. Rather than introduce a new, artificial basis function, the computation of GMSL can be decoupled from the fitting of the basis functions to the tide gauges. For the analysis shown above, this provides reasonable values for the trend in GMSL. However, these estimates are still sensitive to the tide gauge selection. In short, incorporating GMSL into sea level reconstructions is not a trivial task and demands further consideration. The GMSL time series of CW has been used for a wide-range of applications, but caution must be taken in using these results. It is not hard to edit the tide gauges in such a way that a vastly different trend is obtained.

Despite the difficulties with incorporating GMSL into the reconstruction procedure, the CSEOF reconstruction technique has shown great promise to accurately capture signals in the ocean, regardless of the tide gauge editing. The correlations between the reconstruction and climate indices like the MEI and EMI are high for all seven of the tide gauge datasets considered here. Applications involving regional trends or periodic climate signals should be the focus of sea level reconstruction work, as it is in these areas that the CSEOF reconstruction can prove the most beneficial.

9.6 Future Work

The CSEOF reconstruction technique is still in its infancy and applications of the reconstructed dataset have not been fully explored. Several questions remain unanswered, including the best technique for selecting tide gauges, the correct weighting to use in the reconstruction procedure, and how best to account for the unknown datum shift between tide gauges. In addition to answering these questions, the results presented here extend back only to 1950, while the tide gauge record provides measurements back into the early 19th century. Once the reconstruction has been extended, assessing the accuracy of the dataset becomes difficult due to the lack of data available for comparison before 1950.

In addition to practical issues involving the actual computation of the reconstruction, applications of the resulting dataset will need to be investigated. Perhaps the easiest way to find applications would be by forming collaborations across a broad range of disciplines. A reconstructed sea level dataset such as the one described here is potentially a valuable resource for oceanographers, glaciologists, hydrologists, and climate modelers. An initial CSEOF reconstructed dataset will be submitted to NASA/JPL PO.DAAC for general release to the Earth

system science community. The quality of the dataset can then be verified by stringent review as users access the preview dataset and evaluate the reconstruction for a wide-range of applications. Eventually software will be developed allowing users to compute their own CSEOF sea level reconstructions. This software will include the ability to edit tide gauges so that the user can understand the effect tide gauge selection has on the resulting reconstruction.

9.7 Summary and Conclusion

Accurate observations of sea level change are critical to understand how changes in climate affect the earth's water reservoirs. However, those same observations will also determine the socio-economic impact of sea level change. Although the public is justifiably concerned about the future of sea level rise, estimating future sea change will be difficult absent an understanding how the current state of the oceans compares to past states. The more challenging work of reconstructing sea level is still in its infancy, despite well-established reconstructions and studies for SST data. Reconstruction techniques take advantage of both the accurate measurements of modern instruments and the long duration of historical records to investigate how sea level and climate has changed over the past century. Using a fully reconstructed sea level dataset, we can study the change in ocean signals (such as those related to the annual cycle and ENSO) over a longer period that cannot be resolved with satellite altimetry records and shorter duration reconstructions. While the annual and ENSO signals are of interest, investigating climate signals at decadal and multi-decadal timescales is even more important because of their potentially significant impact on sea level change. Before such studies can be started, questions must be answered regarding the accuracy of sea level reconstructions and an understanding must be gained of how the user-defined parameters (tide gauge editing, weighting,

basis function, etc.) affect the reconstructed dataset. In short, however, the CSEOF reconstruction technique presented here provides the first significant effort toward improving upon earlier published sea level reconstructions and will hopefully lead to a better understanding of how to compute sea level reconstructions in the future.

CHAPTER 10: SUMMARY AND CONCLUSION

Mitigating the effects of rising sea level is of the utmost importance given the number of people throughout the world living near coastlines or on islands. Our ability to plan and account for such threats is limited by our ability to detect hazards and understand how these hazards develop and evolve. The work presented here focuses on improving the ability to detect changes in sea level from two specific sea level hazards. The feasibility of tsunami detection in the open ocean has been demonstrated using measurements from satellite altimeters. While satellite altimeters are not optimal for tsunami detection in terms of temporal and spatial sampling, these techniques can hopefully be extended to other space and airborne sensors that make measurements of variations of ocean surface roughness across much wider swaths. The broader surface coverage of these sensors suggests that they are far more promising for early tsunami detection in the open ocean and may be an important component in a future global system for tsunami detection and warning.

The other sea level hazard discussed in this thesis also poses a significant threat to coastal communities, albeit on a much longer timescale. Rising sea level as a result of climate change has been well documented and widely discussed in recent years. Often the trend in global mean sea level is cited to highlight the dangers of rising sea level, but perhaps more relevant to nations around the world are the regional trends in sea level. The seventeen-year satellite altimetry is long enough to estimate the trend in GMSL with a high degree of certainty. This is not true, however, of regional sea level trends where ocean variability can serve to mask the underlying trend. Tools like CSEOFs can improve our ability to estimate regional sea level trends, but more work and time is needed until regional sea level trends are estimable with the same degree of

confidence as GMSL. In addition to understanding the current state of the ocean, an important part of predicting the state of the ocean in the future is understanding how sea level has changed in the past. Sea level reconstruction techniques have been developed in the last decade that seek to marry the satellite altimetry data with the tide gauge data obtained over the last two centuries. These techniques, however, are still in their infancy, and while the work presented here is an advancement of the methods used in the past, there is still significant improvement that needs to be made. In short, this thesis represents an incremental step for both the tsunami detection and sea level rise problems, but more work is needed to make such techniques practical and capable of providing the information that is needed to make critical decisions regarding the safety of coastal communities around the world.

CHAPTER 11: REFERENCES

Ablain, M., J. Dorandeu, P.-Y. Le Traon, and A. Sladen, 2006: High resolution altimetry reveals new characteristics of the December 2004 Indian Ocean tsunami, Geophys. Res. Lett., 33, L21602, doi:10.1029/2006GL027533, 2006.

Acton, F.S., 1966: *Analysis of straight-line data*. Dover Publications, New York, 267 pp.

Artru, J., P. Lognonné, G. Occhipinti, F. Crespon, R. Garcia, E. Jeansou, M. Murakami, 2005: Tsunami detection in the ionosphere, *Space Res. Today*, 163, 23-27.

Ashok, K., S.K. Behera, S.A. Rao, H. Wang, T. Yamagata, 2007: El Nino Modoki and its possible teleconnection, *J. Geophys. Res.*, **112**, C11007.

Behrens, J., A. Androsov, S. Harig, F. Klaschka, L. Mentrup, W.S. Pranowo, H.Y. Cui, J. Schroter, and W. Hiller, 2008: Design and performance testing of a multi-sensor quick assimilation technique for tsunami early warning in the GITEWS simulation system, Geophys. Res. Abstr., 10, EGU2008-A-01878, 2008.

Beckley, B.D., F.G. Lemoine, S.B. Lutchke, R.D. Ray, N.P. Zelensky, 2007: A reassessment of global and regional mean sea level trends from TOPEX and Jason-1 altimetry based on revised reference frame and orbits. *Geophys. Res. Lett.* **34**, L14607.

Bernard, E. N., H.O. Mofjeld, V.V. Titov, C.E. Synolakis, and F.I. Gonzalez, 2006: Tsunami: scientific frontiers, mitigation, forecasting and policy implications, Phil. T. R. Soc. A, 364, 1989–2007, doi:10.1098/rsta.2006.1809.

Cazenave, A. and R.S. Nerem, 2004: Present day sea level change: Observations and causes.

Rev. Geophys., **42**, RG3001.

Cane, M.A., A.C. Clement, A. Kaplan, S.E. Zebiak, and D. Huang, 2004: Predictability of El Nino over the past 148 years. *Nature*, **428**, 733-736.

Chambers, D.P., C.A. Melhaff, T.J. Urban, D. Fuji, R.S. Nerem, 2002: Low-frequency variations in global mean sea level: 1950-2000, *J. Geophys. Res.,* **107**, 3026.

Chiang, J.C.H. and D.J. Vimont, 2004: Analogous Pacific and Atlantic meridional modes of tropical atmosphere-ocean variability. *J. Climate*, **17**, 4143-4158.

Church, J.A., N.J. White, R. Coleman, K. Lambeck, J.X. Mitrovica, 2004: Estimates of the regional distribution of sea level rise over the 1950-2000 period. *J. Climate*, **17**, 2609-2625.

Church, J.A., N.J. White, 2006: A 20th century acceleration in global sea level rise, *Geophys. Res. Lett.*, **36**, L040608.

Compo, G.P. and P.D. Sardeshmukh, 2010: Removing ENSO-Related variations from the climate record. *J. Climate*, **23**, 1957-1978.

Dudley, W. C. and M. Lee, 1998: Tsunami!, University of Hawaii Press, Honolulu, 5 pp., 302–303, 321–322.

Douglas, B.C., 1991: Global Sea Level Rise. *J. Geophys. Res.* **96(C4)**, 6981-6992.

Edgington, E. S., 1995: Randomization Tests, Marcel Dekker, New York.

Fine, I. V., A.B. Rabinovich, and R.E. Thomson, 2005: The dual source region for the 2004 Sumatra tsunami, *Geophys. Res. Lett.*, 32, L16602, doi:10.1029/2005GL023521.

Folland, C.K., D.E. Parker, A.W. Coleman, and R. Washington, 1999: Large scale modes of ocean surface temperature since the late nineteenth century. *Beyond El Nino: Decadal and Interdecadal Climate Variability*, A. Navarra, Ed. Springer-Verlag, 73-102.

Freilich, M. H. and P.G. Challenor, 1995: A new approach for determining fully empirical altimeter wind speed model functions, *J. Geophys. Res.*, 99, 25051–25062.

Fujii, Y. and K. Satake, 2007: Tsunami source of the 2004 Sumatra-Andaman earthquake inferred from tide gauge and satellite data, *B. Seismol. Soc. Am*., 97, 192–207, doi:10.1785/0120050613.

Garratt, J. R., 1994: The Atmospheric Boundary Layer, Cambridge University Press, Cambridge.

Fu, L.-L. and A. Cazenave, 2001: Satellite Altimetry and Earth Sciences: A Handbook of Techniques and Application, Int. Geophys. Ser., vol. 69, 463 pp, Elsevier, New York, USA.

Geist, E. L., V.V. Titov, D. Arcas, F.F. Pollitz, and S.L. Bilek, 2007: Implications of the 26 December 2004 Sumatra-Andaman earthquake on tsunami forecast and assessment models for great subduction-zone earthquakes, *B. Seismol. Soc. Am.,* 97, 249–270, doi:10.1785/0120050619.

Giese, B.S., G.P. Compo, N.C. Slowey, P.D. Sardeshmukh, J.A. Carton, S. Ray, J.S. Whitaker, 2009: The 1918/1919 El Niño, *Bull. Amer. Met. Soc.*, **91**, 177-183.

Godin, O. A., 2003: Influence of long gravity waves on wind velocity in the near-water layer and feasibility of early tsunami detection, Dokl. Earth Sci., 391, 841–844.

Godin, O. A., 2004: Air-sea interaction and feasibility of tsunami detection in the open ocean, J. Geophys. Res., 109, C05002, doi:10.1029/2003JC002030.

Godin, O. A., 2005: Wind over fast waves and feasibility of early tsunami detection from space, in: Frontiers of Nonlinear Physics, edited by: Litvak, A., Inst. Appl. Phys., Nizhny Novgorod, 210–215.

Godin, O. A. and V.G. Irisov, 2003: A perturbation model of radiometric manifestations of oceanic currents, *Radio Sci.*, 38, 8070, doi:10.1029/2002RS002642.

Godin, O.A, V.G. Irisov, R.R. Leben, B.D. Hamlington, G.A. Wick, 2009: Variations in sea surface roughness induced by the 2004 Sumatra-Andaman Tsunami, Nat. Hazards Earth Syst. Sci., 9, 1135-1147.

Gonzalez, F. I., E.N. Bernard, C. Meinig, M.C. Eble, H.O. Mofjeld, and S. Stalin, 2005: The NTHMP tsunameter network, Nat. Hazards, 35, 25–39, doi: 10.1007/s11069-004-2402-4.

Goswami, B., 1995: A multi-scale interaction model for the origin of the tropospheric QBO. *J. Climate*, **8**, 524-534.

Gower, J. 2007: The 26 December 2004 tsunami measured by satellite altimetry, Int. J. Remote Sens., 28, 2897–2913, doi:10.1080/01431160601094484.

Groger, M. and H.P. Plag, 1993: Estimations of a global sea level trend: limitations from the structure of the PSMSL global sea level data set. *Global Planet. Change*, **8,** 161.

Gu, D., S.G.H. Philander, M.J. McPhaden, 1997: The seasonal cycle and its modulation in the eastern tropical Pacific Ocean. *J. Phys. Oceanogr.*, **27**, 2209-2218.

Hamlington, B.D., O.A. Godin, V.G. Irisov, R.R. Leben, 2011: Detection of tsunamis from changes in sea surface roughness, Tsunami, Research and Technologies, Intech, Rjeka, Croatia.

Hamlington, B.D., R.R. Leben, R.S. Nerem, K.-Y. Kim, 2011: The effect of signal-to-noise ratio on the study of sea level trends, *J. Climate*, in press.

Han, W., G.A. Meehl, B. Rajagopalan, J. Fasullo, A. Hu, J. Lin, W. Large, J. Wang, X. Quan, L. Trenary, A. Wallcraft, T. Shinoda, S. Yeager, 2010: Patterns of Indian Ocean sea level change in a warming climate, *Nat. Geosci.*, DOI:10.1038/NGEO901.

Hara, T. and W.J. Plant, 1994: Hydrodynamic modulation of short wind-wave spectra by long waves and its measurement using microwave backscatter, *J. Geophys. Res*., 99, 9767–9784.

Hayashi, Y., 2008: Extracting the 2004 Indian Ocean tsunami signals from sea surface height data observed by satellite altimetry, *J. Geophys. Res*., 113, C01001, doi:10.1029/2007JC004177.

Hirata, K., K. Satake, Y. Tanioka, T. Kuragano, Y. Hasegawa, Y. Hayashi, and N. Hamada, 2006: The 2004 Indian Ocean tsunami: Tsunami source model from satellite altimetry, *Earth Planets Space*, 58, 195–201.

Hoechner, A., A.Y. Babeyko, and S.V. Sobolev, 2008: Enhanced GPS inversion technique applied to the 2004 Sumatra earthquake and tsunami, *Geophys. Res. Lett*., 35, L08310, doi:10.1029/2007GL033133.

Holgate, S.J., and P.L.Woodworth, 2004: Evidence for enhanced coastal sea level rise during the 1990s, *Geophys. Res. Lett.*, 31, L07305.

Holgate, S.J., 2007: On the decadal rates of sea level change during the twentieth century, *Geophys. Res. Lett.*, 34, L01602.

Houghton, J.T., L.G. Meira Filho, B.A. Callander, N. Harris, A. Kattenberg, K. Maskell., 1996: *Climate Change 1995*. Cambridge University Press, Cambridge, 572 pp.

Houghton, J.T., Y. Ding, D.J. Griggs, M. Noguer, P.J. van der Linden, X. Dai, K. Maskell, and C.A. Johnson, Eds., 2001: *Climate Change 2001: The Scientific Basis.* Cambridge Univeristy Press, 881 pp.

Kanamori, H. and M. Kikuchi, 1993: The 1992 Nicaragua Earthquake: a slow tsunami earthquake associated with subducted sediments, *Nature*, 361, 714-716.

Kaplan, A.M., M.A. Cane, Y. Kushnir, A.C. Clement, M.B. Blumenthal, and B. Rajagopalan, 1998: Analyses of global sea surface temperature 1856-1991. *J. Geophys. Res.,* **103**, 18567-17589.

Kaplan, A.M., Y. Kushnir, M.A. Cane, 2000: Reduced Space Optimal Interpolation of Historical Marine Sea Level Pressure 1854-1992, *J. Climate*, **13**, 2987-3002.

Kelly, P.M. and P.D. Jones, 1996: Removal of the El Nino-Southern Oscillation signal from the gridded surface air temperature data set. *J. Geophys. Res.,* **101**, 19013-19022.

Kim, K.-Y., G.R. North and J. Huang, 1996: EOFs of one-dimensional cyclostationary time series: Computations, examples, and stochastic modeling. *J. Atmos. Sci.,* **53**, 1007-1017.

Kim, K.-Y. and G.R. North, 1997: EOFs of harmonizable cyclostationary processes. *J. Atmos. Sci.,* **54**, 2416-2427.

Kim, K.-Y. and Q. Wu, 1999: A comparison of study of EOF techniques: Analysis of nonstationary data with periodic statistics. *J. Climate*, **12**, 185-199.

Kim, K.-Y. and C. Chung, 2001: On the evolution of the annual cycle in the tropical Pacific. *J. Climate*, **14**, 991-994.

Kudryavtsev, V. N., C. Mastenbroek, and V.K. Makin, 1997: Modulation of wind ripples by long surface waves via the air flow: a feedback mechanism, *Bound.-Lay. Meteorol*., 83, 99–116.

Kulikov, E. A., P.P. Medvedev, and S.S. Lappo, 2005: Satellite recording of the Indian Ocean tsunami on December 26, 2004, *Dokl. Earth Sci*., 401A, 444–448.

Kumar, B. P., R.R. Kumar, S.K. Dube, T. Murty, A. Gangopadhyay, A. Chaudhuri, and A.D. Rao, 2006: Tsunami travel time computation and skill assessment for the 26 December 2004 event in the Indian Ocean, *Coast. Eng. J.*, 48, 147–166.

Lau, K.-M. and H. Weng, 1999: Interannual, decadal-interdecadal, and global warming signals in sea surface temperature during 1955-97. *J. Climate*, **12**, 1257-1267.

Lautenbacher, C. C. (2005). Tsunami warning systems, *The Bridge*, 35, 21–25.

Lay, T., H. Kanamori, C.J. Ammon, M. Nettles, S.N. Ward, R.C. Aster, S.L. Beck, S.L. Bilek, M.R. Brudzinski, R. Butler, H.R. DeShon, G. Ekstrom, K. Satake, and S. Sipkin, 2005: The Great Sumatra-Andaman Earthquake of 26 December 2004, Science, 308, 1127–1133, doi:10.1126/science.1112250.

Le Traon, P.-Y., F. Nadal, N. Ducet, 1998: An improved mapping method of multi-satellite altimeter data, J. Atmos. Oceanic Technol., 15, 522-534.

Leuliette, E.W., R.S. Nerem, G.T. Mitchum, 2004: Results of TOPEX/Poseidon and Jason calibration to Construct a Continuous Record of Mean Sea Level. *Mar. Geodesy*, **27**, 79-94.

Levin, B. W. and M.A. Nosov, 2005: Physics of Tsunamis and Kindred Phenomena, Janus-K, Moscow.

Meehl, G.A., J.M. Arblaster, K. Matthes, F. Sassi, and H. van Loon, 2009: Amplifying the Pacific Climate System Response to a Small 11-Year Solar Cycle Forcing, *Science*, 325, 1114.

Merrifield, M.A., S.T. Merrifield, G.T. Mitchum, 2010: Evidence for anomalous recent acceleration of global sea level rise, *J. Climate*, **22**, 5772-5781.

Miller, L. and B.C. Douglas, 2007: Gyre-scale atmospheric pressure variations and their relation to 19th and 20th century sea level rise. *Geophys. Res. Lett.*, **34**, L16602.

Mitrovica, J.X., J.L. Davis, 1995: Present-Day Post-Glacial Sea Level Change Far From the Late Pleistocene Ice Sheets: Implications for Recent Analyses of Tide Gauge Records, *Geophys. Res. Lett.*, **22**, 2529-2532.

Montgomery, D.C., E.A. Peck, 1982: *Introduction to Linear Regression Analysis*, John Wiley and Sons, Inc., New York, 495 pp.

Naeije, M., E. Schrama, and R. Scharroo, 2000: The Radar Altimeter Database System project RADS. Proc. of the IEEE 2000 Int. Geoscience and Remote Sensing Symp. (IGARSS 2000), Honolulu, HI, IEEE, 487-490.

Nagai, T., T. Kato, N. Moritani, H. Izumi, Y. Terada, and M. Mitsui, 2007: Proposal of hybrid tsunami monitoring network system consisted of offshore, coastal and on-site wave sensors, *Coast. Eng. J.*, 49, 63–76.

Nerem, R.S., 1995: Global mean sea level variations from TOPEX/POSEIDON altimeter data. *Science,* **268**, 708-710.

Nerem, R.S., 1999: Measuring very low frequency sea level variations using satellite altimeter data. *Glob. and Planetary Change*, **20**, 157-171.

Nerem, R.S., D.P. Chambers, E.W. Leuliette, G.T. Mitchum, B.S. Giese, 1999: Variations in global mean sea level associated with the 1997–98 ENSO event. *Geophys. Res. Lett.* **26:19**, 3005-3008.

Nerem, R.S., D.P. Chambers, B.D. Hamlington, R.R. Leben, G.T. Mitchum, T. Phillips, J.K. Willis, 2010: Observations of recent sea level change, IPCC Workshop on Sea Level Rise & Ice Sheet Instabilities, Malaysia, June, 2010.

North, G.R., 1984: Empirical orthogonal functions and normal modes. *J. Atmos. Sci.,* **41**, 7563-7571.

Occhipinti, G., P. Lognonné, A. Kherani, H. Hebert, 2006: 3D Waveform modeling of ionospheric signature induced by the 2004 Sumatra tsunami, *Geophys. Res. Lett.*, doi:10.1029/2006GL026865.

Okal, E.A., A. Piatanesi, and P. Heinrich, 1999: Tsunami detection by satellite altimetry, J. Geophys. Res., 104, 599–615.

OOPC, 2010: http://ioc-goos-oopc.org/state_of_the_ocean/sur/, Ocean Observations Panel for Climate, State of Ocean Surface Indices Webpage.

Parker, D., C. Folland, A. Scaife, J. Knight, A. Colman, P. Baines, and B. Dong, 2007: Decadal to multidecadal variability and the climate change background. *J. Geophys. Res.,* **112,** D18115.

Pascual, A., Y. Faugère, G. Larnicol, P.Y. Le Traon, 2006: Improved description of the ocean mesoscale variability by combining four satellite altimeters. Geophys. Res. Lett., 33, 2.

Peltier, W.R., A.M. Tushingham, 1989: Global sea level rise and the greenhouse effect: might they be connected? *Science*, **244**, 806-810.

Penland, C. and L. Matrusova, 2006: Studies of El Nino and interdecadal variability in topical sea surface temperature using a nonnormal filter. *J. Climate*, **11**, 5796-5815.

Pezzulli, S., D.B. Stephenson, A. Hannachi, 2005: The variability of seasonality. *J. Climate*, **18**, 71-88.

Philander, S.G., 1990: *El Nino, La Nina, and the Southern Oscillation*. Academic Press, 293 pp.

Powell, B. S. and R.R. Leben, 2004: An optimal filter for geostrophic mesoscale currents from along-track satellite altimetry, *J. Atmos. Ocean. Tech.,* 21, 1633–1642.

Rasmusson, E.M. and J.M. Wallace, 1993: Meteorological aspects of El Nino/Southern Oscillation. *Science*, **220**, 1195-1202.

Rasmusson, E.M., X. Wang, C.F. Ropelewski, 1990: The biennial component of ENSO variability. *J. Mar. Syst.*, **1**, 71-96.

Ray, R.D and B.C. Douglas , 2011: Experiments in Reconstructing Twentieth-Century Sea Levels, *in prep.*

Robock, A., and J. Mao, 1995: The volcanic signal in surface temperature observations. *J. Climate*, **8**, 1086-1103.

Rowan, L., 2004: Tsunami and its shadow, *Science*, 304, p.1569.

Schindele, F., A. Loevenbruck, and H. Hebert, 2008: Strategy to design the sea-level monitoring networks for small tsunamigenic oceanic basins: the Western Mediterranean case, Nat.

Hazards Earth Syst. Sci., 8, 1019–1027, http://www.nat-hazards-earth-syst-sci.net/8/1019/2008/, 2008.

Sladen, A. and H. Hebert, 2008: On the use of satellite altimetry to infer the earthquake rupture characteristics: application to the 2004 Sumatra event, *Geophys. J. Int*., 172, 707–714, doi:10.1111/j.1365-246X.2007.03669.x.

Smith, T.M., R.W. Reynolds, R.E. Livezey, D.C. Stokes, 1996: Reconstruction of historical sea surface temperatures using empirical orthogonal functions, *J. Climate*, **9**, 1403-1420.

Smith, T.M., R.W. Reynolds, T.C. Peterson, and J. Lawrimore, 2008: Improvements to NOAA's Historical Merger Land-Ocean Surface Temperature Analysis (1880-2006), *Journal of Climate*, **21**, 2283-2296.

Smith, W. H. F., R. Scharroo, V.V. Titov, D. Arcas, and B.K. Arbic, 2005: Satellite altimeters measure tsunami, Oceanography, 18, 11–13.

Song, T. Y., C. Ji, L.L. Fu, V. Zlotnicki, C.K. Shum, Y. Yi, and V. Hjorleifsdottir, 2005: The 26 December 2004 tsunami source estimated from satellite radar altimetry and seismic waves, *Geophys. Res. Lett*., 32, L20601, doi:10.1029/2005GL023683.

Stein, S. and E.A. Okal, 2005: Speed and size of the Sumatra earthquake, Nature, 434, 581–582, doi:10.1038/434581a.

Sturges, W., 1990: Large-scale coherence of sea level at very low frequencies, *Sea Level Change*, Report of N.A.S Geophysics Study Committee on Sea Level Change, 63-72.

Sturges, W. and B.G. Hong, 2001: Decadal variability of sea level, *Sea Level Rise*, Douglas, Kearney, and Leatherman, eds., Academic Press, 165-180.

Synolakis, C. E. and E.N. Bernard, 2006: Tsunami science before and beyond Boxing Day 2004, Philos. T. Roy. Soc. A., 364, 2231– 2265, doi:10.1098/rsta.2006.1824.

Synolakis, C. E., E.N. Bernard, V.V. Titov, U. Konoglu, F.I. Gonzalez, 2008: Validation and verification of tsunami numerical models, Pure Appl. Geophys., 165(11-12), 2197-2228.

Titov, V., A.B. Rabinovich, H.O. Mofjeld, R.E. Thomson, and F.I. Gonzalez, 2005: The global reach of the 26 December 2004 Sumatra tsunami, Science, 309, 2045–2048, doi:10.1126/science/1114576.

Titov, V.V., and C.E. Synolakis, 1997: Extreme inundation flows during the Hokkaido-Nansei-Oki tsunami, Geopshysics Res. Lett., 24(11), 1315-1318.

Trenberth, K.E., 2004: Interannual Variability of Patterns of Atmospheric Mass Distribution, *J. Climate*, **18**, 2812-2825.

Troitskaya, Y. I. and S.A. Ermakov, 2005: Recording of the December 26, 2004 tsunami in the open ocean based on variations in radar scattering section, Dokl. Earth Sci., 405A, 1384–1387.

Troitskaya, Y. I. and S.A. Ermakov, 2008: Manifestations of the Indian Ocean tsunami of 2004 in satellite nadir-viewing radar backscattering variations, Int. J. Remote Sens., 29, 6361–6371, doi:10.1080/01431160802175348.

Vermeer, M., S. Rahmstorf, 2009: Global sea level linked to global temperature, *Proc. Of Nat. Acad. Of Sci. USA,* **106**, 21527-21532.

Vimont, D.J., 2005: The contribution of the interannual ENSO cycle to the spatial pattern of decadal ENSO-like variability, *J. Climate*, **18**, 2080-2092.

Vyushin, D., and P.J. Kushner, 2009: Power-law and long-memory characteristics of the atmospheric general circulations. *J. Climate*, **22**, 2890-2904.

Walker, D. A., 1996: Observations of tsunami "shadows": A new technique for assessing tsunami wave heights?, Science of Tsunami Hazards, 14, 3–11.

Wei, Y., E.N. Bernard, L. Tang, R. Weiss, V.V. Titov, C. Moore, M. Spillane, M. Hopkins, and U. Kanoglu, 2008: Realtime experimental forecast of the Peruvian tsunami of August 2007 for US coastlines, Geophys. Res. Lett., 35, L04609, doi:10.1029/2007GL032250.

Witter, D. L. and D.B. Chelton, 1991: A geosat altimeter wind speed algorithm and a method for altimeter wind speed algorithm development, *J. Geophys. Res*., 96, 8853–8860.

Wolter, K., and M. S. Timlin, 1998: Measuring the strength of ENSO events - how does 1997/98 rank? *Weather,* **53,** 315-324.

Wolter, K., 2010: http://www.esrl.noaa.gov/psd/people/klaus.wolter/MEI/, NOAA Earth System Research Laboratory, Mulitvariate ENSO Index webpage.

Wu, Z., N.E. Huang, S.R. Long, and C.-K. Peng, 2007: On the trend, detrending and variability of nonlinear and non-stationary time series. *Proc. Nat. Acad. Sci. USA,* **104**, 14889-14894.

Wu, Z., E.K. Schneider, B.P. Kirtman, E.S. Sarachik, N.E. Huang, C.J Tucker, 2008: The modulated annual cycle: an alternative reference frame for climate anomalies, *Clim. Dyn.,* **31**, 823-841.

Zaichenko, M. Y., E.A. Kulikov., B.V. Levin, and P.P. Medvedev, 2005: On the possibility of registration of tsunami waves in the open ocean with the use of a satellite altimeter, Oceanology, 45, 194–201.

Zhang, Y., J.M. Wallace, and D.S. Battisti, 1997: ENSO-like interdecadal variability: 1990-93. *J. Climate*, **10**, 1004-1020.